University of Nevada, Reno

Investigating Atmospheric River Precipitation and Associated Snowpack Characteristics Under a Future Warmer Climate Scenario: Case Studies from the Eastern Sierra Nevada near Donner Summit, California

A thesis submitted in partial fulfillment of the requirements for the degree of Master of Science in Atmospheric Science

by

Paul G. Fremeau

Dr. Douglas P. Boyle/Thesis Advisor

May, 2021

THE GRADUATE SCHOOL

We recommend that the thesis
prepared under our supervision by

PAUL G. FREMEAU

entitled

Investigating Atmospheric River Precipitation and Associated Snowpack Characteristics Under a Future Warmer Climate Scenario: Case Studies from the Eastern Sierra Nevada near Donner Summit, California

be accepted in partial fulfillment of the
requirements for the degree of

MASTER OF SCIENCE

Douglas P. Boyle, Ph.D.
Advisor

Neil P. Lareau, Ph.D.
Committee Member

John F. Mejia, Ph.D.
Committee Member

Kristin A. Lewis, Ph.D.
Graduate School Representative

David W. Zeh, Ph.D., Dean
Graduate School

May, 2021

Abstract

Atmospheric rivers (ARs) making landfall along the California coast have been warming since the 1980's, resulting in changing AR precipitation and temperature characteristics in the Sierra Nevada of California, increasing flood risk, hydrologic resource stress, and impacting winter recreation and local economies. This warming trend is projected to continue, significantly altering the altitude of freezing levels within ARs and changing AR precipitation characteristics for the study area. The pseudo-global warming method (PGW) was utilized to study how five recent ARs could manifest meteorologically at the surface under IPCC RCP8.5 near the end of the 21st century. Projected changes include increasing variability in AR precipitation, warmer near-surface temperatures, and an increase in freezing levels by the end of the 21st century. These changing AR characteristics raise concerns of both flooding and snow drought which would negatively affect environmental health and safety, induce hydrological stress, and damage local economies.

Acknowledgements

A debt of gratitude is owed to Itinderjot Singh, Ph.D. candidate at the University of Illinois Urbana-Champaign, for offering his time and guidance on the subject of calculating temperature deltas from RCP8.5 GCM future climate simulations and applying those deltas to a reanalysis dataset. IT generously donated hours of his time in support of this complex modeling experiment.

I would also like to express my gratitude to WeatherExtreme Ltd. and Dr. Elizabeth Austin, CEO, for generously providing computing resources, an inspiring workspace, and encouragement in support of the research undertaken for this thesis.

Mikhail Korotkin, also of WeatherExtreme Ltd. and a master's student in the Department of Atmospheric Science at the University of Nevada, Reno served as a tremendous resource in support of the technical challenges of WRF modeling and the creation of high-quality graphics. Mikhail's knowledge of high-performance computing and architecture, as well as mastery in the use of Python with respect to atmospheric analysis and graphics was invaluable to this research.

Table of Contents

List of Tables

List of Figures

Background

Atmospheric Rivers (ARs) are long, narrow regions of enhanced moisture transport which, upon making landfall, produce precipitation, at times intense, that can be both beneficial and destructive to affected communities. At the global scale, ARs are significant because they account for 90% of global poleward moisture transport despite covering only 10% of the longitudinal length at a given latitude (Zhu & Newell, 2020). At a regional scale, ARs provide an average of 30% to 50% of the total annual precipitation in the western United States (Dettinger 2011). ARs also contribute 30% to 40% of the annual snowpack to the Sierra Nevada mountains (Guan et al., 2010). In turn, the Sierra Nevada snowpack provides drinking water for the majority of Californians. We expect shifts in the frequency, strength, and average landfall location of ARs under our changing climate. The effects of climate change on atmospheric rivers warrant research because ARs play such a vital role in hydrological resource management, significantly impact commerce, and are foundational to local industry including winter recreation, and changes in AR characteristics could be highly impactful in these areas.

The global average temperature for the period 2081-2100 is expected to be between 2.6° to 4.8°C warmer than the 1986-2005 period under RCP 8.5 (Representative Concentration Pathway 8.5), the "business as usual" emissions-based scenario developed by the Intergovernmental Panel on Climate Change (IPCC). Studies predict that this increase in global average temperature will drive profound changes in global weather patterns including changes in the mean location and speed of jet streams, changes in

precipitation patterns, increases in the frequency and intensity of heat waves, and changes in the distribution and seasonality of sea ice, carrying associated feedbacks and implications. Increasing temperatures and changes in global weather patterns will likely affect the distribution and intensity of ARs, with potentially large hydrological implications for locations in the western United States, particularly for mountainous regions like Donner Summit in the Sierra Nevada near Lake Tahoe.

A number of studies have set out to increase our understanding of how global warming affects ARs (Dettinger 2011, Dominguez et al. 2018, Espinoza et al. 2018, Payne et al. 2020, Singh et al. 2018, Warner et al. 2015). A recent review of the projected response of ARs to climate change breaks down the projected responses into two categories: thermodynamic and dynamic (Payne et al., 2020). Thermodynamic changes relate to how future changes in atmospheric temperature and humidity would affect ARs. This relationship is well-understood and is governed by the Clausius-Clapeyron relationship (Payne et al. 2020). In contrast, dynamical changes are less constrained when compared to thermodynamic changes. For example, changes in global circulation patterns as a result of global warming determine the climatological frequency of AR landfall at a given latitude. These changes are best addressed using global and regional climate models, but are still poorly constrained and under-researched for many areas of the world (Payne et al. 2020). This contributes to uncertainty in future impacts of ARs in a warming world.

As for the thermodynamic changes, as global temperatures increase, Clausius-Clapeyron predicts a near-exponential scaling of atmospheric moisture. This could result in increases in the intensity of AR precipitation and flooding (Dettinger 2011). Locations along the US West Coast are expected to see an increase in the number of days with integrated vapor transport (IVT) in the 99th percentile by up to 290% by the period 2070 – 2099 as compared to 1974 – 2004 (Warner et al. 2015). This is particularly significant in mountainous regions where geographic barriers force air to rise and cool, resulting in condensation and precipitation. For instance, in the Sierra Nevada, windward slopes experience up to four times the amount of precipitation during an AR when compared to relatively flat areas upstream (Hecht et al. 2017). However, due to expected global warming thermodynamic influences, air will need to be lifted to a higher altitude in order to reach condensation, which may move the spatial pattern of precipitation downwind (Siler & Roe 2014). This could feasibly result in higher precipitation totals closer to the lee-side of mountains, which includes the Eastern Sierra. These sentiments are echoed by Payne et al. (2020), who note that high-resolution simulations are needed to study the complexity of future AR impacts in mountainous regions.

Temperatures of ARs making landfall on the US West Coast have been increasing since the 1980s according to a 2019 study by K. R. Gonzales. Increases in the temperature of landfalling ARs are expected to increase the ratio of rain to snow for many locations (Leung et al. 2004). However, this relationship is nuanced, as the highest mountainous locations are high enough that their winter temperatures remain subfreezing, and their precipitation remains frozen despite the overall pattern of global warming,

including warmer ARs. These findings suggest an increase in the elevation of the rain-snow line for many Sierra Nevada mountain locations. Future ARs may also exhibit greater width and length in a warmer climate (Espinoza et al. 2018), which could result in more precipitation for a given location in a given atmospheric river.

The current research seeks to explore how the manifestation of atmospheric rivers changes in a warmer climate and how, meteorologically, those changes may impact the Sierra Nevada near Donner Summit. Individual, historic atmospheric rivers of strengths ranging from weak to exceptional, as described in the Methods section of this paper, were included in this study. Using atmospheric modeling techniques, these ARs were simulated under a global warming scenario (RCP8.5 for the period 2071-2100) in order to investigate how precipitation and snowpack characteristics may change if the current warming trend for ARs making landfall in California continues. Based on the current literature, an increase in the ratio of rain to snow, a higher rain-snow line, and an increase in AR IVT intensity in the Sierra Nevada near Donner Summit are expected.

Data and Methods

Identifying Historic ARs and Associated Precipitation Characteristics

In order to quantify the changes in AR characteristics under climate change simulations, the attributes of present-day atmospheric rivers must first be characterized. To accomplish this, measurements from land-based weather and climate stations were

utilized, allowing for a baseline to be constructed, against which future AR simulations may be compared.

Land-based observations of the atmosphere, precipitation, and snow water equivalent (SWE) were obtained from the snow telemetry (SNOTEL) sites depicted in Figure 1 and Table 1. These SNOTEL stations were selected to represent the Sierra Nevada northwest of Lake Tahoe, near Donner Summit, for the purpose of assessing meteorological characteristics in this region. Trends in average monthly temperature, maximum SWE for the month, and average monthly snow to rain ratio are shown (Appendix 1 – Initial Analysis of January SNOTEL Trends) for the month of January for each site for their respective periods of record. These sites each show significant warming trends in monthly average temperature. The Central Sierra Snow Lab (CSSL) and Squaw G.C. also show a decrease in snow water equivalent (SWE) and snow-to-rain ratio over time; plausible consequences of warmer ARs. The Independence Lake SNOTEL site does not show this decrease in SWE and snow-to-rain ratio over its period of record. This is likely due in part to the fact that the Independence Lake site is at a higher elevation than the CSSL and Squaw Valley G.C sites, and while temperatures have increased, they likely have not increased so much as to affect the snowpack characteristics at this higher-altitude location. The differences in SWE and snow-to-rain ratio patterns for the Independence Lake SNOTEL site as compared to the other SNOTEL stations could also relate to its geographic location with respect to the Sierra crest, along with related differential storm dynamics. In addition, changes in precipitation characteristics and spatial patterns directly attributable to the warming climate cannot be ruled out.

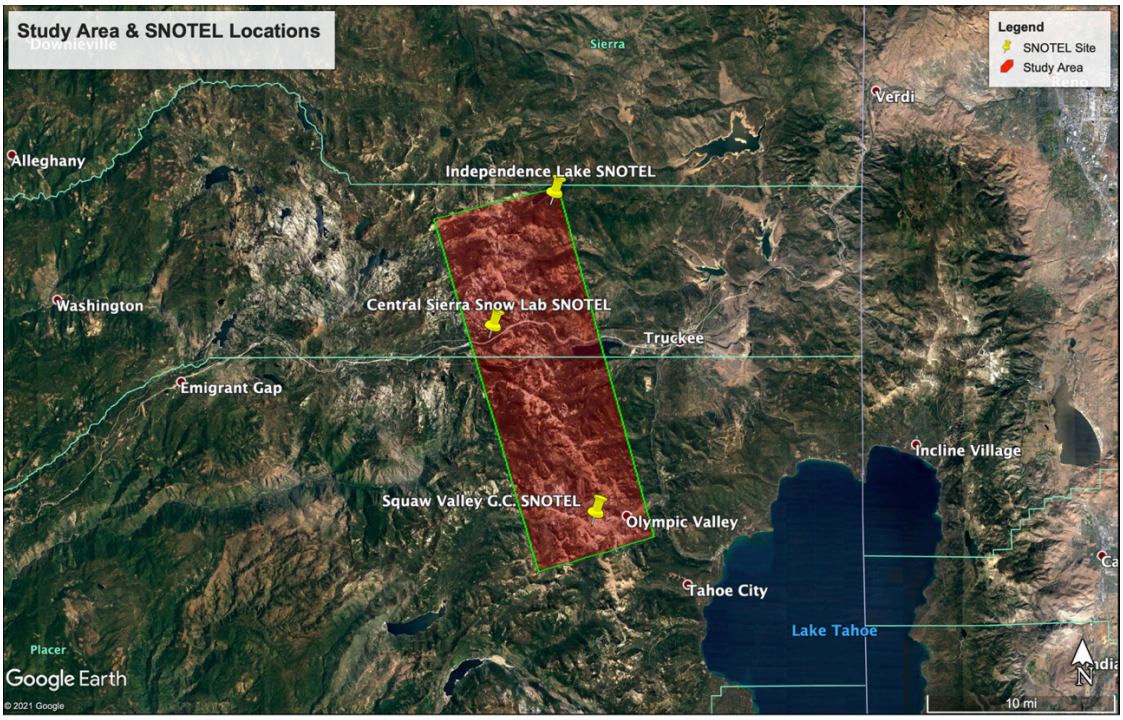

Figure 1. Map of the study area and SNOTEL stations used in this research. Generated using Google Earth software.

SNOTEL Site Name & ID	Lat/Lon	Elevation	Period of Record
Central Sierra Snow Lab (428)	39.33, -120.37	6894 feet	1980 - present
Squaw Valley G.C. (784)	39.19, -120.27	8013 feet	1979 – present
Independence Lake (541)	39.43, -120.31	8338 feet	1978 - present

Table 1. SNOTEL Stations considered for analysis presented along with their location, elevation, and period of record. Source: NRCS SNOTEL

Not all ARs are created equal. AR strength is often assessed using integrated vapor transport (IVT), a measurement of atmospheric moisture flux. AR strength categories based on IVT and the duration of time for which a location is subjected to IVT above a certain threshold are established in the *New Scale to Characterize Strength & Impacts of Atmospheric Rivers* (Ralph et al. 2019). One AR from each of the five categories was included in this analysis in order to observe the current range of

meteorological impacts from ARs under recent climate conditions. The ARs analyzed in this research, listed in Table 2, were recorded and categorized by the Center for Western Weather and Water Extremes (CW3E). For this analysis, if an atmospheric river impacts an area along the California coast at a heading between 220° (southwest) and 270° (west) from any of the SNOTEL stations considered in this report, it was eligible for inclusion in this study. This corresponds to coastal latitudes between 37.15°N and 39.43°N. In addition, the AR was required to produce precipitation in the vicinity of Donner Summit. Impacts from one AR may be experienced at different category levels by different locations along the West Coast at different times. The category of atmospheric rivers fulfilling the latitudinal criteria was determined by the highest category observed along the eligible latitude range during that AR event.

AR Category	AR Date	WRF Simulation Period
5	February 7, 2017	February 4 – February 12, 2017
4	January 8, 2017	January 5 – January 11, 2017
3	February 25, 2019	February 22 – February 28, 2019
2	February 2, 2019	January 30 – February 3, 2019
1	February 2, 2017	January 30 – February 5, 2017

Table 2. Listing of the atmospheric rivers included in this study, their intensity category, the date of first AR precipitation for the Donner Summit domain, and the WRF simulation period for each AR.

Simulating Identified ARs and Evaluating Model Performance Using Observed Precipitation & Snowpack Characteristics

Atmospheric modeling was conducted using the Advanced Research WRF (ARW) dynamical core, version 4.1, with three nested domains, the innermost with a

resolution of 1 km, the second with a resolution of 3 km, the third with a resolution of 9 km, and the outer domain with a resolution of 27 km (see Figure 2). Thompson microphysics (MP) and YSU planetary boundary layer (PBL) parameterization schemes are used, consistent with the West-WRF model that is used by CW3E to study and model atmospheric rivers (Martin et al., 2018). Simulations were run for the AR events listed in Table 2. The WRF model is initialized with ERA5 data, the latest climate reanalysis produced by the European Centre for Medium-Range Weather Forecasts (ECMWF).

Simulated station data obtained from the WRF model for the AR events in Table 2 are compared with observations from the SNOTEL stations listed in Table 1 for the same AR events. Agreement between the WRF model simulated station data and the in-situ observations are then evaluated. Meteorological variables considered in the evaluation include precipitation rate (liquid equivalent), total precipitation, duration of precipitation event, and the station temperature.

These initial AR simulations for each strength category serve as the control simulations (hereafter referred to as “Control”). The same WRF configuration was then used in the next phase of the research, where climate change “deltas” or perturbations were applied to the lateral and initial boundary conditions for the ARs, and the differences between the present day (control) and climate change model simulations are evaluated.

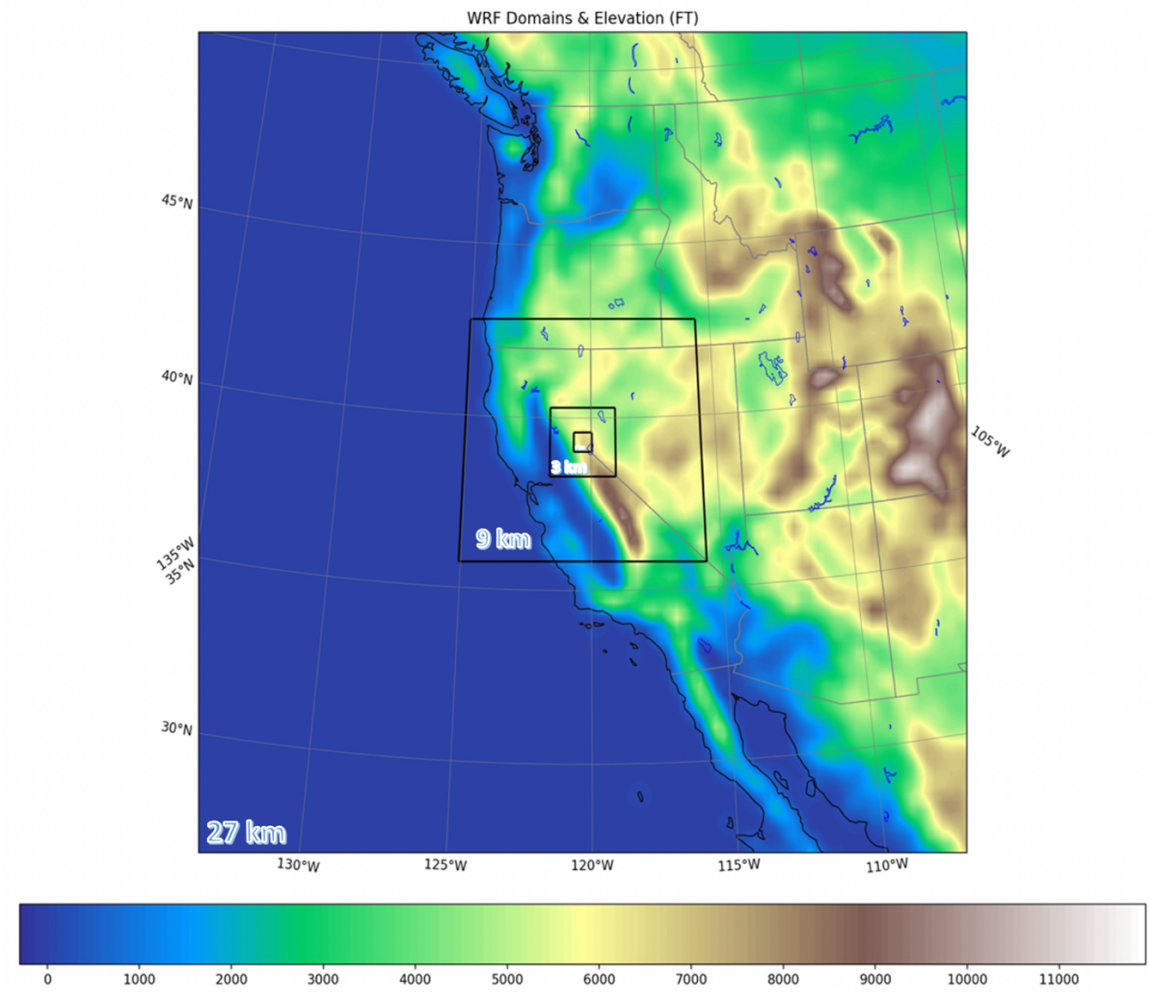

Figure 2. Domains 1, 2, 3, and 4 with grid sizes 27 km, 9 km, 3 km, and 1km, respectively.

Using WRF with Future Climate Predictions to Estimate Changes in Precipitation & Snowpack Characteristics Associated with the Historic ARs

To simulate the ARs under a warmer climate scenario (RCP8.5), the pseudo-global warming (PGW) method was used. PGW utilizes temperature "deltas," average temperature differences between a future climate scenario and a characterization of current conditions, in order to perturb the WRF initialization data to simulate climate change. It should be noted that in the PGW method, relative humidity (RH) is held at the historical value in the initialization dataset in order to allow for saturation to be present in

the initial and boundary conditions. WRF is initialized using RH, which is a computationally efficient process that eliminates the need to calculate specific humidity deltas independent of the WRF model calculations. Within the WRF model, specific humidity is calculated for every grid cell and pressure level based on Clausius-Clapeyron scaling and the ambient temperature. Specific humidity increases (decreases) by approximately 7% per degree Celsius as temperature increases (decreases) (Singh et al. 2018). Once ingested by the WRF model, however, the relative humidity is free to fluctuate.

The PGW method has been used in over 700 prior studies according to search results from Google Scholar. PGW has been used to study the effects of the future projected changes in climate on a diverse number of processes ranging from changes in hurricanes (Gutmann et al. 2018) and midlatitude cyclones in the North Atlantic (Michaelis et al. 2017), to changes in Colorado snowfall and runoff (Rasmussen et al. 2011). PGW has also been used to study future ARs under global warming scenarios in studies including Dominguez et al. (2018), and Singh et al. (2018).

Dominguez (2018) and Singh (2018) use Coupled Model Intercomparison Project Phase 5 (CMIP5) GCM data in order to calculate their temperature deltas. Both studies used a 3 km grid size in their innermost domain, while the present study utilizes a higher resolution 1 km grid. Singh studied a total of five AR events spanning a period from 1980 to 2010. Dominguez studied a single event taking place on December 3, 2007. Using PGW to study individual events for a particular location has been found to be useful to

quantify the possible impacts for members of that community. In part, this is because the past events may be memorable to members of the affected community, and the simulations can be explained simply via the narrative "this is what these events could look like under global warming scenarios" (Dominguez et al. 2018). According to Singh (2018), the PGW approach accounted for both thermodynamic and dynamic changes in individual future ARs under global warming scenarios. However, changes in overall global circulation patterns are not accounted for in most PGW studies, the present study included.

In the present work, a GCM from CMIP5, the Community Climate System Model version 4 (CCSM4), was used to calculate temperature deltas between the periods 2071-2100 and 1971-2000 for the months December, January, and February (DJF). The 26 vertical levels of the CCSM4 output were interpolated to the 37 vertical levels in ERA5 data in addition to land surface temperatures, sea surface temperatures, and soil temperatures (see Table 3). These deltas were applied to the ERA5 reanalysis data that was used as lateral and initial boundary conditions for the WRF model. The WRF model was then run with these deltas applied, simulating how the atmospheric rivers could manifest under RCP 8.5 conditions during the period 2071-2100.

Control and simulations PGW simulations are then evaluated and compared. Specifically, changes in event IVT, mixing ratio, wind speed and direction, total event precipitation, and elevation of the freezing level, and extent of terrain above/below the

freezing line are investigated for each strength category. Finally, the potential implications and impacts of the changes in AR characteristics are assessed.

Delta Summary Statistics

RCP8.5 Ambient Temperature Delta Statistics (TA) (2071 – 2100)			
Level	Minimum	Mean	Maximum
hPa	K	K	K
10	-13.847	-6.9712	-2.808
20	-10.661	-5.1913	-1.688
30	-8.8614	-4.2901	-1.2256
50	-7.0349	-3.3284	-0.44573
70	-5.9621	-2.0128	0.054548
100	-4.5569	0.58644	3.1568
125	-4.2682	0.81261	4.1559
150	-4.0361	1.0388	5.4894
175	-3.3182	1.522	5.7957
200	-2.6161	2.0052	6.1245
225	-1.2899	2.67	6.0477
250	0.018885	3.3348	6.0996
300	1.652	3.9666	5.9415
350	2.1068	4.0284	5.4167
400	2.4564	4.0902	5.2691
450	2.4803	3.9676	5.1447
500	2.4839	3.8451	5.035
550	1.8263	3.7502	5.1978
600	-0.94467	3.6394	6.0752
650	-0.94467	3.6166	6.0752
700	0	3.4112	8.303
750	0	3.4069	8.303
775	0	3.4048	8.303
800	-0.72085	3.1859	8.2497
825	-1.915	3.1838	9.4174
850	-3.1091	3.1817	10.585
875	-3.1091	3.2684	10.585
900	0	3.1228	14.612
925	-1.0828	3.2096	19.238
950	-1.0828	3.3919	19.238
975	-3.1734	2.5407	19.847
1000	-6.3237	2.723	26.403

RCP 8.5 Temperature Delta Statistics (2071-2100)			
Parameter	Minimum (K)	Mean (K)	Maximum (K)
Ocean Surface Temperature (TOS)	-1.196	2.139	7.635
Surface Temperature (TS)	-0.410	4.959	21.785
2-Meter Temperature (TAS)	0.684	4.911	20.211

RCP8.5 Soil Temperature Delta Statistics (TSL) (2071-2100)			
Depth/Level	Minimum	Mean	Maximum
m	K	K	K
.035	0.000	1.430	17.180
.175	0.000	1.445	16.814
0.640	-0.363	1.462	15.875
1.775	-0.156	1.513	13.688

Table 3. Deltas calculated from the CCSM4 GCM for average DJF RCP8.5 conditions for the period 2071-2100 less the period 1971-2000.

Results and Discussion

Evaluating WRF Control Simulations vs Observation and Reanalysis Data

IVT and Synoptic Meteorology

WRF Control IVT and synoptic conditions (500 hPa geopotential height and 700 hPa wind) were compared to ERA5 Reanalysis data for each AR. The purpose of this analysis was to determine how well the WRF Control simulation reproduced each AR in terms of strength, spatial extent, timing, and synoptic-scale pressure and wind fields. This

analysis assumes that the ERA5 Reanalysis is an accurate depiction of IVT and synoptic conditions for the ARs featured in this study.

Figures Figure 3 to Figure 7 present WRF Control vs ERA5 IVT, 500 hPa geopotential height, and 700 hPa winds for AR Cat 1-5. A visual analysis of the WRF Control IVT magnitude, spatial extent, and timing for the ARs reveals a reasonable fit to the ERA5 reanalysis depictions, especially in reference to the study area. A similar analysis of the 500 hPa broad scale weather patterns reveals a particularly close fit of the geopotential height and locations of the low pressure centers associated with the ARs. The 700 hPa wind fields, both in terms of direction and magnitude, also portray a reasonable visual fit for the ARs, although peak wind speeds in the WRF Control simulation are on average 5 knots below the ERA5 values. AR Cat 5, the strongest AR in this study, exhibited the best visual fit when compared to the ERA5 reanalysis IVT strength, spatial extent, and timing. This comparison is shown in Figure 3. At 12:00 UTC on February 7, 2017, the time depicted, the maximum IVT value of 1133 kg m^{-1} s^{-1} is within 2.5% of the ERA5 maximum value of 1162 kg m^{-1} s^{-1}. The orientation of the moisture plume is captured reasonably well and the 700 hPa wind magnitude and direction are in generally close agreement with the ERA5 reanalysis, although WRF Control peak wind speed for the AR is approximately 5 knots below the ERA5 value.

A similar analysis was performed for AR Cat 1, 3, and 4 revealed a similar fit of synoptic-scale IVT, 500 hPa pressure, and 700 hPa winds between the WRF Control and ERA5 reanalysis. For AR Cat 4 (Figure 4) at 00Z on January 9, 2017 the WRF Control

IVT value of 743 kg m^{-1} s^{-1} is 17.2% lower than the ERA5 maximum value of 897 kg m^{-1} s^{-1}. For AR Cat 3 (Figure 5) at 00Z on February 27, 2019 the WRF Control IVT value of 620 kg m^{-1} s^{-1} is 20.4% below the ERA5 maximum value of 779 kg m^{-1} s^{-1}. For AR Cat 1 (Figure 7) at 12Z on February 2, 2017 the WRF Control IVT value of 363 kg m^{-1} s^{-1} (the maximum IVT value for the landfalling AR, rather than for the entire domain was used) is approximately 21.8% below the ERA5 maximum value of 464 kg m^{-1} s^{-1}. The ERA5 and WRF Control AR locations and orientations were in reasonable agreement, while the IVT was lower in the WRF simulations. The lower IVT in the WRF Control simulations was hypothesized to be related to an interaction of three factors: 700 hPa peak wind speeds depressed by an average of 5 knots (all ARs), shallower depth of moisture plumes (AR Cat 4 & 1), and a slightly cooler lower troposphere (all ARs).

The WRF Control simulation for AR Cat 2 appears to have simulated the moisture plume further south than the ERA5 reanalysis (see Figure 6). In addition, the peak IVT value of 745 kg m^{-1} s^{-1} at 12:00 UTC on February 2, 2019, the time depicted, is 24% less than the ERA5 IVT value of 985 kg m^{-1} s^{-1} for the reasons described above. The WRF Control AR Cat 2 wind and pressure fields, however, are aligned with the ERA5 reanalysis data. Despite the differences in the moisture plume location between ERA5 and WRF, the simulated AR is still representative of the types of winter weather systems that currently affect the U.S. West Coast and the study area defined in this paper.

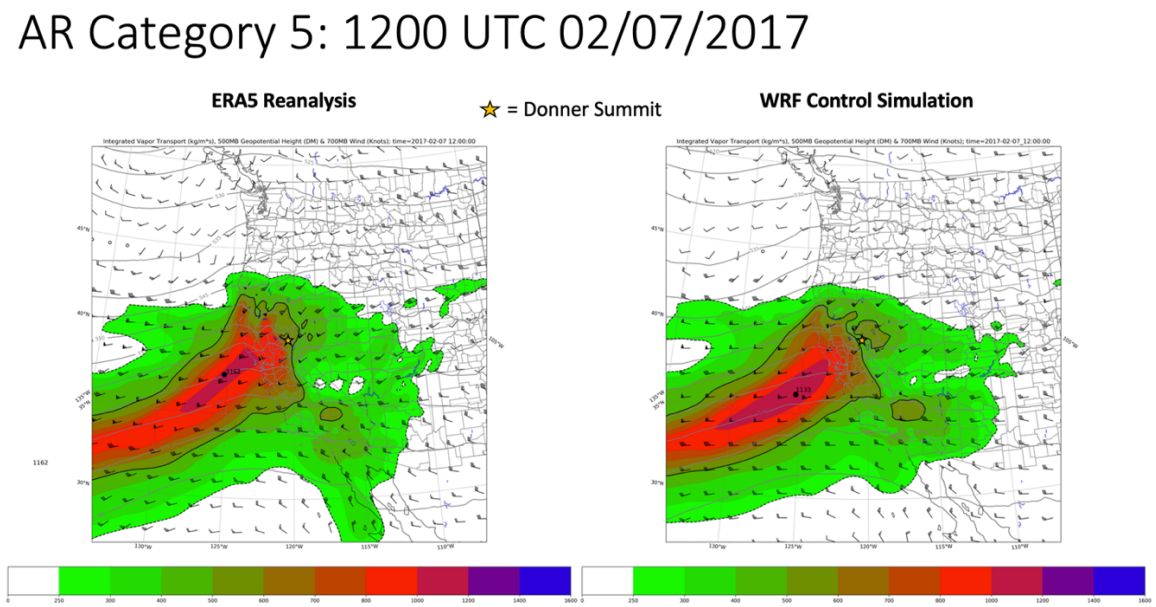

Figure 3. ERA5 vs WRF Control IVT for AR Cat 5. The center of the study area (Donner Summit in the Sierra Nevada Mountains of California) is indicated by the gold star outlined in black.

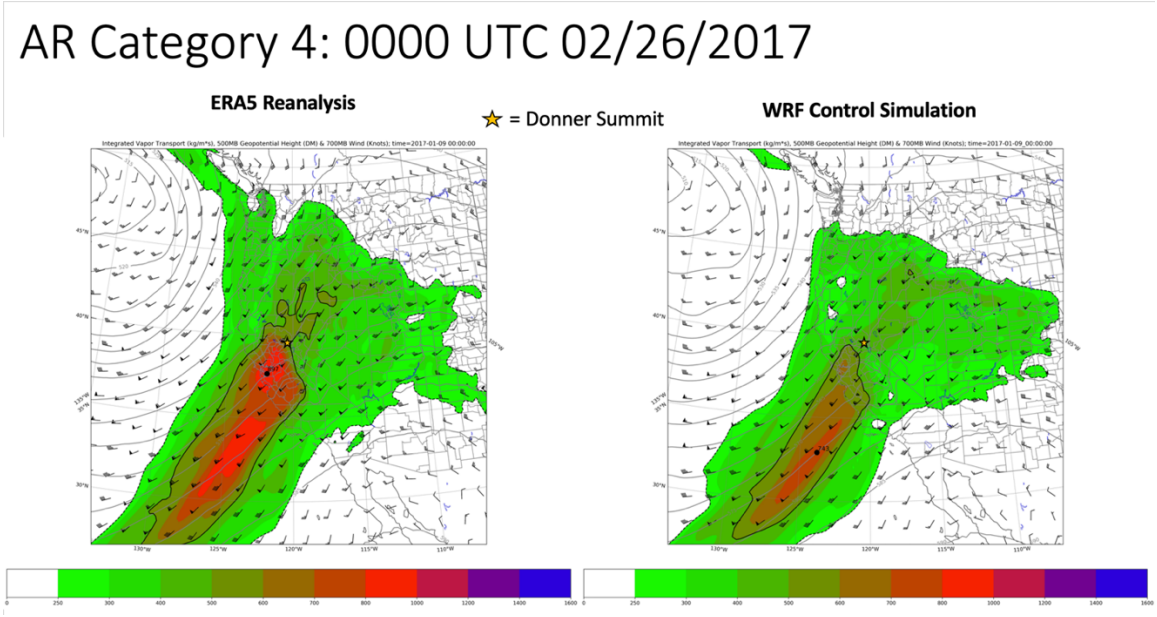

Figure 4. ERA5 vs WRF Control IVT for AR Cat 4. The center of the study area (Donner Summit in the Sierra Nevada Mountains of California) is indicated by the gold star outlined in black.

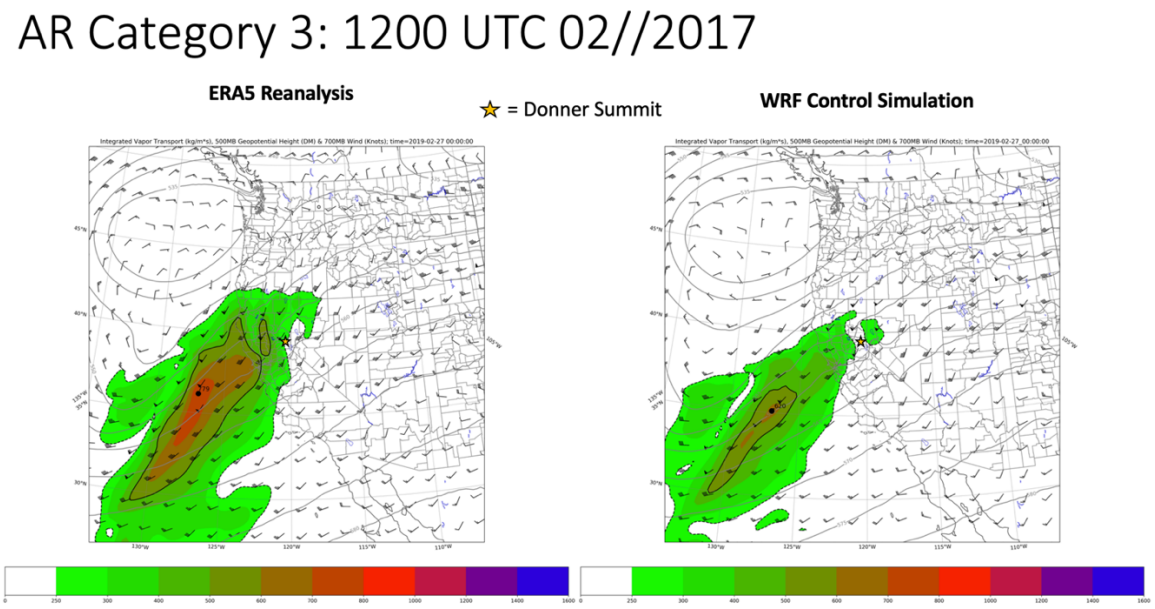

Figure 5. ERA5 vs WRF Control IVT for AR Cat 3. The center of the study area (Donner Summit in the Sierra Nevada Mountains of California) is indicated by the gold star outlined in black.

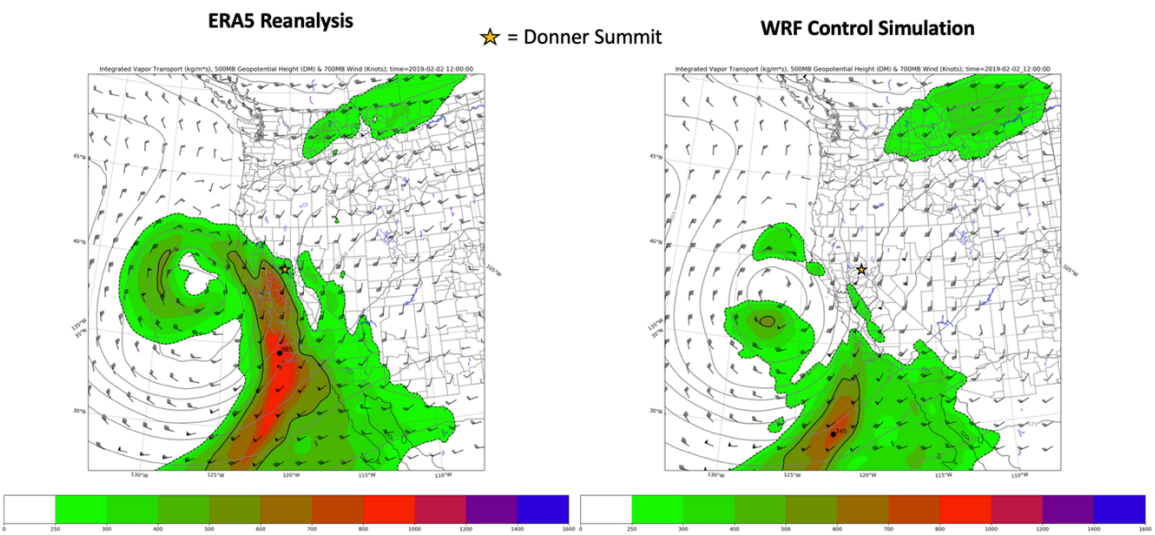

Figure 6. ERA5 vs WRF Control IVT for AR Cat 2. The center of the study area (Donner Summit in the Sierra Nevada Mountains of California) is indicated by the gold star outlined in black.

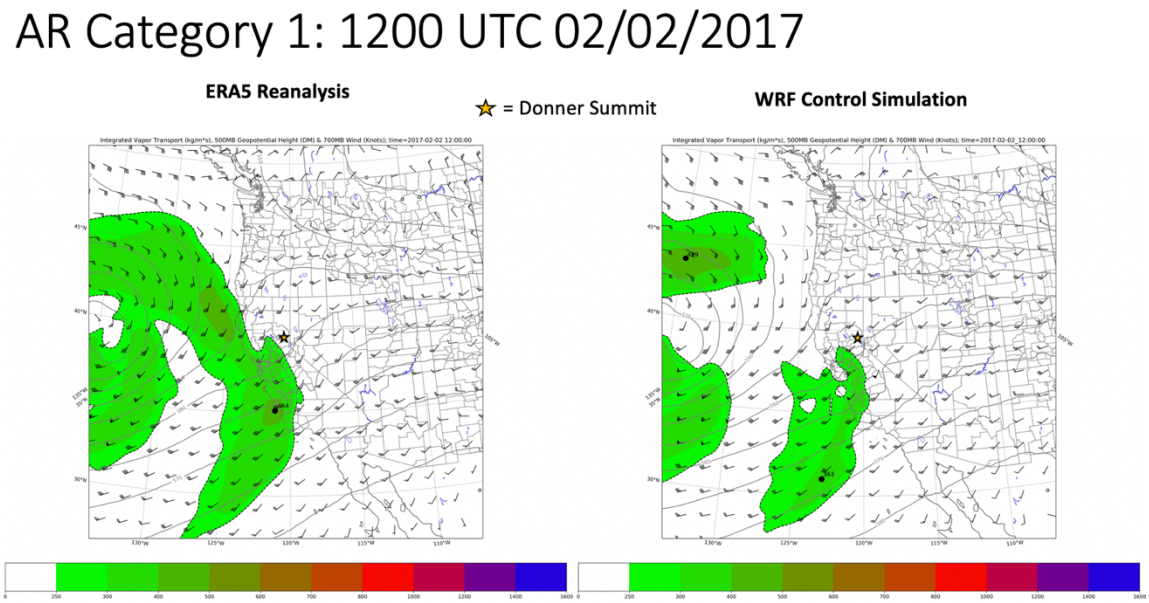

Figure 7. ERA5 vs WRF Control IVT for AR Cat 1. The center of the study area (Donner Summit in the Sierra Nevada Mountains of California) is indicated by the gold star outlined in black.

Precipitation

WRF Control total precipitation (Domain-2) for each AR was compared with the PRISM 4-km precipitation dataset (PRISM Climate Group) to assess the fit of the broad-scale precipitation characteristics between the WRF Control simulations and a dataset generated from surface-based precipitation observations. It should be noted that AR precipitation in the mountains is primarily orographic in nature, and so it is unsurprising that in Domain-2 (with a spatial resolution of 9 km) the WRF Control precipitation is systematically less than the PRISM precipitation, as terrain complexity is dampened. In addition, PRISM utilizes a slope regression methodology that can produce unrealistic precipitation totals in some locations. The purpose of this analysis, however, was to identify and visually compare the overall precipitation patterns to determine how well the

ARs were simulated in this regard. WRF Control precipitation for Domain-4, with a spatial resolution of 1 km, was used to assess the agreement of the WRF simulations with SNOTEL surface observations and will be discussed below.

The precipitation comparison for AR Cat 5, the AR best-simulated in terms of IVT, is shown in Figure 8. Visual analysis of the WRF Control and PRISM precipitation distribution and amounts reveals a reasonable fit, with similar precipitation maxima over the Sierra Nevada, the Southern Coast Ranges, Northern Coast Ranges, Klamath Mountains, and volcanic locations. Precipitation shadowing was captured by the WRF Control simulation as well, with drop-offs in precipitation to the east of the major orographic barriers. Despite the relatively coarse spatial resolution of Domain-2, the WRF Control simulation captured the magnitude of the total precipitation reasonably well, especially in areas not featuring complex topography. Even in the vicinity of the study area, which *is* characterized by complex terrain, the domain 2 WRF Control simulation captured the overall magnitude of the precipitation. Precipitation for AR Cat 1-4 exhibited similar patterns, and are shown in Appendix 4.

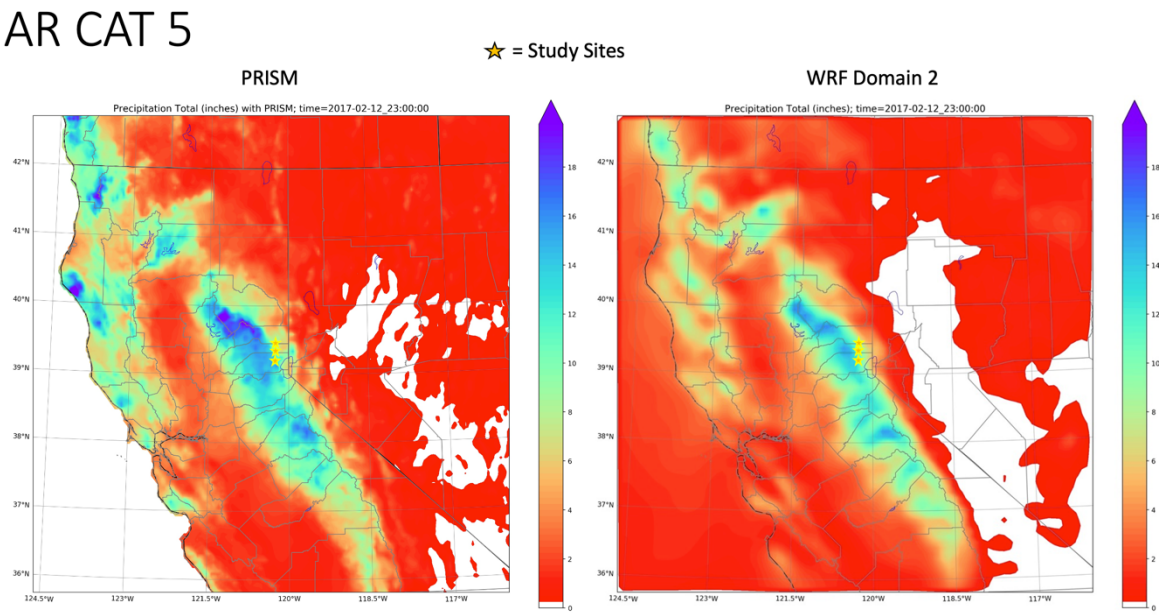

Figure 8. Comparison between WRF-Control Domain-2 precipitation and PRISM precipitation for AR Cat 5.

For the high-resolution innermost domain (Domain-4, 1 km spatial resolution), WRF Control precipitation was compared with SNOTEL observations using WRF-simulated station observations. Increases in SWE were used to represent accumulating precipitation due to observed issues with SNOTEL rain gauge measurements during the ARs in this study. Given a sufficient snowpack, liquid-phase precipitation is incorporated or frozen into the snowpack, presenting as an increase in SWE to the SNOTEL station (Lundquist et al., 2008, Lundquist et al., 2015). For this study, the assumption is made that a sufficient snowpack was in place at the beginning of each AR to incorporate liquid precipitation, as the minimum depth of the snowpack at the beginning of an AR was 68 inches. The primary phase of precipitation for the observed ARs was frozen-phase, but any liquid-phase precipitation was likely incorporated into the snowpack.

The results of this analysis are presented in Table 4. In order to represent the geographic extent and range of altitudes of the study area, data from the individual SNOTEL sites (and WRF-simulated station data) were merged into a Superstation index. This Superstation index is useful in that it represents conditions within the study area with a single number, allowing for easy comparisons between WRF and SNOTEL variables.

In contrast to the 9 km Domain-2 precipitation simulations, high-resolution weather models can overpredict precipitation, especially in the complex terrain of the Sierra Nevada (Holtzman et al., 2017), although this can vary by event or even year-to-year depending on the timescale considered, and also the microphysics scheme used. The WRF Control for AR Cat 3-5 simulated precipitation on the order of 15% higher than SNOTEL precipitation observations. AR Cat 2 precipitation was overestimated by approximately 25% with the WRF Control model despite the maximum IVT being simulated to the south. The AR Cat 1 precipitation was underestimated by the WRF Control by approximately 7% compared to the SNOTEL observations. Potential sources of error for this analysis include the SNOTEL method of accounting for total precipitation using SWE and sources of error innate to the observation of frozen precipitation accumulation.

SNOTEL Comparison – Model Evaluation

Precipitation

AR Category	SNOTEL Total Precip (*SWE Method)	Model Total Precip (Control)	% Difference
Category 5 (Feb. 5 – 12, 2017)	CSSL: 7.8 inches Independence Lake: 12.7 inches Squaw GC: 15.4 inches **Superstation: 11.97 inches**	CSSL: 14.01 inches Independence Lake: 12.76 inches Squaw GC: 15.51 inches **Superstation: 14.09 inches**	**15.09%**
Category 4 (Jan. 6 – 11, 2017)	CSSL: 10.77 inches Independence Lake: 16.0 inches Squaw GC: 11.8 inches **Superstation: 12.86 inches**	CSSL: 12.56 inches Independence Lake: 14.14 inches Squaw GC: 18.96 inches **Superstation: 15.22 inches**	**15.53%**
Category 3 (Feb. 23 – 28, 2019)	CSSL: 9.2 inches Independence Lake: 9.0 inches Squaw GC: 4.4 inches **Superstation: 7.53 inches**	CSSL: 8.79 inches Independence Lake: 8.55 inches Squaw GC: 8.74 inches **Superstation: 8.69 inches**	**13.34%**
Category 2 (Jan. 31 – Feb. 3, 2019)	CSSL: 3.3 inches Independence Lake: 2.8 inches Squaw GC: 2.6 inches **Superstation: 2.9 inches**	CSSL: 3.67 inches Independence Lake: 3.09 inches Squaw GC: 4.9 inches **Superstation: 3.89 inches**	**25.39%**
Category 1 (Jan. 31 – Feb. 5, 2017)	CSSL: 4.8 inches Independence Lake: 3.8 inches Squaw GC: 3.2 inches **Superstation: 3.93 inches**	CSSL: 3.58 inches Independence Lake: 2.9 inches Squaw GC: 4.59 inches **Superstation: 3.69 inches**	**-6.59%**

Table 4. SNOTEL-observed AR precipitation and WRF Control Domain-4 precipitation simulations are reported in this table for each AR and each SNOTEL station evaluated in this study. Superstation data represent the 3-station (CSSL, Squaw GC, and Independence Lake) average. Percent difference is calculated with respect to SNOTEL observations.

Oakland Radiosonde and WRF Soundings

WRF model soundings were compared with Oakland radiosonde observations in order to assess how well the WRF Control configuration depicted the arrival of AR moisture at the California coast. Temporal cross sections were created using the 00 UTC and 12 UTC Oakland radiosonde data. Corresponding WRF model soundings were retrieved for the same times. Both radiosonde and WRF soundings include temperature, pressure, wind, and atmospheric moisture data. These variables drive many of the atmospheric dynamics that determine the strength of atmospheric rivers; thus, a comparison of these variables is useful in determining how well an atmospheric river has been simulated.

The AR Cat 4 comparison, shown in Figure 9, featured the best fit between the WRF Control and the Oakland soundings with similar profiles of atmospheric

temperature, moisture, and wind speed and direction. The mixing ratio is depicted by the color-filled contours, atmospheric temperature is shown using the dashed isotherms with the 0°C isotherm bolded, and wind barbs show the wind speed and direction at the different atmospheric levels plotted in knots. The WRF model comes in slightly moister, but the timing and depth of the moisture plumes are captured reasonably. Upper-air temperature and wind profiles for the Oakland and WRF soundings exhibit a particularly close fit. Similar levels of fit between the Oakland and WRF sounding data were found for the other AR events studied. All Oakland vs WRF sounding comparisons are included in Appendix 5.

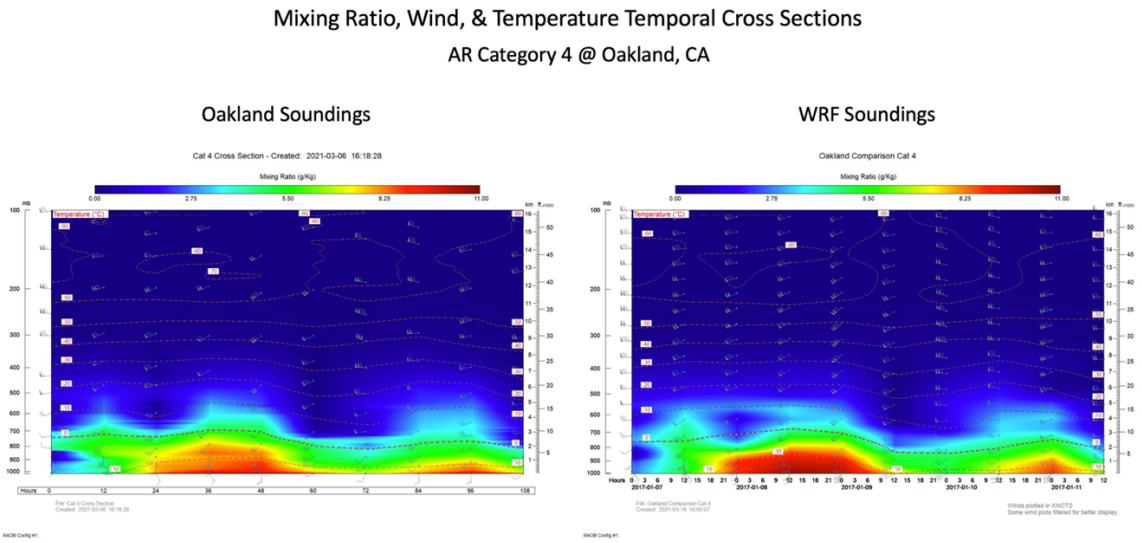

Figure 9. Temporal cross section of vertical profiles of temperature (isotherms) in °C, wind (wind barbs) in knots, and color-filled contours depicting Mixing Ratio in g/Kg for AR Cat 4. Oakland Soundings were launched by the National Weather Service in Oakland, CA, and WRF Soundings are model-derived soundings (Domain-2) for the same times and locations as the Oakland Soundings. Plotted using RAOB software.

Temperature

Temperature data from the SNOTEL sites (2m temperatures) were compared to WRF Control Domain-4 2m temperatures for the same locations for each AR. The purpose of this analysis was to determine how well the WRF Control configuration represents observed surface station temperature for the ARs. WRF and SNOTEL temperatures for each station and AR are provided in Table 5. Average temperatures are the true mean of the temperature observations for the AR rather than the average of the daily high and low temperatures. This approach was selected because it better represents the implications of temperature to precipitation phase and snowpack characteristics than the simple average of the daily high and low temperatures.

WRF Control simulations of 2-m temperature came in lower than the SNOTEL observations, but the bias was relatively consistent. Negative bias in WRF-simulated 2-m temperatures are typical for such simulations, but systematic biases in WRF model 2-m temperature simulations vary both seasonally, diurnally, and geographically (Wyszogrodzki et al., 2013). In this study, the average difference between WRF Control and SNOTEL for a given AR was -2.28 °C. The smaller difference in temperature between the AR Cat 5 SNOTEL and WRF simulation is likely responsible in part for the smaller IVT deficit between the ERA5 and WRF Control, with increasing saturation vapor pressure and mixing ratios governed by the Clausius-Clapeyron relationship. Overall, the WRF Control temperature bias was systematic, predictable, and within the expected magnitude based on the findings of Liu et al. (2009) and Wyszogrodzki et al. (2013) which describe a cold bias of between -4 and -2 °C in the Sierra Nevada. The

systematic nature of the negative temperature bias should not impact the analysis of the changes in individual AR temperatures between the Control and PGW simulations, as the difference in temperature between these conditions is assumed to represent the response of the physical system to the climate change scenario.

SNOTEL Comparison – Model Evaluation

Temperature

AR Category	SNOTEL Average Temp °C	Model Average Temperature °C (Control)	Difference
Category 5 (Feb. 5 – 12, 2017)	CSSL: 1.66 Independence Lake: -0.97 Squaw GC: 0.07 **Superstation: 0.25**	CSSL: -0.81 Independence Lake: -0.02 Squaw GC: -1.39 **Superstation: -0.74**	**-0.99 °C**
Category 4 (Jan. 6 – 11, 2017)	CSSL: -1.17 Independence Lake: -2.97 Squaw GC: -1.63 **Superstation: -1.92**	CSSL: -3.92 Independence Lake: -4.23 Squaw GC: -5.86 **Superstation: -4.67**	**-2.75 °C**
Category 3 (Feb. 23 – 28, 2019)	CSSL: -1.68 Independence Lake: -3.71 Squaw GC: -2.66 **Superstation: -2.69**	CSSL: -4.55 Independence Lake: -4.41 Squaw GC: -6.39 **Superstation: -5.11**	**-2.43 °C**
Category 2 (Jan. 31 – Feb. 3, 2019)	CSSL: 1.7 Independence Lake: 0.17 Squaw GC: 0.41 **Superstation: 0.76**	CSSL: -1.37 Independence Lake: -1.58 Squaw GC: -3.65 **Superstation: -2.2**	**-2.96 °C**
Category 1 (Jan. 31 – Feb. 5, 2017)	CSSL: 0.95 Independence Lake: 0.13 Squaw GC: 1.33 **Superstation: 0.80**	CSSL: -1.24 Independence Lake: -0.75 Squaw GC: -2.42 **Superstation: -1.47**	**-2.28 °C**

Table 5. SNOTEL-observed average temperatures and WRF Control Domain-4 average temperaturess are reported in this table for each AR and each SNOTEL station evaluated in this study. Superstation data represent the 3-station (CSSL, Squaw GC, and Independence Lake) average. Difference is calculated with respect to SNOTEL observations.

PGW – Simulating Changes in Temperature & Precipitation Under RCP8.5

This segment of the research explores the differences in meteorological outcomes between the pseudo-global warming WRF simulations and the control simulations. For the PGW simulation, the same ERA5 initialization files were used as in the WRF Control simulations, except that the DJF temperature deltas (see Appendix 2) have been applied while holding relative humidity equal to that in the original ERA5 files. Aside from the temperature and humidity changes, the initialization files are identical between the PGW

and Control simulations. Within the WRF domains, however, the model is free to simulate as its equations and parameterizations allow. The thermodynamic and dynamic changes between the Control and PGW simulations and their impacts on mountain meteorology in the Sierra Nevada near Donner Summit are the subject of this study.

PGW IVT

The Clausius-Clapeyron relationship dictates that increases in air temperature are accompanied by corresponding increases in the saturation mixing ratio. Thus, where ambient temperatures are increased in the model, the PGW method increases the amount of moisture in the air in order to hold relative humidity constant with respect to the ERA5 initialization dataset. One direct consequence of the PGW method is an increase in AR IVT. This increase in IVT is not incidental, but is considered to be an important aspect of the PGW-simulated climate. While the magnitude of the increases in AR IVT are determined by the model dynamics, the increase in IVT was expected. Changes in AR characteristics, including the increases in IVT, were analyzed with a focus on the potential impact to surface meteorology and snow conditions in the study area defined in this research.

Figure 10 to Figure 14 present WRF Control and PGW IVT comparisons for ARs Cat 1 to 5. As expected, IVT increased in every PGW simulation. For these ARs, the maximum IVT value increased by an average of 31-32% from the Control to the PGW simulation. Clausius-Clapeyron predicts a ~7% increase in saturation vapor pressure per Kelvin as temperature increases, which equates to a 7% increase in the mixing ratio per

Kelvin (Dominguez et al. 2018, Singh et al. 2018). The average temperature delta applied from the surface to 700 hPa was 3.3 Kelvin, so we would expect an overall increase in mixing ratio of approximately 23%. However, IVT depends on both mixing ratio (integrated vertically) and wind speed. It was noted that wind speeds did not significantly change between the Control and PGW simulations, so the additional 9% difference between the Clausius-Clapeyron expected increase in IVT and the simulated increase in IVT is likely accounted for by an increase in the depth of the moisture plume associated with the AR. For all ARs, the increase in IVT from Control to PGW simulation averaged 31.3%. AR IVT comparisons between Control and PGW are shown for all ARs in Appendix 6.

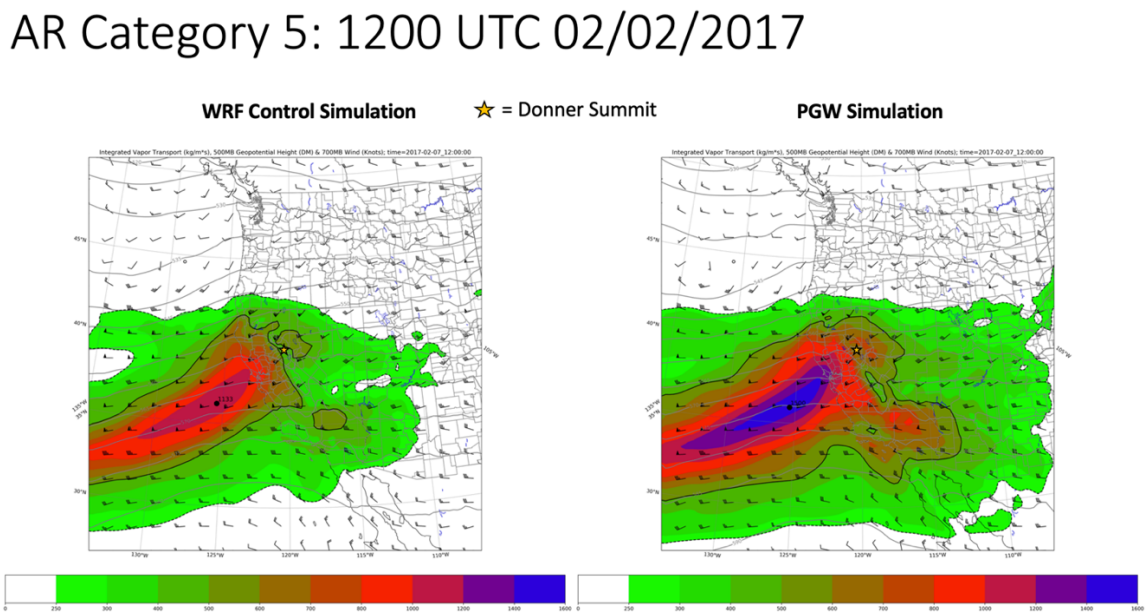

Figure 10. Comparison of WRF Control and PGW simulations of IVT for AR Cat 5 near the time of landfall.

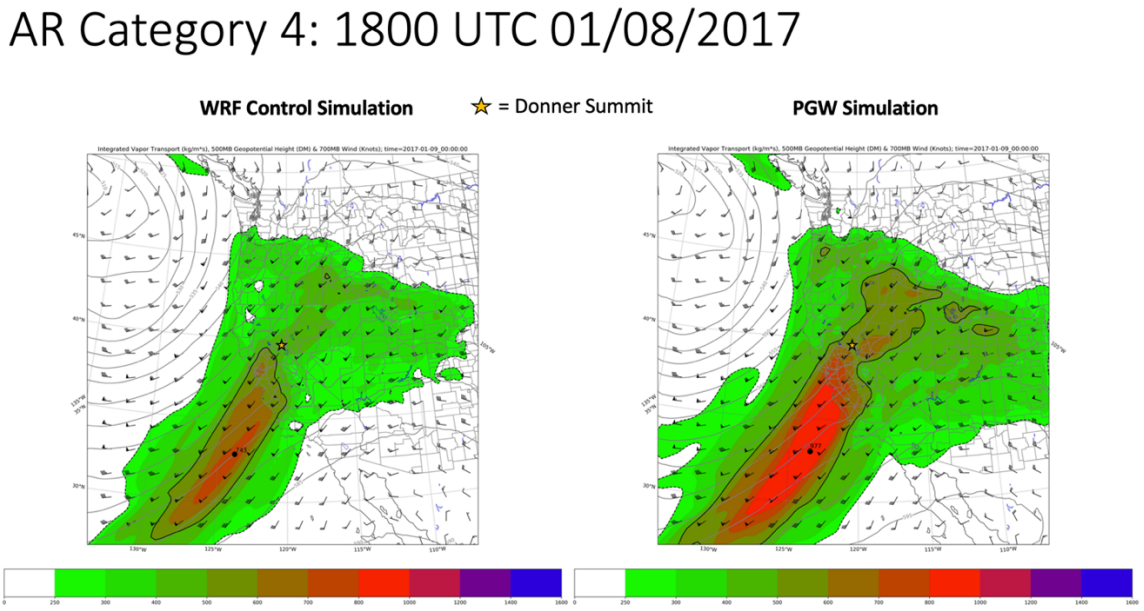

Figure 11. Comparison of WRF Control and PGW simulations of IVT for AR Cat 4 near the time of landfall.

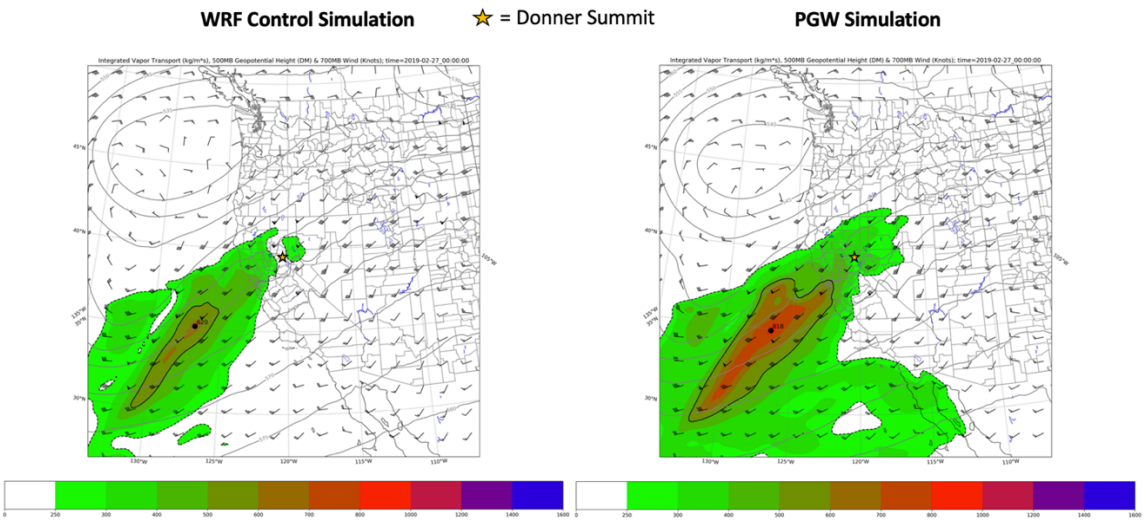

Figure 12. Comparison of WRF Control and PGW simulations of IVT for AR Cat 3 near the time of landfall.

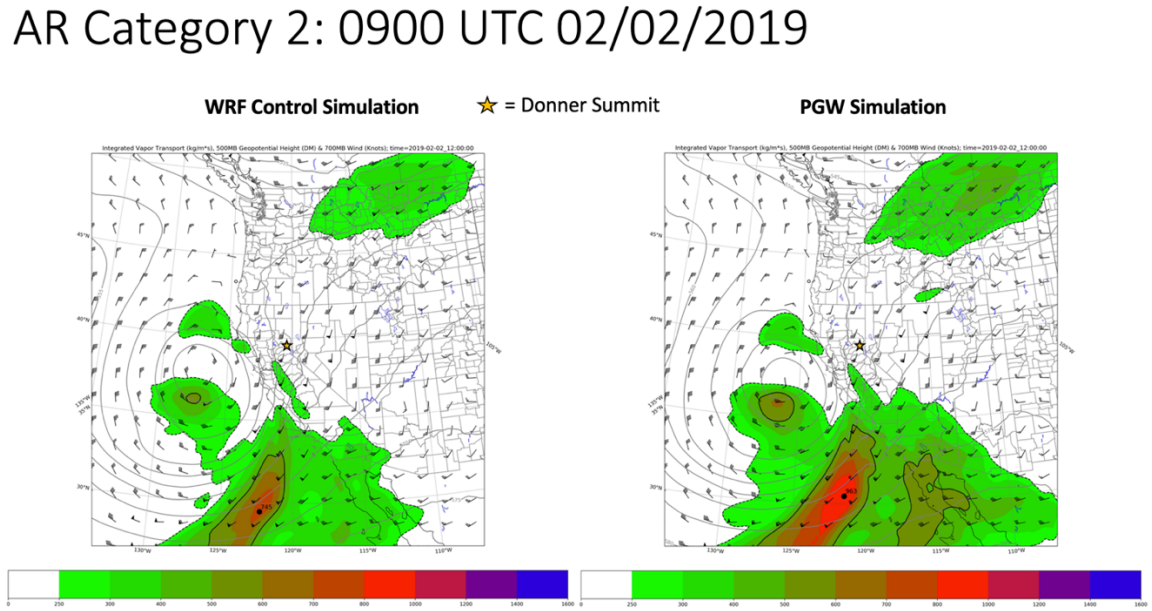

Figure 13. Comparison of WRF Control and PGW simulations of IVT for AR Cat 2 near the time of landfall.

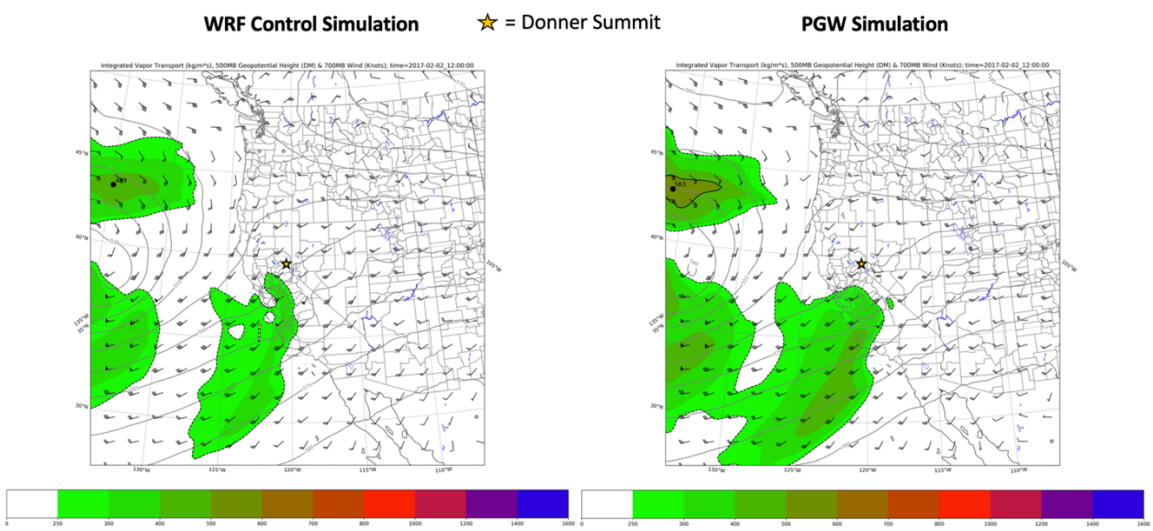

Figure 14. Comparison of WRF Control and PGW simulations of IVT for AR Cat 1 near the time of landfall.

PGW Model Soundings: Central Sierra Snow Lab

Hourly atmospheric soundings were retrieved from the WRF Control and PGW simulations for the location of the CSSL. The CSSL is the proximal center of Domain-4,

and for the purposes of atmospheric sounding analysis is assumed to be representative of the study area. These hourly WRF soundings were used to generate temporal cross sections of atmospheric variables for each AR. Mixing ratio is plotted as color-filled contours. Temperature is plotted with isotherms; the 0°C isotherm is bolded. Wind speed and direction are plotted in knots using wind barbs. The temporal cross section comparison for AR Cat 5 is shown in Figure 15. Temporal cross section comparisons for all ARs studied are provided in Appendix 7. The patterns and trends identified in the AR Cat 5 analysis below are representative of the patterns identified in the other ARs (i.e., increases in mixing ratio, warming temperatures, relatively unchanged wind fields. Table 6 presents the change in the height of the 0°C isotherm for each AR.

Analyzing Figure 15, the significant increase in the mixing ratio from the Control to the PGW simulation for AR Cat 5 is clear. The increase in maximum mixing ratio for the AR is on the order of 20%, which is in line with the Clausius-Clapeyron expected increase. The vertical extent (i.e., depth) of the moisture plume also increased significantly, contributing to the difference between the Clausius-Clapeyron-expected versus PGW-simulated maximum IVT increase discussed in the last section.

Changes in the freezing level (i.e., the height of the 0°C isotherm) for AR Cat 5 can be seen in the figure, with surface temperatures elevated to over 5°C for a number of hours during the peak of the AR. At the same time, the height of the 0°C isotherm increases from approximately 10,000 ft. MSL to approximately 12,000 ft. MSL. This analysis reveals temperatures increasing up through 400 hPa between the Control and

PGW simulations. The average increase in the height of the event-maximum 0°C isotherm from Control to PGW for the ARs in this study was 2,121 ft (see Table 6).

Because the temperature deltas obtained from the CCSM4 climate model vary both geographically and vertically, it is possible for the wind field to change between the Control and the PGW simulations as the atmosphere finds a new hydrostatic and thermodynamic equilibrium. That being said, significant changes in wind speed and direction were not identified at any level in the present study. Differences in wind speed and direction from the surface to over 400 hPa were quite subtle within the study area.

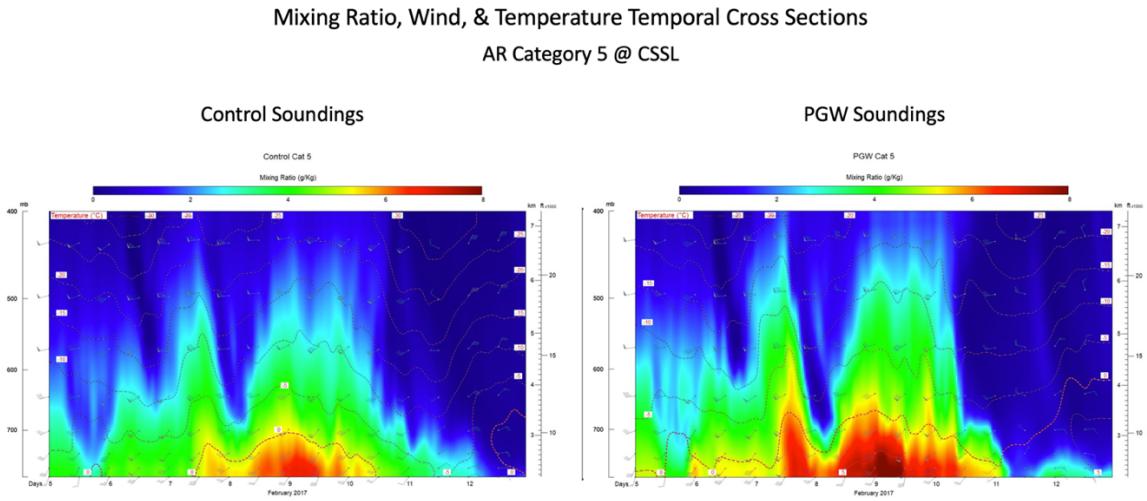

Figure 15. Comparison of Control and PGW temporal cross sections of vertical profiles of atmospheric variables for AR Cat 5. Plotted with RAOB software. Temperature is represented by isotherms in °C; winds are in knots (wind barbs); mixing ratio is depicted by color-filled contours.

Event-Maximum Altitude of the 0°C Isotherm			
AR Category	**Control (ft. MSL)**	**PGW (ft. MSL)**	**Change (PGW-Control) (ft.)**
Cat 5	10,337	11,130	793
Cat 4	10,127	12,144	2,017
Cat 3	5,604	8,774	3,170
Cat 2	10,402	13,525	3,123
Cat 1	7,764	9,265	1,501

Table 6. Table reporting the AR event-maximum altitude (MSL) of the 0°C isotherm, i.e., freezing level, for WRF Domain-4 Control and PGW simulations. Increases in the event-maximum altitude of the 0°C isotherm are reported with respect to the Control simulation.

PGW Precipitation

Broad-scale precipitation patterns were analyzed to contextualize the changes in precipitation found within the high-spatial resolution Domain-4. Previous studies have found that changes in PGW precipitation are heterogeneous both spatially and between individual AR events (Dominguez et al. 2018, Singh et al. 2018). The broad-scale precipitation patterns for AR Cat 5 and AR Cat 3 are shown in Figure 17, respectively. Precipitation plots for all ARs in the study are provided in Appendix 8.

The AR Cat 5 precipitation patterns for the Control and PGW simulations appear at first glance to be very similar. However, an analysis of the difference plot reveals that the Eastern Sierra received less precipitation in the PGW simulation. In the vicinity of the study site, locations on the windward side of the Sierra Nevada received more precipitation, while locations on the leeward side received less precipitation. More broadly, locations to the west of major geographic barriers received the largest increases in precipitation, although distance from the barrier appears to matter little, at least on the geographic scale represented by Domain-2. The impact of the PGW conditions on the

study area for this AR was that the Sierra Nevada near Donner Summit received less precipitation.

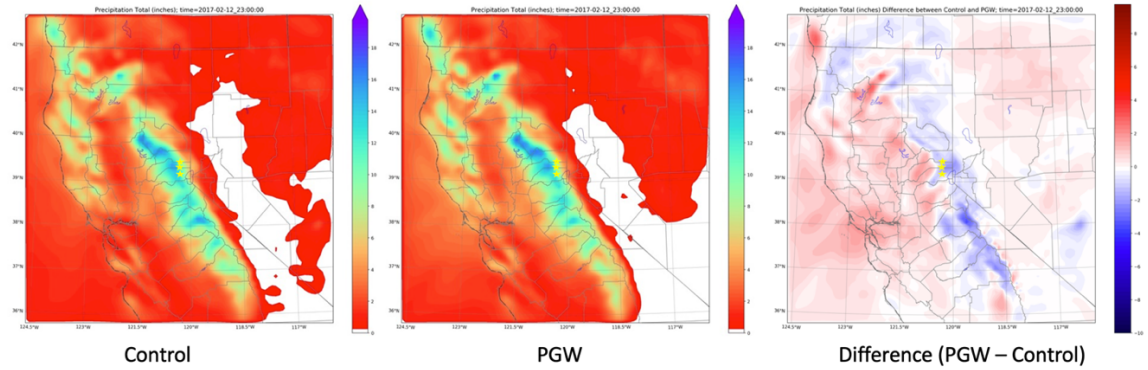

Figure 16. AR Cat 5 Total Precipitation Comparison (PGW – Control) for Domain 3. Precipitation is reported in inches.

In contrast, the precipitation pattern found for AR Cat 3 (Figure 17) features a pattern in which, between the California coast and the Eastern Sierra, areas to the north of a transect running from the Bay Area to approximately Pyramid Lake received less precipitation while areas to the south of this transect received more precipitation (i.e., the precipitation maxima shifted south). This resulted in the study area receiving more precipitation from this particular AR.

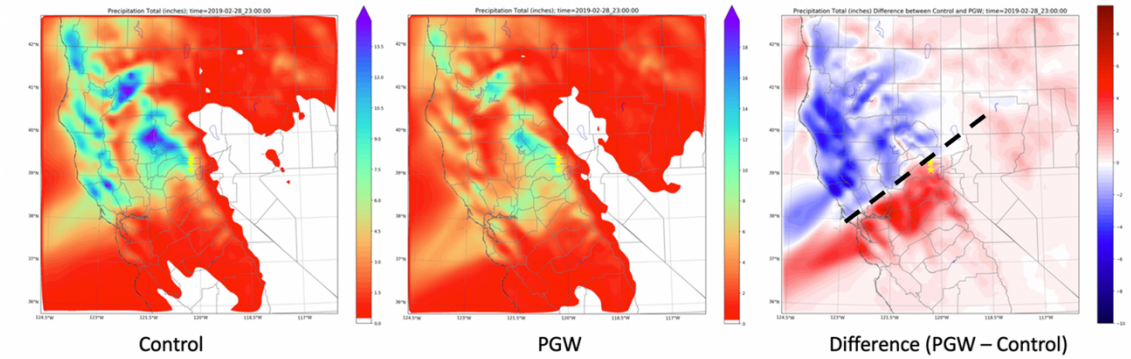

Figure 17. AR Cat 3 Total Precipitation Comparison (PGW – Control) for Domain 3. Precipitation is reported in inches.

Considering all ARs included in this study, the overall broadscale precipitation patterns for the PGW vs Control simulations varied widely. A unifying theory accounting for the differences in precipitation between ARs and between Control and PGW conditions was not readily identified. On a broad scale, precipitation did increase slightly for Domain-2 as a whole. However, this did not translate to an obvious signal in terms of an overall increase or decrease in precipitation for the study area, i.e., Donner Summit. This finding presents an interesting question: why does orographic precipitation fail to increase in proportion to increases in AR IVT and atmospheric moisture? This question, along with an analysis of precipitation in the highest-resolution domain, is analyzed below.

Domain 4 Precipitation (1-km Resolution)

Precipitation timeseries for the Control and PGW simulations for Domain-4 were analyzed to assess changes in precipitation timing, intensity, and total AR event precipitation. Figure 18 depicts the precipitation timeseries for AR Cat 5 and Cat 4. Timeseries for all Control and PGW AR simulations are provided in Appendix 8. Similar to the changes between the Control and PGW simulations in the broadscale precipitation pattern, the Domain-4 results are marked by both spatial and inter-AR heterogeneity. An analysis of the Superstation index revealed that some ARs presented as wetter while some presented as drier in the PGW simulations. Further, even within the same AR, different locations sometimes received either more or less precipitation depending on the AR.

For AR Cat 5, PGW precipitation decreased for two locations, Independence Lake and Squaw Valley GC, by 11.1% and 4.1%, respectively, while increasing for the CSSL by 4.2%. Overall, for AR Cat 5 the Superstation precipitation index decreased by 3.45% from Control to PGW. For AR Cat 4, PGW precipitation increased for all study sites, and the Superstation precipitation index increased by 11.7%. These spatial and AR-specific heterogeneous changes in event total precipitation were found for all ARs in this study. Previous PGW studies have noted similar findings in heterogeneous precipitation patterns both spatially and between individual ARs (Dominguez et al. 2018, Singh et al. 2018). These WRF results are in line with findings that precipitation variability increases in response to a warming climate on timescales ranging from single events to year-to-year (Pendergrass, et al., 2017). The precipitation patterns for ARs Cat 5 and 2 feature an increase in precipitation on the windward side of the Sierra. Such a pattern is hypothesized to occur due to the faster fall speeds of liquid vs frozen hydrometeors, resulting in decreased spillover precipitation for some warmer events, with windward (leeward) locations receiving more (less) precipitation. A similar pattern was not found, however, for AR Cat 1, which also featured a relatively warm near-surface temperature for the study area. This highlights the complexity of the processes that are affected by the PGW.

AR precipitation for the study area increased by an average of 1.31% in the PGW simulations. However, as shown in Table 7 individual ARs produced up to 15.3% more precipitation (AR Cat 3) and 18.9% less precipitation (AR Cat 2). This is in contrast to

the 31.3% increase in maximum AR IVT around the time of landfall discussed in the IVT section. Previous PGW research explains this apparent discrepancy by noting a decrease in precipitation efficiency, with increases in mixing ratio scaling faster than increases in cloud condensation, which in turn scale at a faster rate than precipitation (Dominguez et al. 2018, Singh et al. 2018).

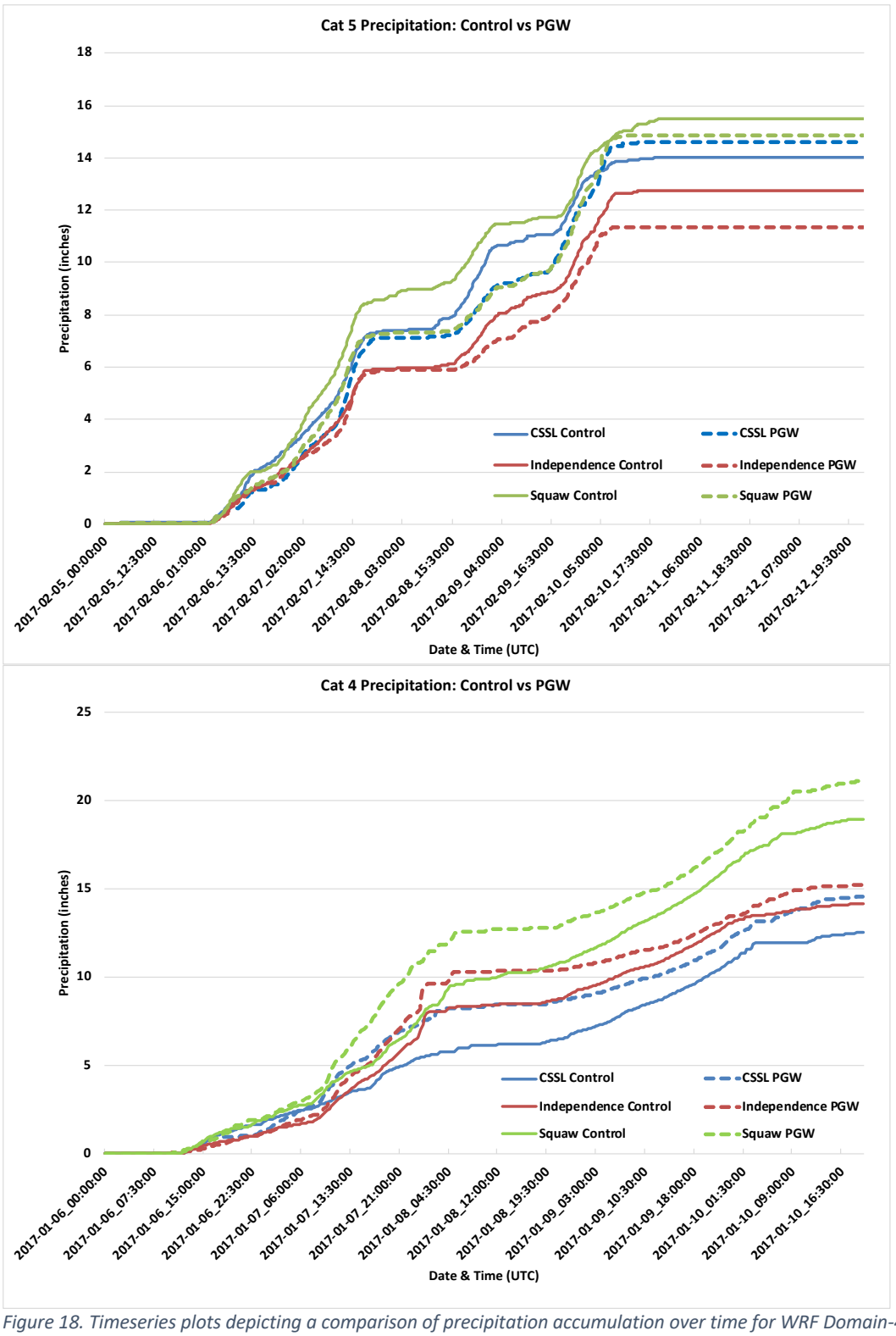

Figure 18. Timeseries plots depicting a comparison of precipitation accumulation over time for WRF Domain-4 Control and PGW simulations. Solid lines represent Control simulations; dashed lines represent PGW simulations. Colors as-defined by the legend.

Precipitation

AR Category	WRF Total Precip (Control)	WRF Total Precip (PGW)	% Difference
Category 5 (Feb. 5 – 12, 2017)	CSSL: 14.01 inches Independence Lake: 12.76 inches Squaw GC: 15.51 inches **Superstation: 14.09 inches**	CSSL: 14.60 inches Independence Lake: 11.34 inches Squaw GC: 14.88 inches **Superstation: 13.61 inches**	**-3.45%**
Category 4 (Jan. 6 – 11, 2017)	CSSL: 12.56 inches Independence Lake: 14.14 inches Squaw GC: 18.96 inches **Superstation: 15.22 inches**	CSSL: 14.58 inches Independence Lake: 15.21 inches Squaw GC: 21.20 inches **Superstation: 17.00 inches**	**11.67%**
Category 3 (Feb. 23 – 28, 2019)	CSSL: 8.79 inches Independence Lake: 8.55 inches Squaw GC: 8.74 inches **Superstation: 8.69 inches**	CSSL: 9.28 inches Independence Lake: 7.92 inches Squaw GC: 12.87 inches **Superstation: 10.02 inches**	**15.30%**
Category 2 (Jan. 31 – Feb. 3, 2019)	CSSL: 3.67 inches Independence Lake: 3.09 inches Squaw GC: 4.9 inches **Superstation: 3.89 inches**	CSSL: 3.50 inches Independence Lake: 2.45 inches Squaw GC: 3.51 inches **Superstation: 3.15 inches**	**-18.87%**
Category 1 (Jan. 31 – Feb. 5, 2017)	CSSL: 3.58 inches Independence Lake: 2.9 inches Squaw GC: 4.59 inches **Superstation: 3.69 inches**	CSSL: 4.12 inches Independence Lake: 2.73 inches Squaw GC: 4.43 inches **Superstation: 3.76 inches**	**1.90%**

Table 7. WRF Domain-4 Control vs PGW Precipitation for AR Cat 1 – 5. Percent difference is calculated with respect to Control simulations.

Temperature

Near-surface temperatures (2-m temperature) were analyzed for both Control and PGW AR simulations. While temperature deltas were applied to initial and boundary condition initialization data, the deltas were horizontally and vertically heterogeneous, representing RCP8.5 patterns of projected temperature changes. Thus, the model is not restricted to simply reproducing the applied temperature deltas, and simulated temperatures at the surface and aloft reflect the model's prediction of how the temperature fields for these ARs may change under RCP8.5 in the late 21st century. The temperature timeseries for AR Cat 5 is shown in Figure 19, and shows a comparison of 2m temperatures for the Control and PGW simulations. Event average temperature comparisons for all ARs in this study are shown in Appendix 9.

AR Cat 5 was the most significant event studied in terms of impacts, and the event average temperature, both in the SNOTEL observations and WRF simulations, was

within one degree Celsius of the melting point for the Superstation. The PGW simulation shows temperatures above 0°C for a longer duration during AR Cat 5, and further above 0°C compared to the Control simulation when temperatures were already above freezing in the Control simulation. Furthermore, PGW conditions pushed AR average temperatures above the freezing point for every AR studied, including AR Cat 3, in which the Control simulation kept temperatures below 0°C throughout the precipitation event for the Superstation.

The average increase in event-averaged 2-m temperatures for the PGW simulations was 2.14°C. This value is taken as the climate change response to the PGW forcing for the ARs in this study. While the WRF control simulations exhibited an average cold bias of -2.28°C for the ARs studied, the climate change response of +2.14°C is assumed to be free from this type of bias. This is because the processes underlying the model simulations are based on physical equations and parameterizations that are internally consistent between the simulations. Thus, changes in simulated temperature are significant, and are a fundamentally different measurement than the comparison of the WRF Control simulations to the SNOTEL observations. Changes in AR-average temperature between the Control and PGW simulations are the result of an internally consistent modeling framework based on the governing equations of the atmosphere, and are assumed to be capable of representing the changes in the dominant atmospheric properties (Dominguez 2018).

The projected increases in AR temperature between the Control and PGW simulations (Table 8) were applied to the SNOTEL observations in order to estimate the likely new AR average temperatures under RCP8.5 near the end of the 21st century. Table 9 lists the results of this analysis. One crucial implication of the increases in AR average temperature is that the AR-average temperature for each AR studied is warmer than 0°C under RCP8.5. AR Cat 5, which produced incredible impacts in and around the study area in February 2017, features an average overall temperature of 1.58°C, or 34.8°F under RCP8.5, up from 0.25°C as observed by the SNOTEL stations.

Lundquist et al. (2008) found that, in the California Sierra Nevada, near-surface air temperatures are a good predictor of precipitation type, and that at a temperature of 1.5°C, rain and snow are climatologically equally probable. Above 1.5°C, rain becomes increasingly more likely. For an AR of this magnitude, increasing temperatures and an increase in the proportion of rain to snow could spell disastrous consequences, both short-term and long-term. In the short-term, 12 inches of liquid precipitation falling as rain rather than snow would cause flooding concerns in its own right, but rain-on-snow presents additional flooding concerns. In the long-term, precipitation falling as rain paired with SWE loss due to rain-on-snow events could require area reservoirs to make large releases to accommodate the increased runoff. When precipitation falls as snow rather than rain, it is more likely to be retained as snowpack and released to area reservoirs in the spring and summer, replenishing water supplies when the water is needed most. Thus, the warmer climate may result in both short-term flooding and long-term water deficits.

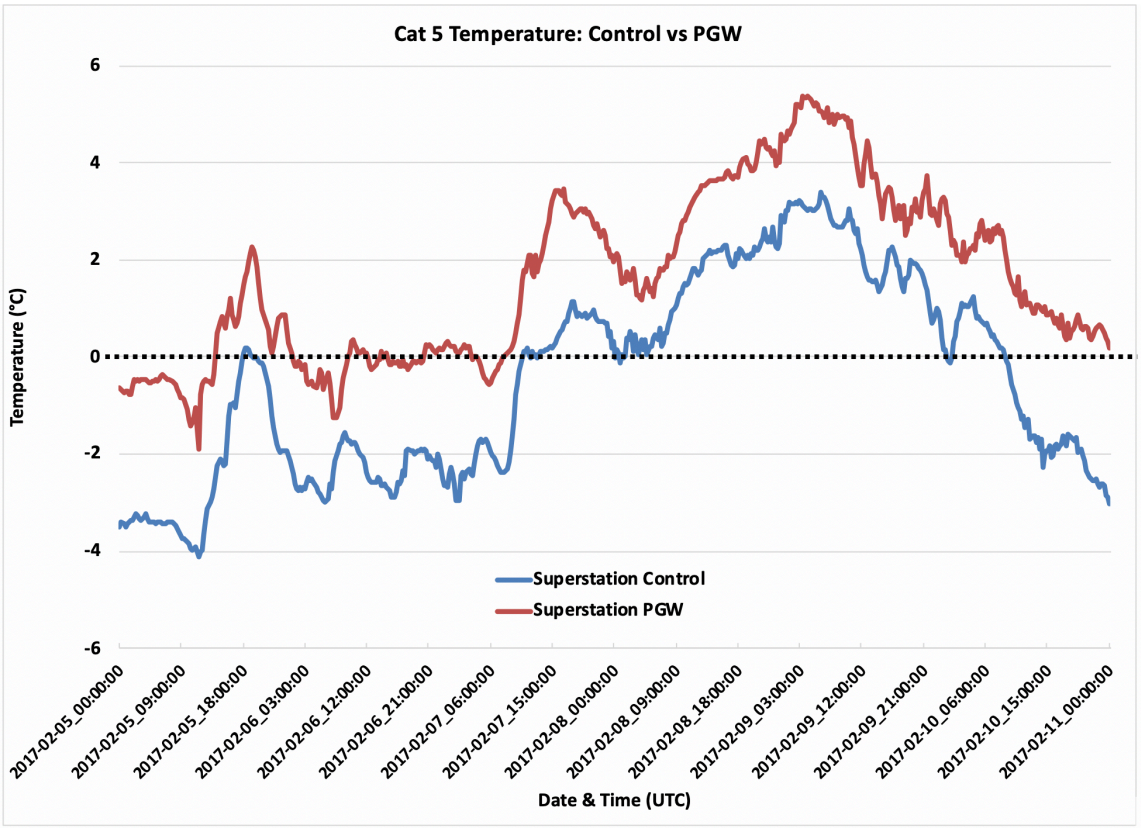

Figure 19. Comparison of WRF Domain-4 Control and PGW AR Cat 5 Temperature. The 0°C isotherm is indicated by the dotted black line.

Temperature

AR Category	WRF Control Average Temperature °C	WRF PGW Average Temperature °C	Difference
Category 5 (Feb. 5 – 12, 2017)	CSSL: -0.81 Independence Lake: -0.02 Squaw GC: -1.39 **Superstation: -0.74**	CSSL: 1.43 Independence Lake: 0.57 Squaw GC: -0.23 **Superstation: 0.59**	**+1.33 °C**
Category 4 (Jan. 6 – 11, 2017)	CSSL: -3.92 Independence Lake: -4.23 Squaw GC: -5.86 **Superstation: -4.67**	CSSL: -1.81 Independence Lake: -1.91 Squaw GC: -3.38 **Superstation: -2.37**	**+2.30 °C**
Category 3 (Feb. 23 – 28, 2019)	CSSL: -4.55 Independence Lake: -4.41 Squaw GC: -6.39 **Superstation: -5.11**	CSSL: -1.87 Independence Lake: -1.51 Squaw GC: -3.19 **Superstation: -2.19**	**+2.93 °C**
Category 2 (Jan. 31 – Feb. 3, 2019)	CSSL: -1.37 Independence Lake: -1.58 Squaw GC: -3.65 **Superstation: -2.20**	CSSL: 0.41 Independence Lake: 0.71 Squaw GC: -1.08 **Superstation: 0.01**	**+2.21 °C**
Category 1 (Jan. 31 – Feb. 5, 2017)	CSSL: -1.24 Independence Lake: -0.75 Squaw GC: -2.42 **Superstation: -1.47**	CSSL: 0.29 Independence Lake: 1.27 Squaw GC: -0.19 **Superstation: 0.46**	**+1.93 °C**

Average Temperature Increase = 2.14 °C (3.85 °F)

Table 8. WRF Domain-4 temperature for Control and PGW simulations for AR Cat 1-5. Temperature difference is with respect to Control simulations.

Atmospheric River	SNOTEL T	PGW–Control T	RCP8.5 New AR T
AR Cat 5	0.25°C	+ 1.33°C	**1.58°C**
AR Cat 4	-1.92°C	+ 2.30°C	**0.38°C**
AR Cat 3	-2.69°C	+ 2.93°C	**0.24°C**
AR Cat 2	0.76°C	+ 2.21°C	**2.97°C**
AR Cat 1	0.80°C	+ 1.93°C	**2.73°C**

Table 9. Table reporting PGW-adjusted SNOTEL Superstation AR event-average temperatures.

Changes in Freezing Levels

Changes in the average freezing level for the ARs were analyzed in order to determine the likely impacts of the temperature changes projected by RCP8.5. The plots below depict 2-m temperatures for Domain-4 with the 0°C isotherm indicated by the solid blue line. As the WRF Control simulations were shown to have a cold bias of nearly -2.4°C, the plots shown below are conservative estimates of the freezing level with respect to the SNOTEL observations. These plots are perhaps most effective at conveying the magnitude of the warming simulated in the PGW modeling rather than indicating the true projected freezing level. As discussed earlier, the magnitude of the projected changes is expected to be relatively unbiased compared to the difference between the SNOTEL observations and WRF simulations.

Figure 20 and Figure 21 depict the average 2m temperature and 0°C isotherm for AR Cat 5 and AR Cat 4, respectively. Plots for all ARs in the study are provided in Appendix 9. Between the Control and PGW simulations temperatures warm significantly, with the freezing level rising visibly, so that less of Domain-4 is below freezing and more precipitation will likely fall as liquid-phase rather than frozen-phase. These changes are

significant and consistent across ARs. In some cases, even in these relatively conservative estimates of the freezing level, the SNOTEL sites are either below the freezing level or are left alone on island-like areas of subfreezing temperatures, while average temperatures in surrounding areas warm to above freezing in terms of AR average temperature. This would certainly have significant implications on snow levels, snow storage, and potentially flooding impacts as a higher proportion of precipitation falls as rain and as snow melts when temperatures exceed the freezing point.

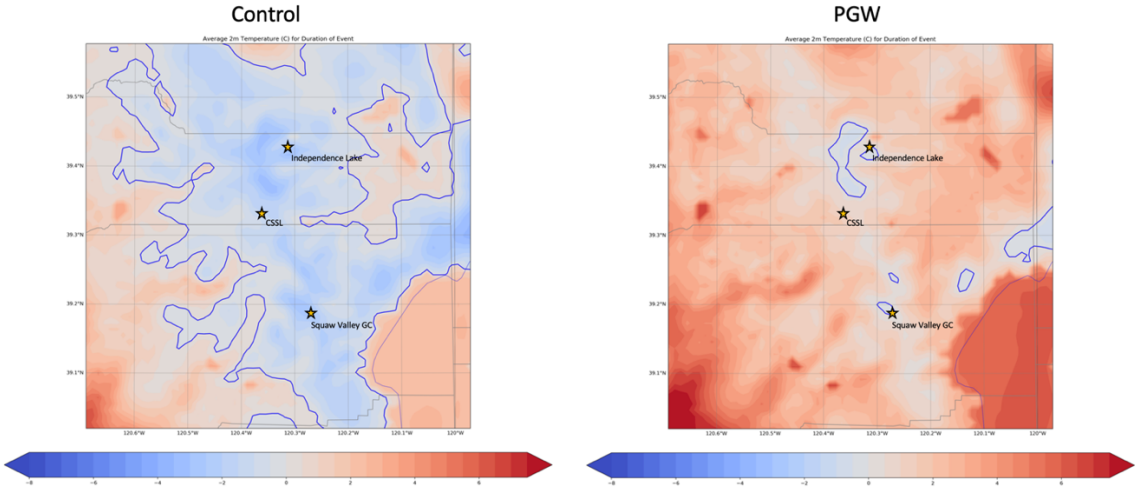

Figure 20. Comparison of WRF Domain-4 Control and PGW AR Cat 5 Surface Temperature and 0°C Isotherm.

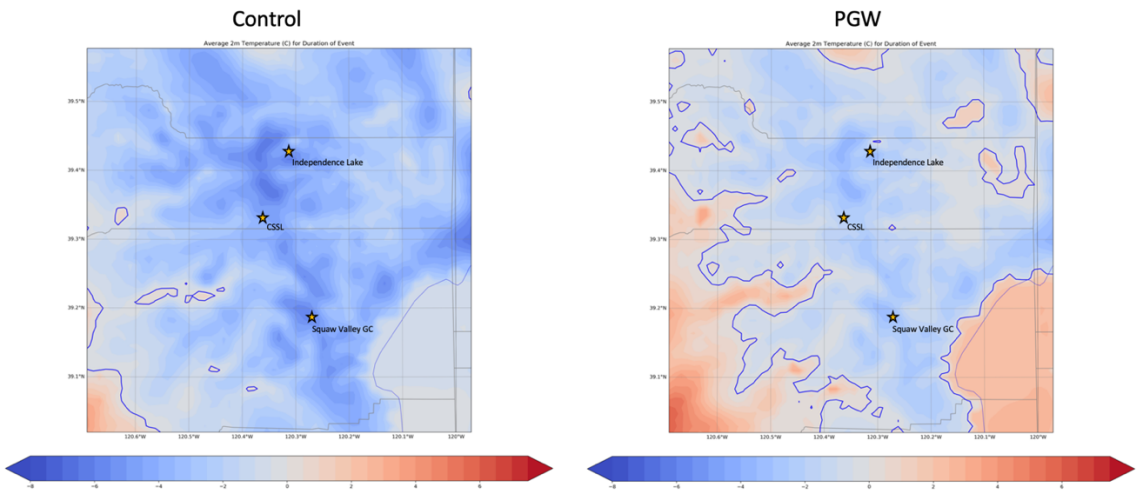

Figure 21. Comparison of WRF Domain-4 Control and PGW AR Cat 4 Surface Temperature and 0°C Isotherm.

Water Supply & Flooding Considerations

Under RCP8.5, future AR events are shown to be significantly warmer, while event-specific AR precipitation is shown to become significantly more variable (see Table 10). Warmer ARs are likely to increase both the number and significance of flood events (Payne et al. 2020). Warmer ARs that are also wetter will pose the significant two-fold challenge of increased flooding from both increased liquid precipitation and increased snowmelt, along with decreased snow storage, or SWE, resulting in less water in area reservoirs in the spring and early summer. These reservoirs may be unable to accommodate the additional runoff during the warm AR events, and may need to make flood-control releases, causing valuable water resources to be transported away from the Reno-Tahoe area to either Pyramid Lake or the Los Angeles District of Water and Power. The significance of the expected increase in AR average temperature paired with the range of precipitation outcomes will pose significant hydrological challenges. In this

study, the AR with the greatest increase in temperature also exhibited the greatest percentage increase in total precipitation (AR Cat 3). Table 10 summarizes this worst-case scenario along with data highlighting the magnitude of the changes and variability found in the PGW simulations approximating AR conditions near the end of the 21st century.

The implications of the PGW conditions representative of AR conditions under RCP8.5 are significant, including increased stress on hydrological resources, the local economy including the winter recreation sector, and life and safety concerns due to the increase in prevalence of wintertime flooding.

AR Cat 3: the Greatest Increases in Precipitation & Temperature	
Increase in Temperature	+2.93°C
Increase in Precipitation	+15.3%

Climate Change Signals: AR Cat 1-5 Under RCP8.5	
Maximum Temperature Increase	+2.93°C
Average Temperature Increase	+2.14°C
Maximum Precipitation % Increase	+15.3%
Maximum Precipitation % Decrease	-18.87%

Table 10. Summary statistics reporting WRF Domain-4 PGW temperature and precipitation changes with respect to Control simulations.

Summary and Conclusions

Atmospheric rivers provide a significant contribution of annual precipitation and SWE to the Sierra Nevada near Donner Summit, California, impacting commerce, hydrologic resources, and local industry. ARs can feature both beneficial and deleterious impacts depending on individual storm characteristics. While ARs often provide beneficial snowpack and have the capability to lift regions out of long-term drought, they also are responsible for nearly every major river flooding event in California history (Dettinger, 2011). AR characteristics are likely to change under a warming climate, which could impact the probability that a given AR will be primarily beneficial versus primarily hazardous. The motivation of this study was to better understand the potential changes in AR impacts caused by the warming climate.

ARs making landfall on the US West Coast have exhibited a warming trend since the 1980's according to a 2019 study by K. R. Gonzales. Individual atmospheric rivers and the overall AR climatology in terms of location, strength distribution, temperature, and precipitation intensity, are all expected to be impacted by changing global temperatures and circulations patterns due to warming temperatures and climate change. There have already been a number of studies undertaken on the impacts of climate change on the distribution, strength, and frequency of ARs, and much is already known, but more high-resolution modeling studies are needed. This is especially true in mountainous areas, as the complexities of the impacts of climate change on ARs in mountainous areas require specific and high-resolution modeling (Payne et al. 2020).

This study was designed to investigate how precipitation and temperature characteristics of future ARs (under RCP8.5 during the period 2071-2100) may impact the Donner Summit region of the Sierra Nevada. The potential effects of AR climate change on surface precipitation and temperature are investigated. Potential resultant impacts on flood potential, hydrologic resource management, and the local winter recreation industry are then discussed. This research utilized the PGW method, an approach in which temperature "deltas," both horizontal and vertical, are calculated by differencing gridded future and historic global climate model simulations, in this case for the DJF winter season under RCP8.5m (2071-2100 less 1971-2000). These deltas are then applied to the reanalysis data used to initialize WRF. While temperatures are altered in the initialization data to account for the future expected warming, relative humidity is maintained at the original values in order to account for the Clausius-Clapeyron relationship, in which the saturation mixing ratio of warmer air increases. This step is required because in its absence there would be essentially no saturation with respect to water in the initialization data after the climate change deltas are applied, which would deleteriously affect the modeling.

The WRF model was run for both Control and PGW scenarios. The CW3E West-WRF configuration was used for both Control and PGW scenarios. The only differences between the model runs were the temperature deltas that were applied following the PGW approach. The Control simulations were compared with IVT and synoptic wind and pressure fields from the ERA5 reanalysis data, PRISM precipitation, SNOTEL precipitation and temperature data for the study area, and with atmospheric sounding data

from the NWS Oakland radiosonde launches. While the moisture plume for AR Cat 2 was simulated further south than in the reanalysis data, the simulated precipitation for the study area was reasonable for a Category 2 AR. For all ARs studied, AR-related parameters exhibited a reasonable fit compared to the reanalysis data, and the major atmospheric processes were determined to have been reasonably simulated by the WRF Control.

Differences between the PGW and Control simulations were analyzed in order to quantify the effects of RCP8.5 climate conditions on the ARs. For the PGW simulations, maximum IVT was found to increase by approximately 31-32% above Control simulations. This increase in IVT is slightly higher than would be expected given the average temperature delta in the lower troposphere and the implications of the Clausius-Clapeyron relationship. The additional contribution to IVT likely comes from the increased depth of the AR moisture plumes given the RCP8.5 conditions, although further research is needed to further address this hypothesis. Model soundings for PGW and Control simulations at the CSSL were compared in order to study changes in the vertical distribution of atmospheric properties in the study area. Mixing ratio (i.e., atmospheric moisture) was noted to increase for all PGW simulations. This increase was observed both for event-maximum mixing ratio and for the vertical extent (i.e., depth) of the AR moisture.

The event-maximum altitude of the 0°C isotherm was found to increase by an average of 2,121 ft. for the ARs in this study. Precipitation changes between Control and

PGW simulations were heterogeneous in nature. Some ARs featured more precipitation for the study area while some were characterized by less precipitation in the PGW simulations. In all cases, precipitation scaled at a ratio less than Clausius-Clapeyron scaling of saturation vapor pressure with increasing temperature. This is hypothesized to occur due primarily to changes in precipitation efficiency, with saturation vapor pressure scaling at a faster rate than cloud condensation, which in turn scales at a faster rate than precipitation generation in ARs. In addition, variability in AR-to-AR precipitation is observed in global climate model simulations under RCP8.5 (Pendergrass et al. 2017).

In this study, individual AR precipitation increased (decreased) by up to 15.3% (18.9%), highlighting the finding of increased variability in precipitation in future climate scenarios. Near-surface temperatures (2-m temperatures) increased by an average of 2.14°C for PGW AR simulations. This average increase in temperature was applied to historic AR SNOTEL observations to calculate the PGW AR event average temperatures, resulting in event-average temperatures, as measured by the Superstation described in the Results & Discussion section, increasing to above 0°C for each AR in this study. This finding is significant, as surface temperatures are useful for predicting the type of precipitation that a given location will experience: above 0°C rain becomes increasingly more likely until at 1.5°C rain and snow are equally likely (Lundquist et al. 2008).

The AR that underwent the most warming in this study, AR Cat 3, also exhibited the largest percentage increase in precipitation. This highlights the troubling likelihood that, with increased variability in precipitation and with all storms undergoing some

degree of warming, inevitably some storms will increase in both strength and average temperature under RCP8.5 conditions. These storms will likely result in increased flooding, landslides, and significant SWE loss at elevations currently above the average rain-snow line. Plots of the terrain above and below the freezing level for the Control and PGW highlight this finding, as the Category 5 AR features above-freezing temperatures for almost the entire study area, including the Central Sierra Snow Lab. ARs with these characteristics are likely to pose a significant danger to life, safety, property (flooding, landslides, etc.) and hydrologic resource management.

Leung et al. 2004 predict an increase in the rain-to-snow ratio given warming ARs; however, the relationship is nuanced as the highest elevation locations may remain below freezing despite increases in temperature. This study corroborates those findings. However, the majority of most watersheds, and the majority of the region selected for this study, will likely see temperature increases that drive AR temperatures above 0°C, resulting in increased flooding in the short term and snow drought and hydrologic stress in the long term.

Warm snow drought conditions exist where the amount of total precipitation may be average, or even above average while the snow storage in the mountains, measured by SWE, is below normal (Harpold, Dettinger, & Rajagopal, 2017, Hatchett & McEvoy, 2018). Warm snow drought generates stress on hydrologic resources, as late spring and early summer snowmelt is decreased, sometimes failing to replenish area reservoirs. It is exacerbated by warming temperatures and rising snow lines in mountainous areas. As

temperatures continue to warm and snow lines continue their upward creep, snow coverage decreases at an even faster rate as less and less land surface area exists above the snow line. Left unchecked, the increasing elevation of the snow line will result in islands of snow coverage, marooning lower-elevation ski resorts and decreasing the amount of snow storage in the Sierra Nevada near Donner Summit. This scenario implies significant challenges for the local winter recreation industry and water resource managers due to the projected snow drought conditions, and for emergency managers as a result of significant warm precipitation events that may trigger flooding.

Additional research will be useful in understanding the likely changes in AR impacts as global average temperatures increase. A future method of studying ARs under climate change scenarios involves studying AR-specific temperatures in GCM-simulations. A limitation of the present study is that climate change deltas were calculated using wintertime mean temperatures for both recent (1971-2000) and future (2071-2100) time periods. The AR-specific method involves identifying ARs in future GCM model projections and identifying the associated temperature characteristics in order to calculate deltas specific to ARs rather than deltas that represent average winter temperatures. This could result in more accurate simulations of future ARs that further constrain the range of AR impacts under climate change scenarios.

References

Abatzoglou, J. T. (2011). Development of gridded surface meteorological data for ecological applications and modelling. International Journal of Climatology, 33(1), 121-131. doi:10.1002/joc.3413

Dettinger, M. (2011). Climate Change, Atmospheric Rivers, and Floods in California - A Multimodel Analysis of Storm Frequency and Magnitude Changes. JAWRA Journal of the American Water Resources Association, 47(3), 514–523. doi: 10.1111/j.1752-1688.2011.00546.x

Dominguez, F., Dall'erba, S., Huang, S., Avelino, A., Mehran, A., Hu, H., … Lettenmaier, D. (2018). Tracking an atmospheric river in a warmer climate: from water vapor to economic impacts. Earth System Dynamics, 9(1), 249–266. doi: 10.5194/esd-9-249-2018

Espinoza, V., Waliser, D. E., Guan, B., Lavers, D. A. & Ralph, F. M. Global analysis of climate change projection effects on atmospheric rivers. Geophys. Res. Lett. 45, 4299–4308 (2018). https://doi.org/10.1029/2017GL076968

Gonzales, K. R., Swain, D. L., Nardi, K. M., Barnes, E. A., & Diffenbaugh, N. S. (2019) Recent warming of landfalling atmospheric rivers along the west coast of the united states. https://opensky.ucar.edu/islandora/object/articles%3A22696

Guan, B., Molotch, N. P., Waliser, D. E., Fetzer, E. J., & Neiman, P. J. (2010). Extreme snowfall events linked to atmospheric rivers and surface air temperature via satellite measurements. Geophysical Research Letters, 37(20). doi: 10.1029/2010gl044696

Gutman et al. 2018: Changes in hurricanes from a 13-yr convection-permitting pseudo-global warming simulation. https://journals.ametsoc.org/doi/abs/10.1175/JCLI-D-17-0391.1

Harpold, A., Dettinger, M., & Rajagopal, S. (2017). Defining snow drought and why it matters. Eos. doi:10.1029/2017eo068775

Hatchett, B. J., & McEvoy, D. J. (2018). Exploring the origins of Snow drought in the Northern Sierra Nevada, California. Earth Interactions, 22(2), 1-13. doi:10.1175/ei-d-17-0027.1

Hecht, Chad W. & Cordeira, Jason M. 2017: Characterizing the influence of atmospheric river orientation and intensity on precipitation distributions over North Coastal California. https://agupubs.onlinelibrary.wiley.com/doi/full/10.1002/2017GL074179

Holtzman, N. M., Pavelsky, T. M., Cohen, J. S., Wrzesien, M. L., & Herman, J. D. (2020). Tailoring WRF and Noah-MP to improve Process representation of Sierra Nevada runoff: Diagnostic evaluation and applications. Journal of Advances in Modeling Earth Systems, 12(3). doi:10.1029/2019ms001832

IPCC Fifth Assessment Report, Chapter 12: Long-term Climate Change: Projections, Commitments and Irreversibility. https://www.ipcc.ch/site/assets/uploads/2018/02/WG1AR5_Chapter12_FINAL.pdf

Leung, L. R. et al. Mid-century ensemble regional climate change scenarios for the western United States. Clim. Change 62, 75–113 (2004).

Liu Y, Warner T, Wu W, Roux G, Cheng W, Liu Y, Chen F, Delle Monache L, Mahoney W, Swerdlin S (2009) A versatile WRF and MM5-based weather analysis and forecasting system for supporting wind energy prediction. In: 23rd WAF/19th NWP Conference, AMS, Omaha, NE. 1–5 June 2009, Paper 17B.3

Lundquist, J. D., Hughes, M., Henn, B., Gutmann, E. D., Livneh, B., Dozier, J., & Neiman, P. (2015). High-Elevation precipitation patterns: Using snow measurements to Assess daily Gridded datasets across the Sierra Nevada, California. Journal of Hydrometeorology, 16(4), 1773-1792. doi:10.1175/jhm-d-15-0019.1

Lundquist, J. D., Neiman, P. J., Martner, B., White, A. B., Gottas, D. J., & Ralph, F. M. (2008). Rain versus snow in the Sierra Nevada, California: Comparing doppler profiling radar and surface observations of melting level. Journal of Hydrometeorology, 9(2), 194-211. doi:10.1175/2007jhm853.1

Martin, A., Ralph, F. M., Demirdjian, R., DeHaan, L., Weihs, R., Helly, J., . . . Iacobellis, S. (2018). Evaluation of Atmospheric River predictions by the WRF model using aircraft and regional MESONET observations of orographic precipitation and its forcing. Journal of Hydrometeorology, 19(7), 1097-1113. doi:10.1175/jhm-d-17-0098.1

Payne, A.E., Demory, ME., Leung, L.R. et al. Responses and impacts of atmospheric rivers to climate change. Nat Rev Earth Environ 1, 143–157 (2020). https://doi.org/10.1038/s43017-020-0030-5

Pendergrass, A. G., Knutti, R., Lehner, F., Deser, C., & Sanderson, B. M. (2017). Precipitation variability increases in a warmer climate. Scientific Reports, 7(1). doi:10.1038/s41598-017-17966-y

PRISM Climate Group Precipitation Dataset, Oregon State University. http://prism.oregonstate.edu, Data acquired April 18, 2021.

Ralph, F. Martin et al. 2019 A Scale to Characterize the Strength and Impacts of Atmospheric Rivers. https://journals.ametsoc.org/doi/full/10.1175/BAMS-D-18-0023.1

Rasmussen et al. 2011: High-resolution coupled climate runoff simulations of seasonal snowfall over Colorado: A process study of current and warmer climate. https://journals.ametsoc.org/doi/full/10.1175/2010JCLI3985.1

Siler, N., & Roe, G. (2014). How will orographic precipitation respond to surface warming? An idealized thermodynamic perspective. Geophysical Research Letters, 41(7), 2606–2613. doi: 10.1002/2013gl059095

Singh, I., Dominguez, F., Demaria, E., & Walter, J. (2018). Extreme Landfalling Atmospheric River Events in Arizona: Possible Future Changes. Journal of Geophysical Research: Atmospheres. doi: 10.1029/2017jd027866

Warner, M. D., Mass, C. F., & Salathé, E. P. (2015). Changes in Winter Atmospheric Rivers along the North American West Coast in CMIP5 Climate Models. Journal of Hydrometeorology, 16(1), 118–128. doi: 10.1175/jhm-d-14-0080.1

Wrzesien, M. L., Durand, M. T., Pavelsky, T. M., Howat, I. M., Margulis, S. A., & Huning, L. S. (2017). Comparison of methods to estimate snow water equivalent at

the mountain Range scale: A case study of the California Sierra Nevada. Journal of Hydrometeorology, 18(4), 1101-1119. doi:10.1175/jhm-d-16-0246.1

Wyszogrodzki, A. A., Liu, Y., Jacobs, N., Childs, P., Zhang, Y., Roux, G., & Warner, T. T. (2013). Analysis of the surface temperature and wind forecast errors of the NCAR-AirDat operational Conus 4-KM WRF forecasting system. Meteorology and Atmospheric Physics, 122(3-4), 125-143. doi:10.1007/s00703-013-0281-5

Zhu, Y., & Newell, R. E. (1998). A Proposed Algorithm for Moisture Fluxes from Atmospheric Rivers. Monthly Weather Review, 126(3), 725–735. doi: 10.1175/1520-0493(1998)126<0725:apafmf>2.0.co;2

Appendices

Appendix 1 –Analysis of January SNOTEL Trends

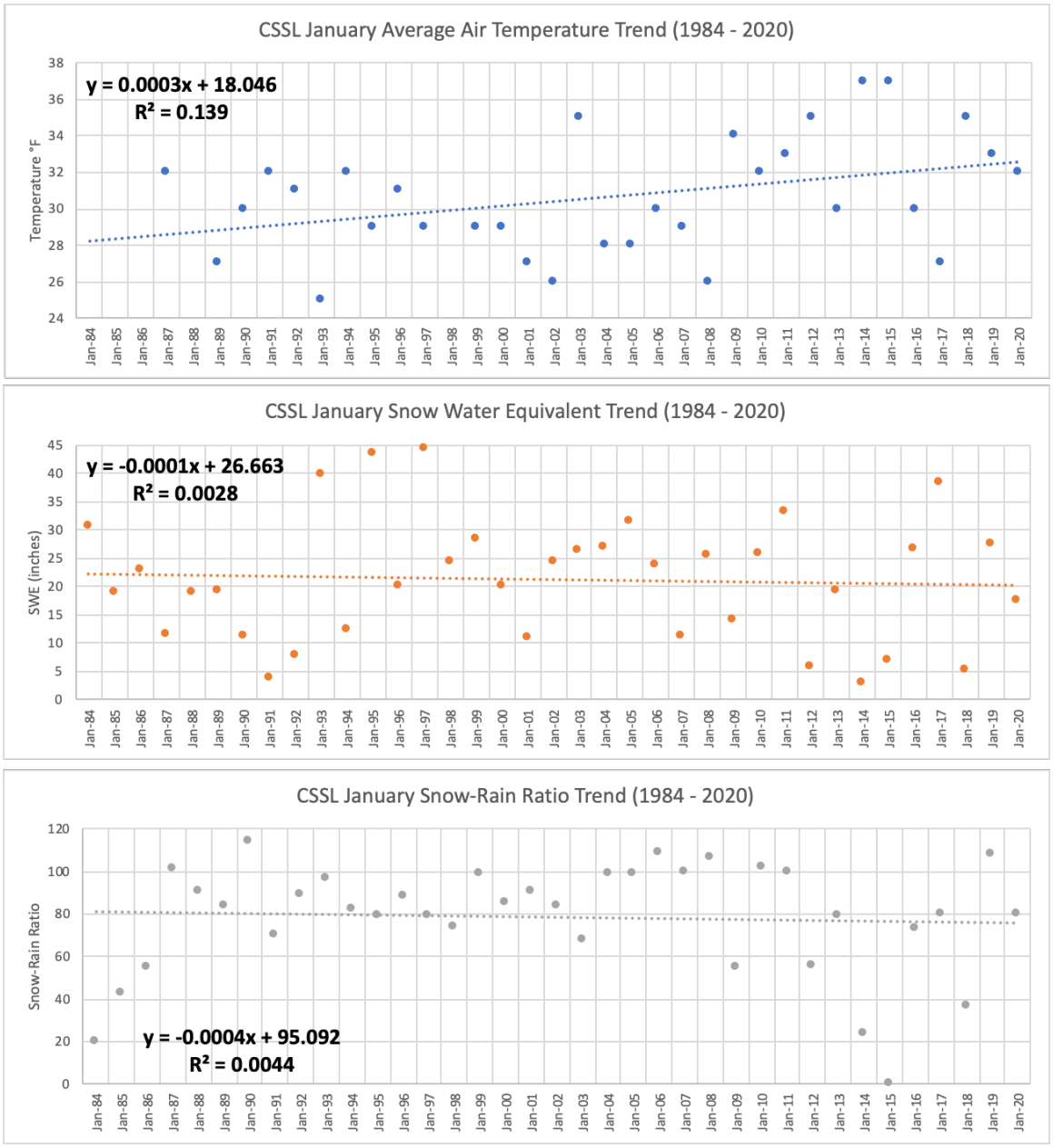

Appendix 1 Figure 1. Central Sierra Snow Lab SNOTEL observations and trends. Source: NRCS SNOTEL

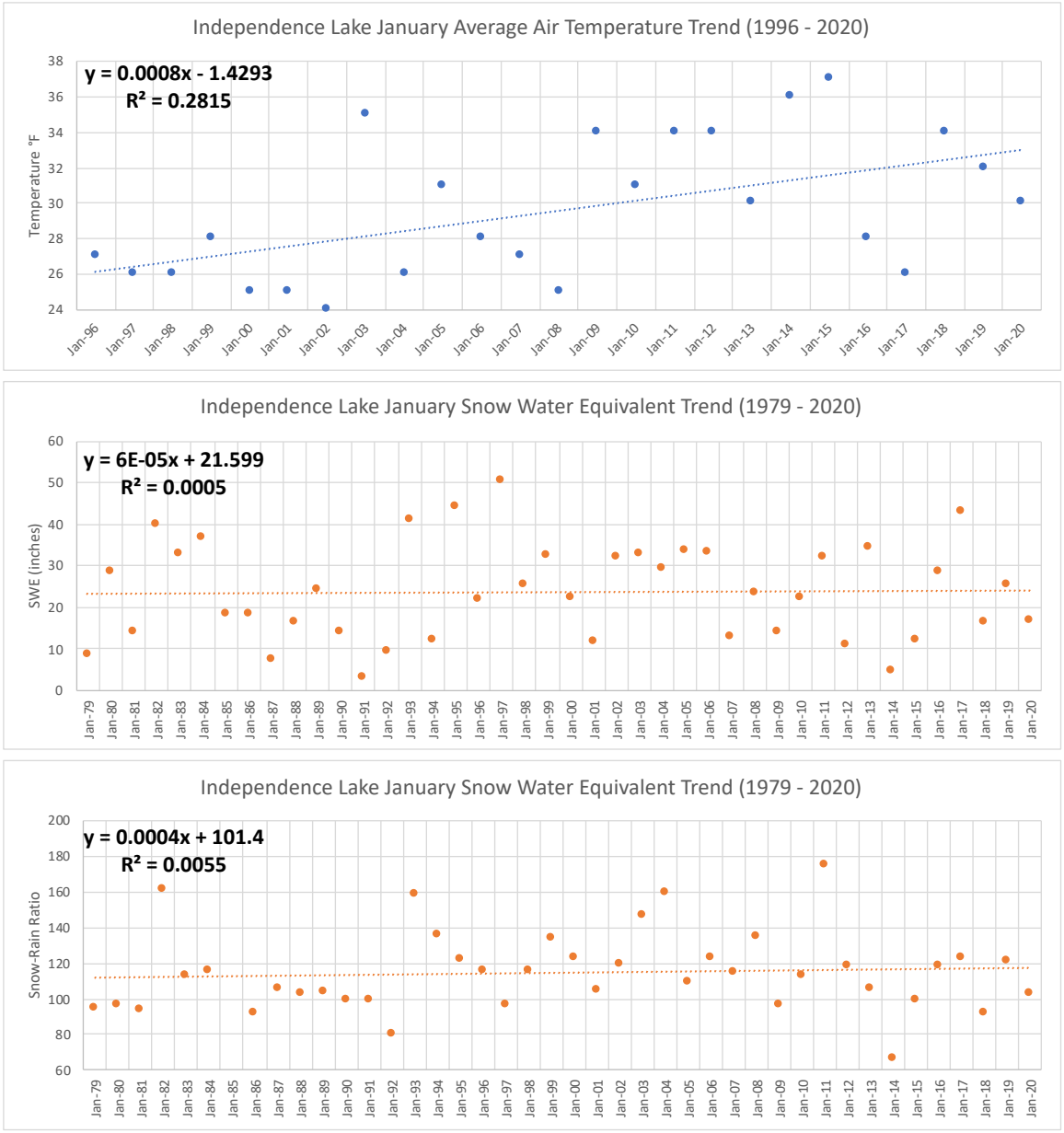

Appendix 1 Figure 2. Independence Lake SNOTEL observations and trends. Source: NRCS SNOTEL

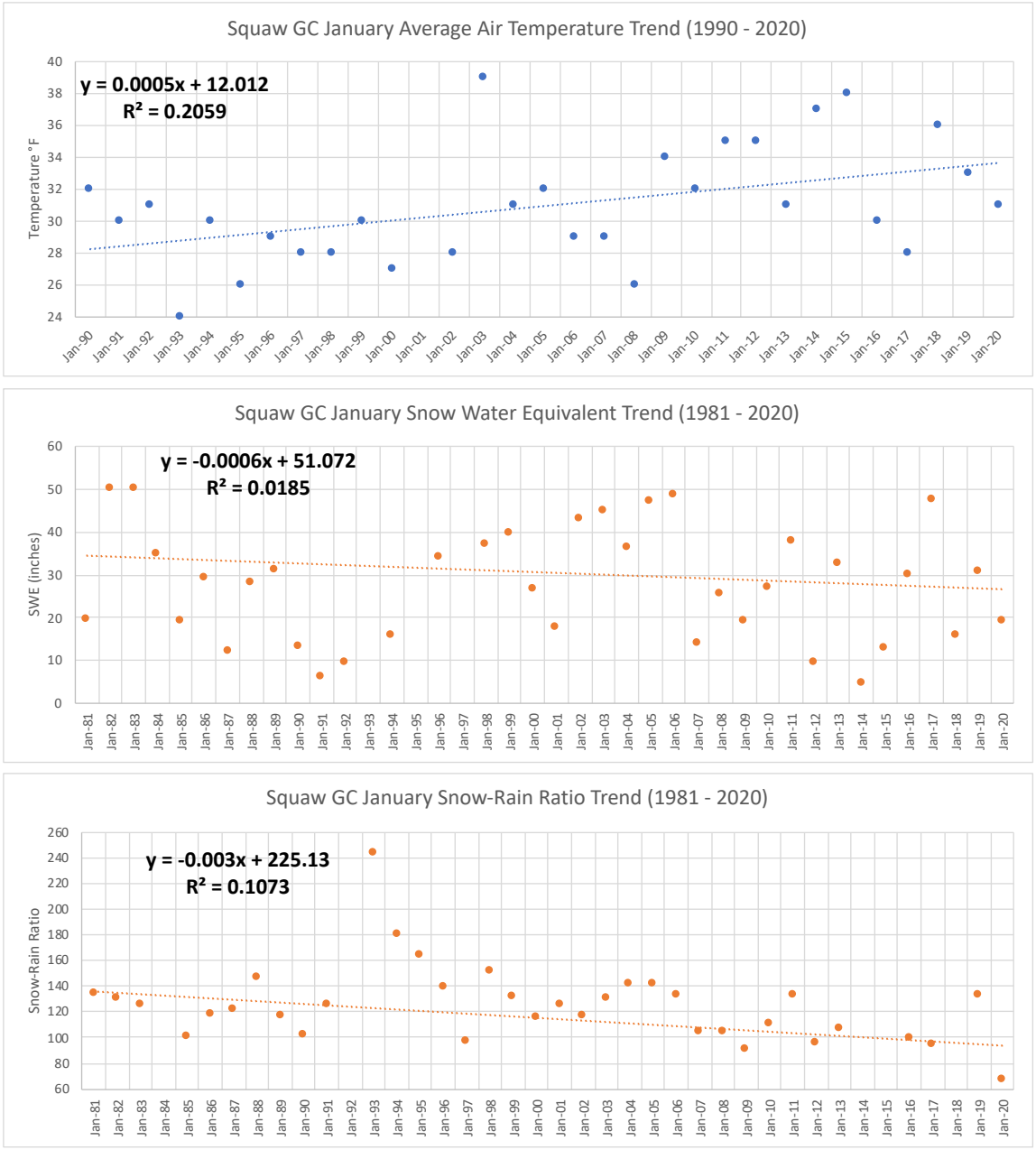

Appendix 1 Figure 3. Squaw GC SNOTEL observations and trends. Source: NRCS SNOTEL

Appendix 2 – CCSM4 2071-2100 – 1971-2000 Temperature Deltas

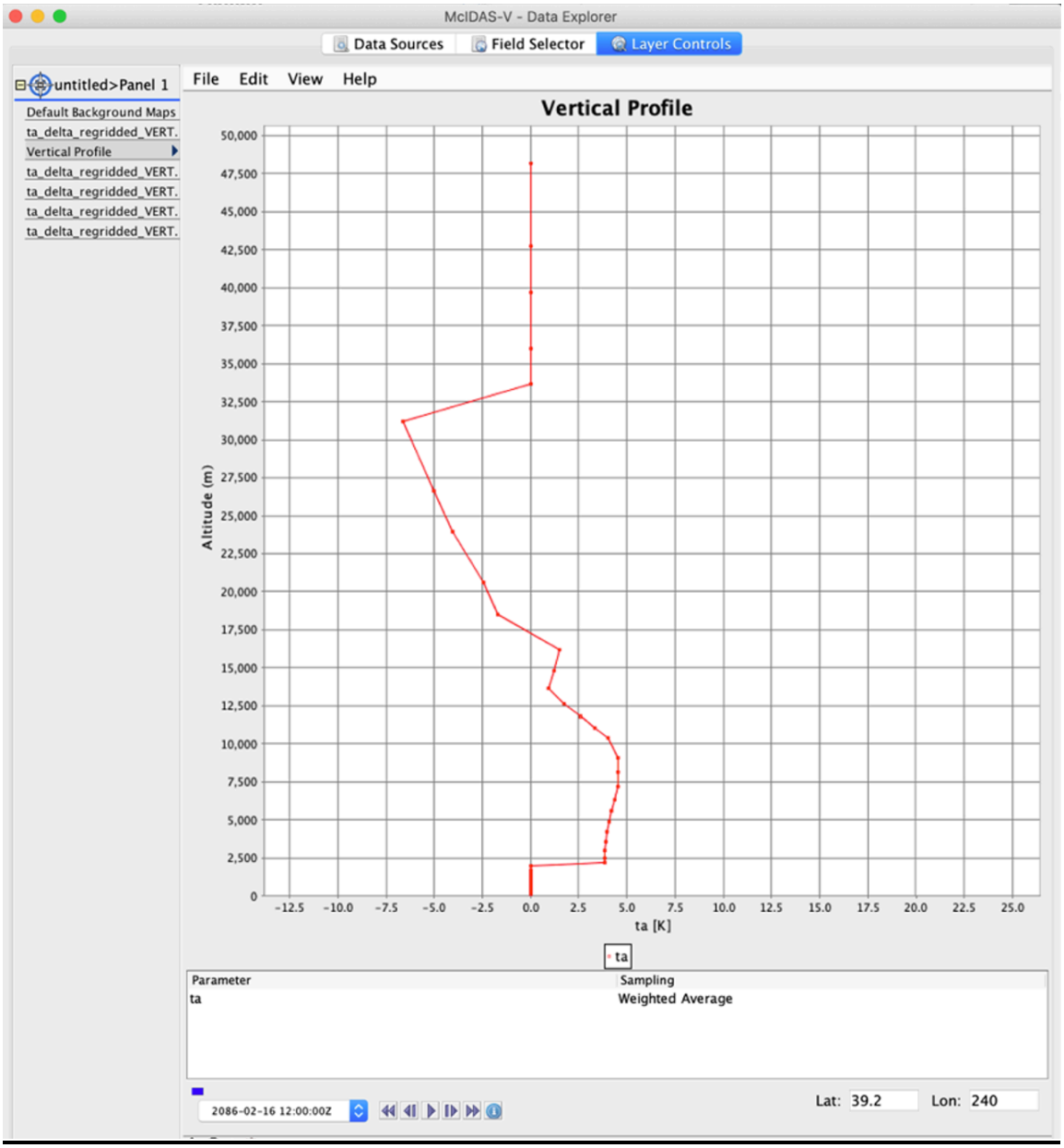

Appendix 2 Figure 1. Vertical profile of CCSM-4 RCP8.5 DJF air temperature deltas (2071-2100 less 1971-2000 temperatures) at the Central Sierra Snow Lab. Deltas are reported in Kelvins.

Delta Summary Statistics

RCP8.5 Ambient Temperature Delta Statistics (TA) (2071 – 2100)

Level	Minimum	Mean	Maximum
hPa	K	K	K
10	-13.847	-6.9712	-2.808
20	-10.661	-5.1913	-1.688
30	-8.8614	-4.2901	-1.2256
50	-7.0349	-3.3284	-0.44573
70	-5.9621	-2.0128	0.054548
100	-4.5569	0.58644	3.1568
125	-4.2682	0.81261	4.1559
150	-4.0361	1.0388	5.4894
175	-3.3182	1.522	5.7957
200	-2.6161	2.0052	6.1245
225	-1.2899	2.67	6.0477
250	0.018885	3.3348	6.0996
300	1.652	3.9666	5.9415
350	2.1068	4.0284	5.4167
400	2.4564	4.0902	5.2691
450	2.4803	3.9676	5.1447
500	2.4839	3.8451	5.035
550	1.8263	3.7502	5.1978
600	-0.94467	3.6394	6.0752
650	-0.94467	3.6166	6.0752
700	0	3.4112	8.303
750	0	3.4069	8.303
775	0	3.4048	8.303
800	-0.72085	3.1859	8.2497
825	-1.915	3.1838	9.4174
850	-3.1091	3.1817	10.585
875	-3.1091	3.2684	10.585
900	0	3.1228	14.612
925	-1.0828	3.2096	19.238
950	-1.0828	3.3919	19.238
975	-3.1734	2.5407	19.847
1000	-6.3237	2.723	26.403

RCP 8.5 Temperature Delta Statistics (2071-2100)

Parameter	Minimum (K)	Mean (K)	Maximum (K)
Ocean Surface Temperature (TOS)	-1.196	2.139	7.635
Surface Temperature (TS)	-0.410	4.959	21.785
2-Meter Temperature (TAS)	0.684	4.911	20.211

RCP8.5 Soil Temperature Delta Statistics (TSL) (2071-2100)

Depth/Level	Minimum	Mean	Maximum
m	K	K	K
.035	0.000	1.430	17.180
.175	0.000	1.445	16.814
0.640	-0.363	1.462	15.875
1.775	-0.156	1.513	13.688

Appendix 2 Figure 2. CCSM-4 Temperature Deltas (DJF, 2071-2100 less 1971-2000) that were applied to WRF boundary and lateral conditions for the PGW simulatinos described in this paper.

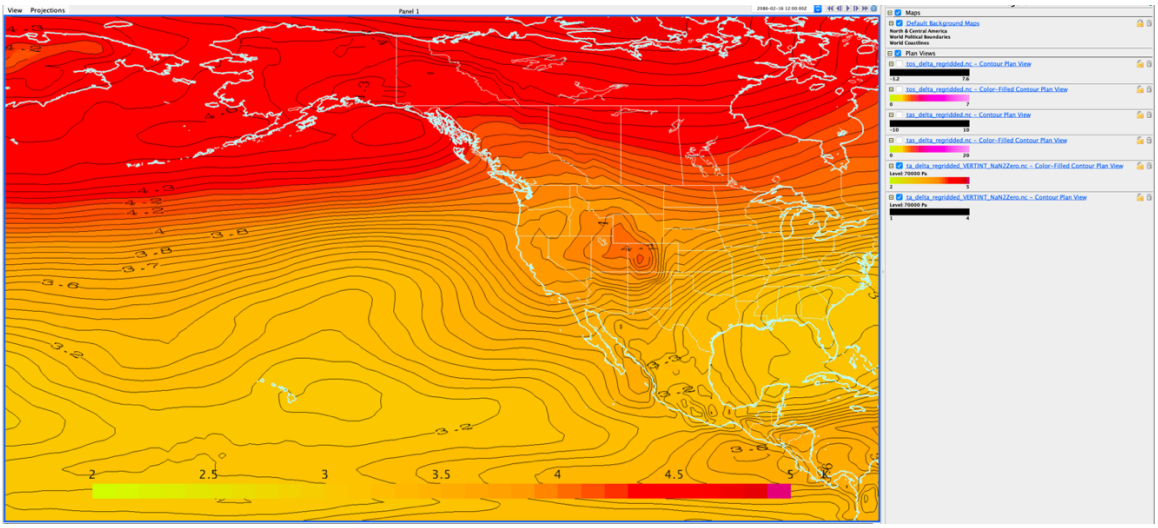

Appendix 2 Figure 3. Temperature deltas (as described above) for the 700 hPa pressure level reported in Kelvins.

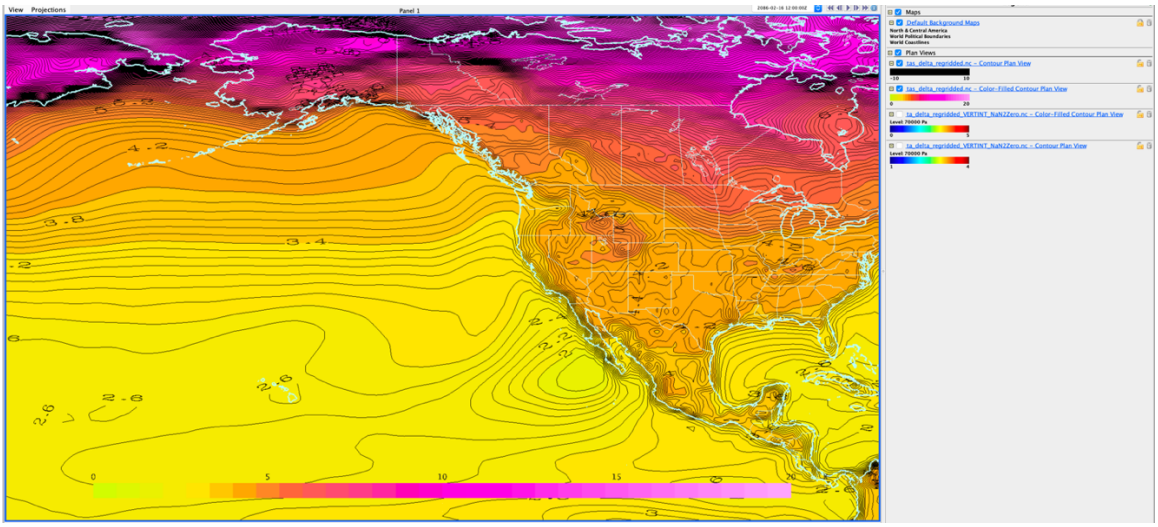

Appendix 2 Figure 4. Temperature deltas (as described above) for the near-surface (2-meter) level reported in Kelvins.

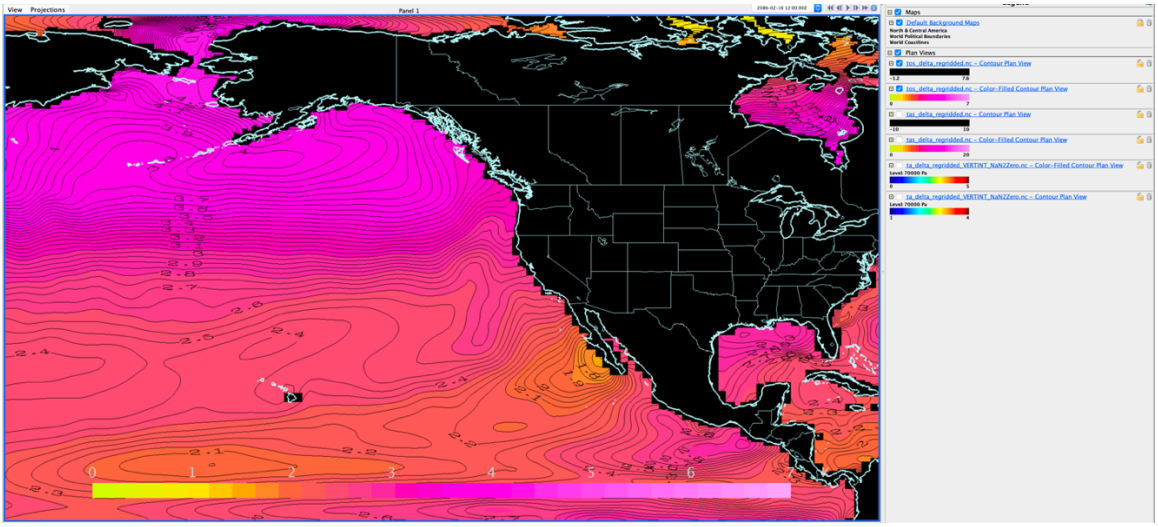

Appendix 2 Figure 5. Ocean surface temperature deltas (CCSM-4 DJF 2071-2100 less 1971-2000) reported in Kelvins.

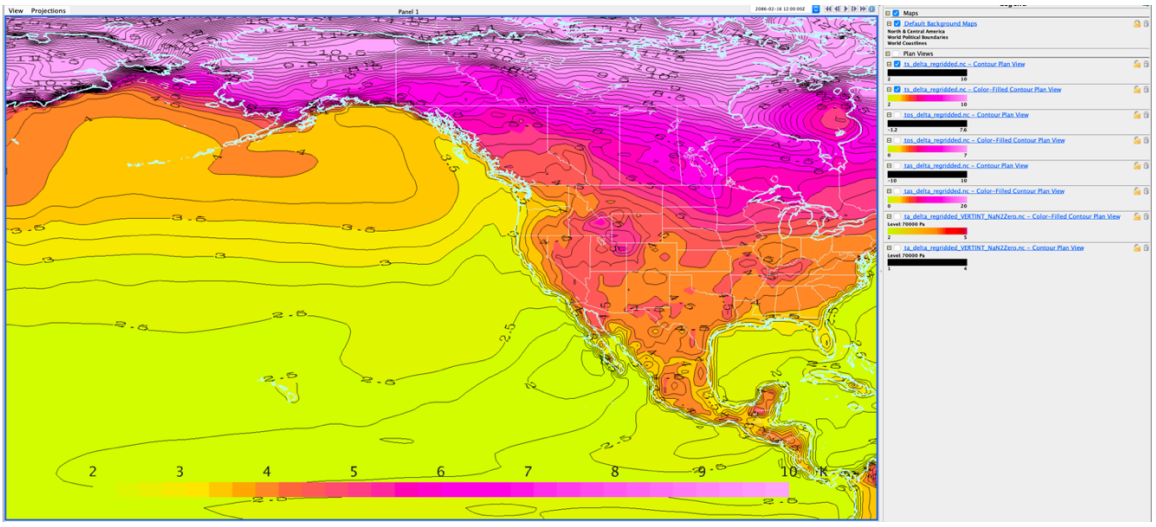

Appendix 2 Figure 6. Surface temperature deltas (CCSM-4 DJF 2071-2100 less 1971-2000) reported in Kelvins.

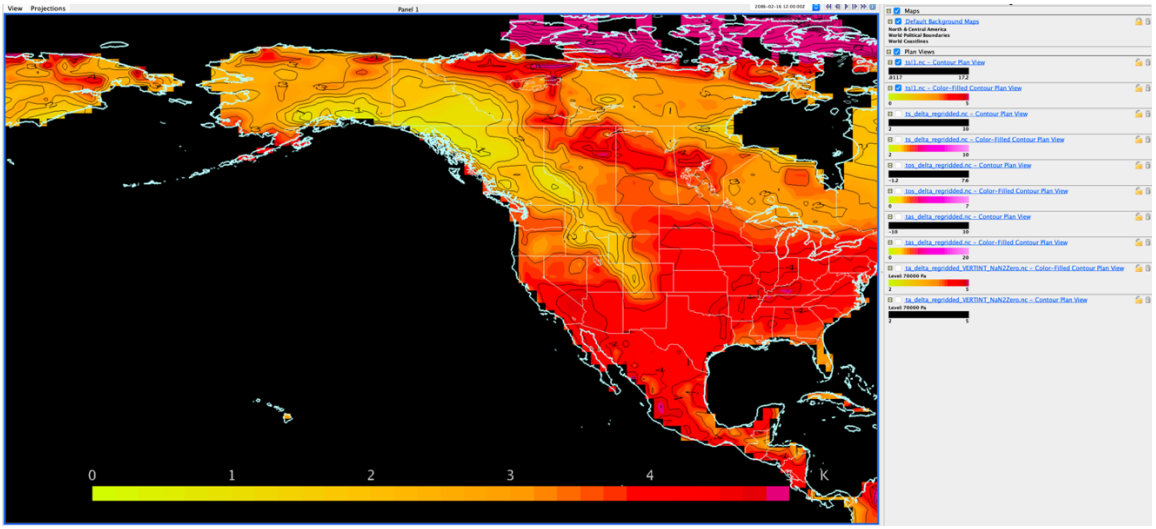

Appendix 2 Figure 7. Soil temperature (layer 1 average, 0-7cm depth) deltas (CCSM-4 DJF 2071-2100 less 1971-2000) reported in Kelvins.

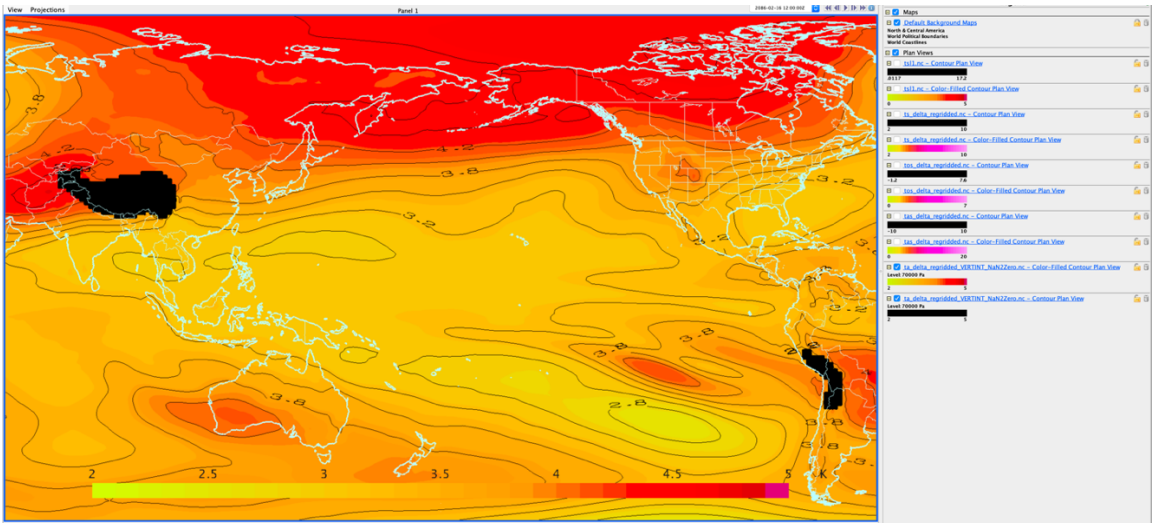

Appendix 2 Figure 8. Temperature deltas (as described above) for the 700 hPa pressure level reported in Kelvins.

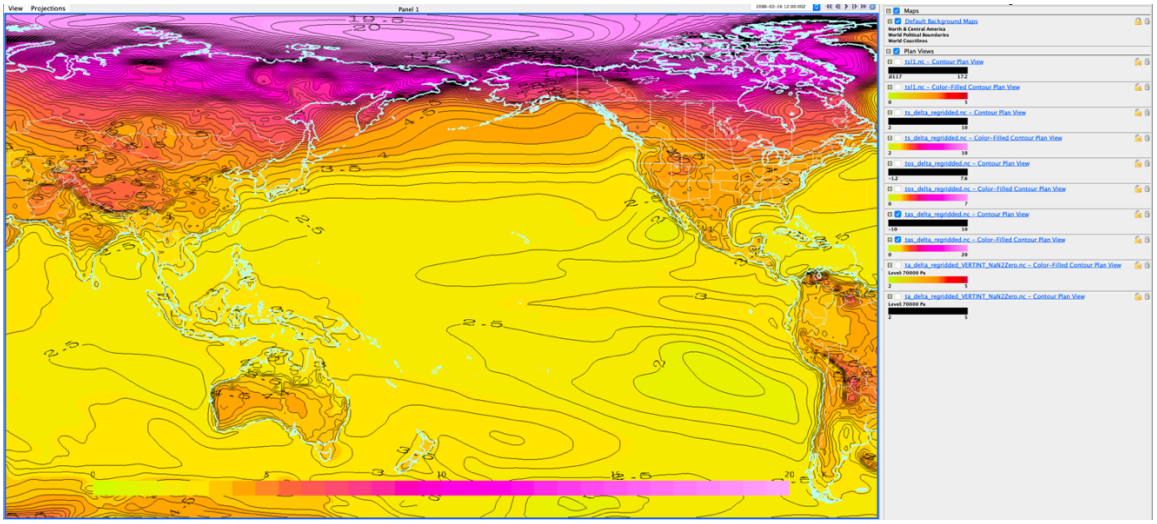

Appendix 2 Figure 9. Temperature deltas (as described above) for the near-surface (2-meter) level reported in Kelvins.

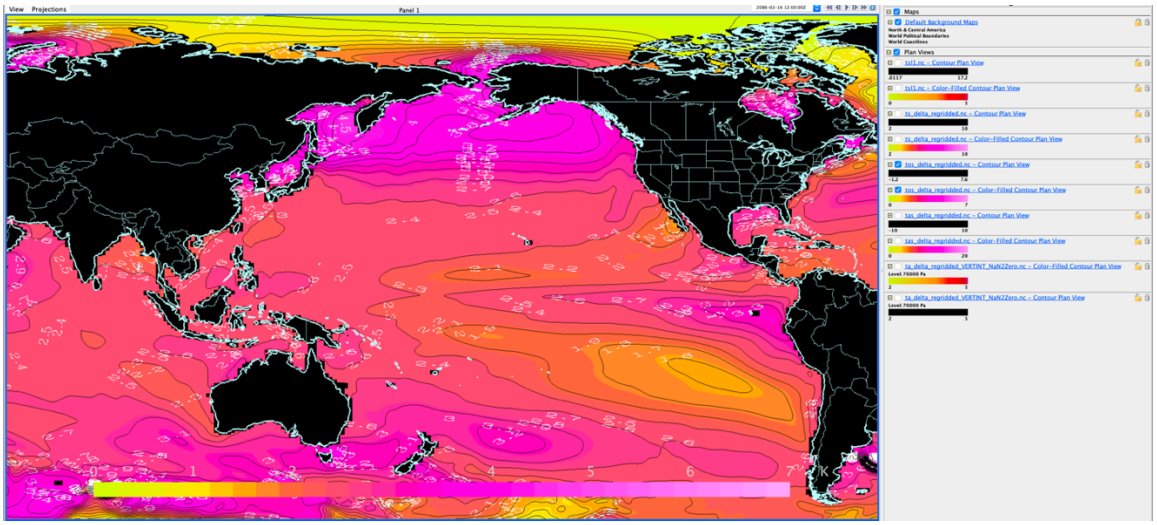

Appendix 2 Figure 10. Ocean surface temperature deltas (CCSM-4 DJF 2071-2100 less 1971-2000) reported in Kelvins.

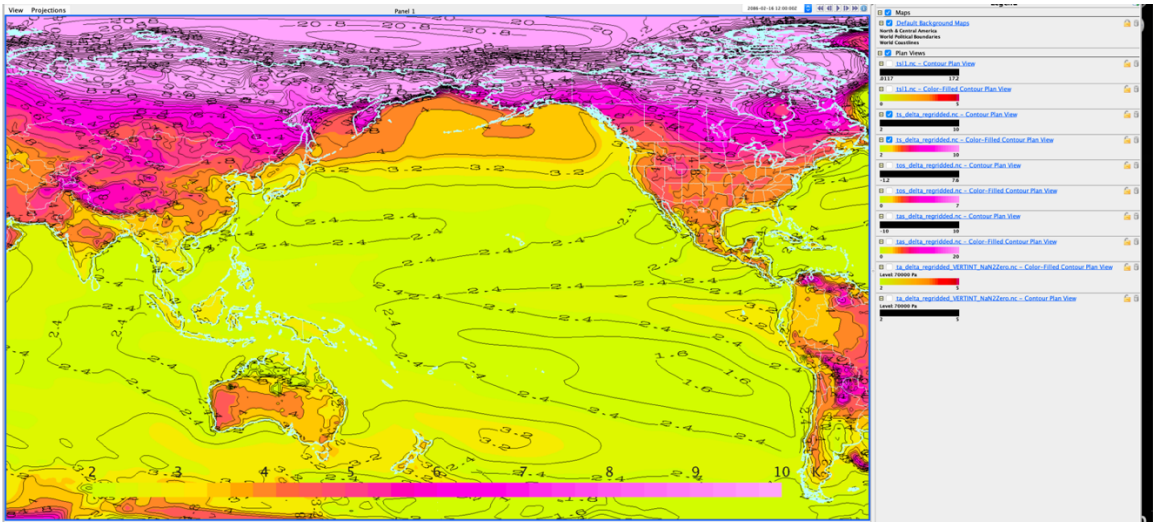

Appendix 2 Figure 11. Surface temperature deltas (CCSM-4 DJF 2071-2100 less 1971-2000) reported in Kelvins.

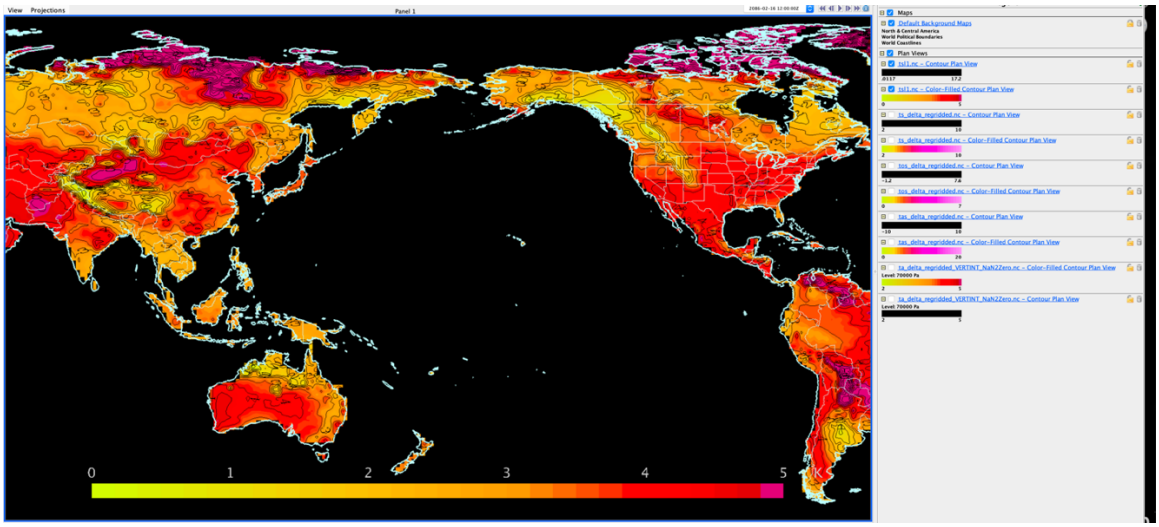

Appendix 2 Figure 12. Soil temperature (layer 1 average, 0-7cm depth) deltas (CCSM-4 DJF 2071-2100 less 1971-2000) reported in Kelvins.

Appendix 3 – IVT Comparison: ERA5 Reanalysis vs WRF Control

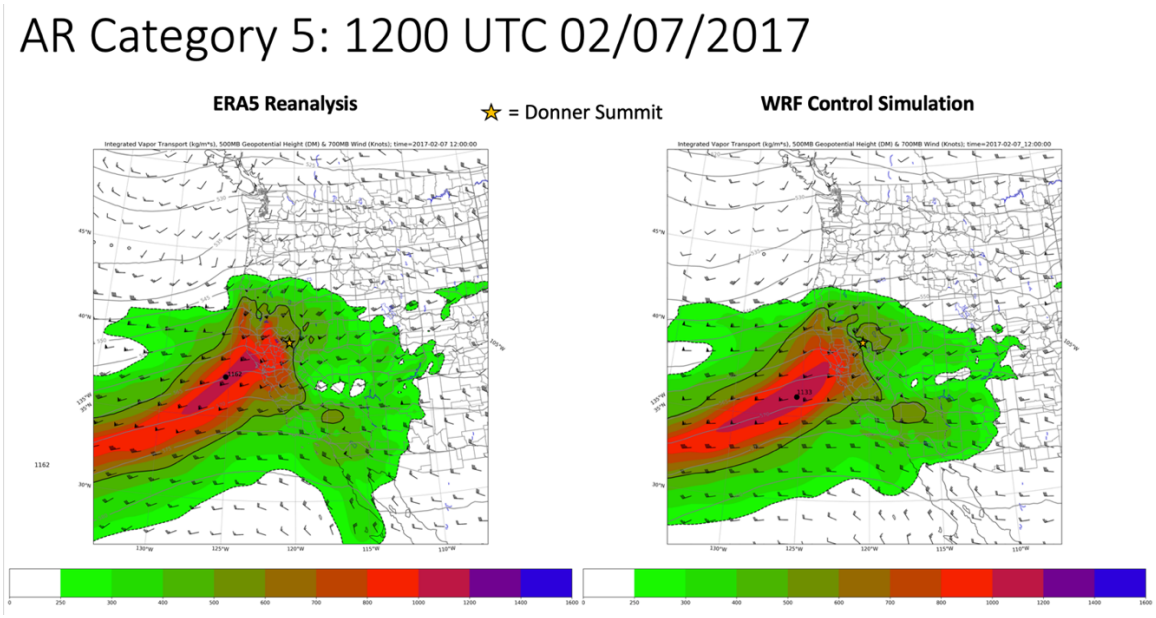

Appendix 3 Figure 1. ERA5 vs WRF Control IVT for AR Cat 5. The center of the study area (Donner Summit in the Sierra Nevada Mountains of California) is indicated by the gold star outlined in black.

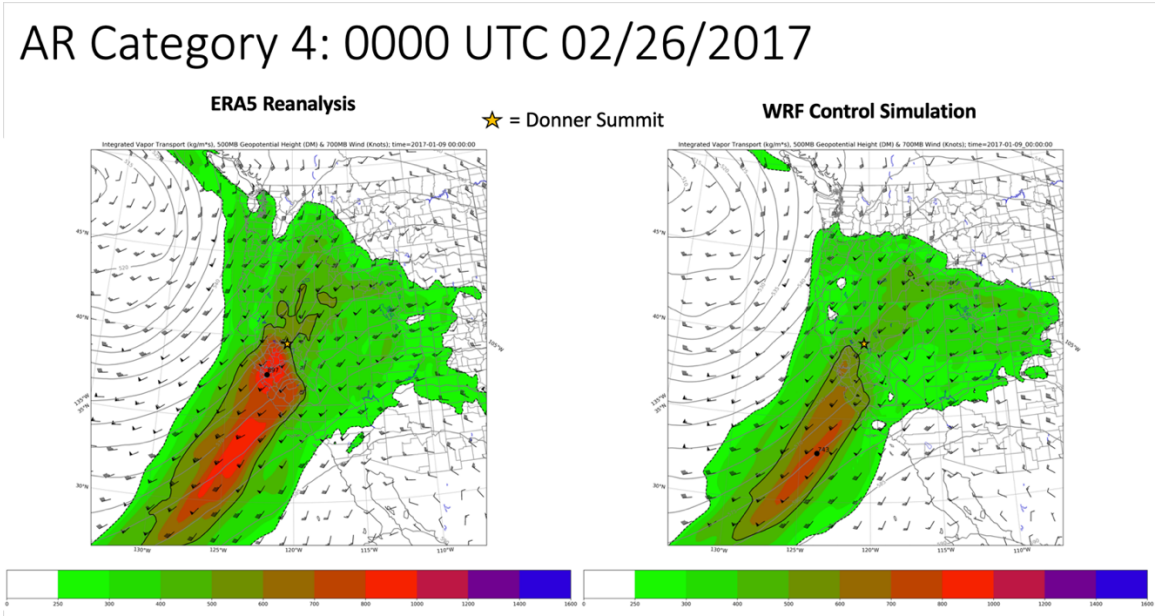

Appendix 3 Figure 2. ERA5 vs WRF Control IVT for AR Cat 4. The center of the study area (Donner Summit in the Sierra Nevada Mountains of California) is indicated by the gold star outlined in black.

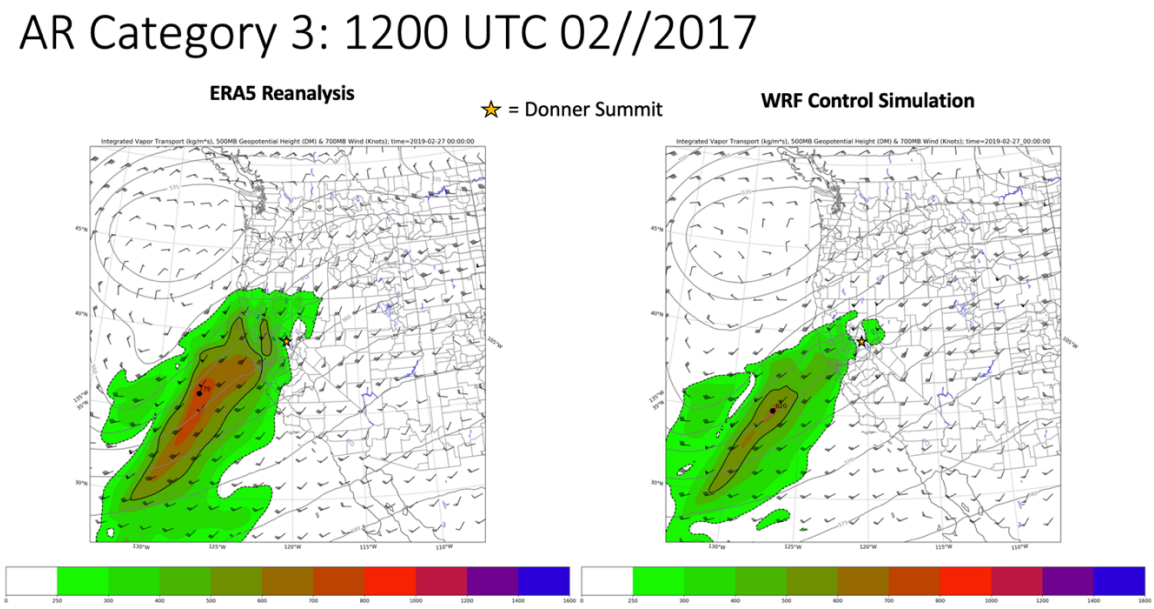

Appendix 3 Figure 3. ERA5 vs WRF Control IVT for AR Cat 3. The center of the study area (Donner Summit in the Sierra Nevada Mountains of California) is indicated by the gold star outlined in black.

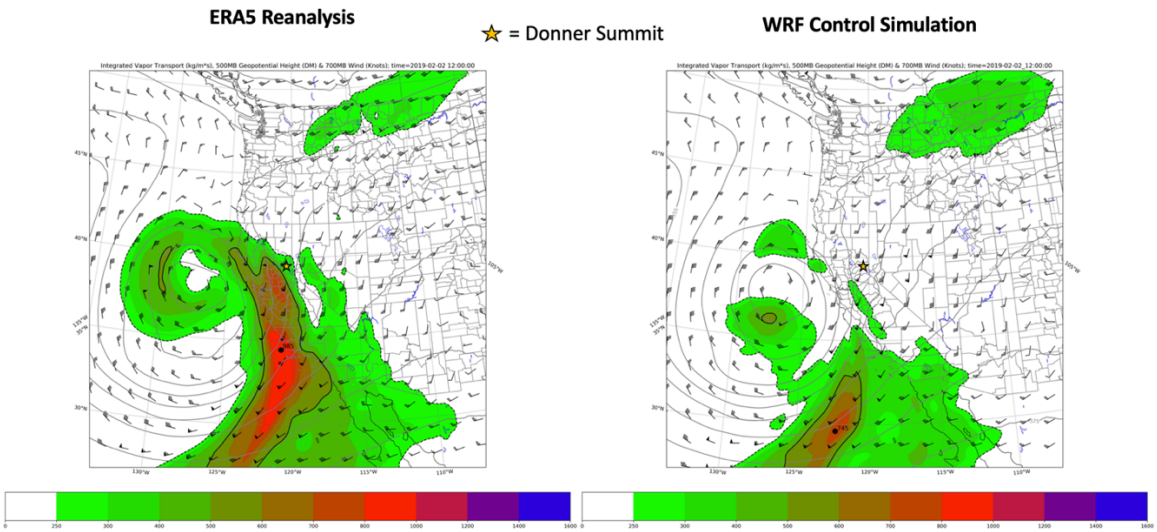

Appendix 3 Figure 4. ERA5 vs WRF Control IVT for AR Cat 2. The center of the study area (Donner Summit in the Sierra Nevada Mountains of California) is indicated by the gold star outlined in black.

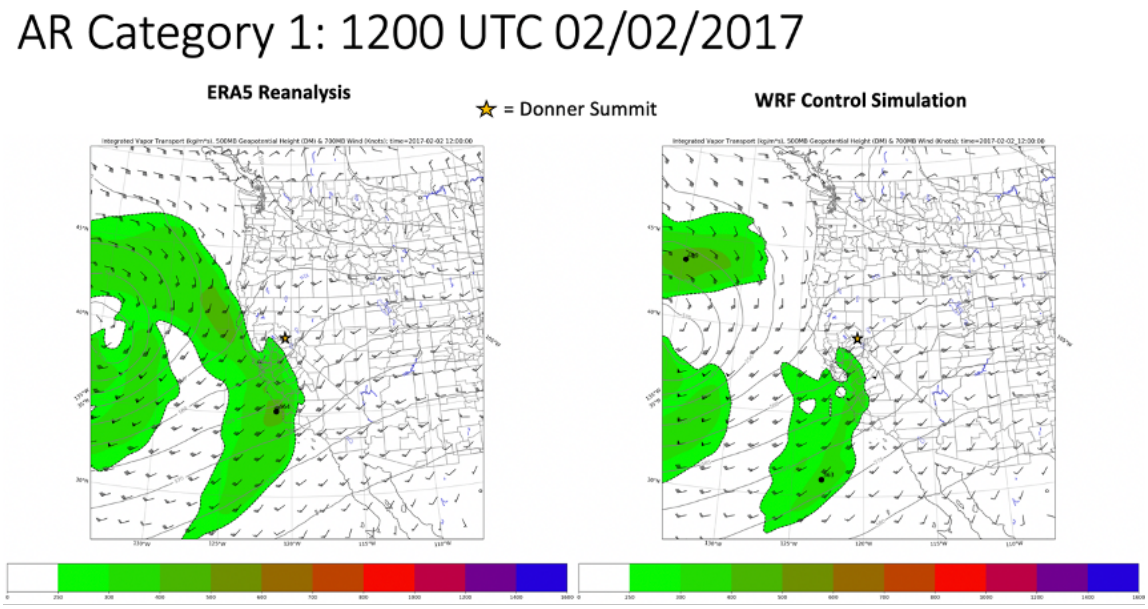

Appendix 3 Figure 5. ERA5 vs WRF Control IVT for AR Cat 1. The center of the study area (Donner Summit in the Sierra Nevada Mountains of California) is indicated by the gold star outlined in black.

Appendix 4 – Precipitation Comparison: PRISM vs WRF Control

AR CAT 5

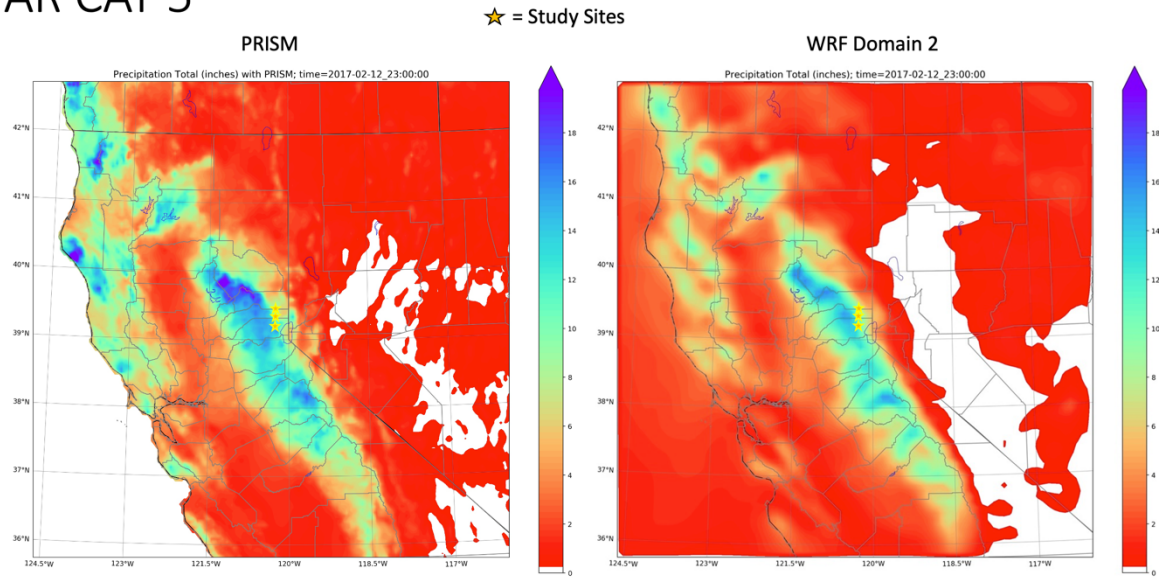

Appendix 4 Figure 1. Comparison between WRF-Control Domain-2 precipitation and PRISM precipitation for AR Cat 5.

AR CAT 4

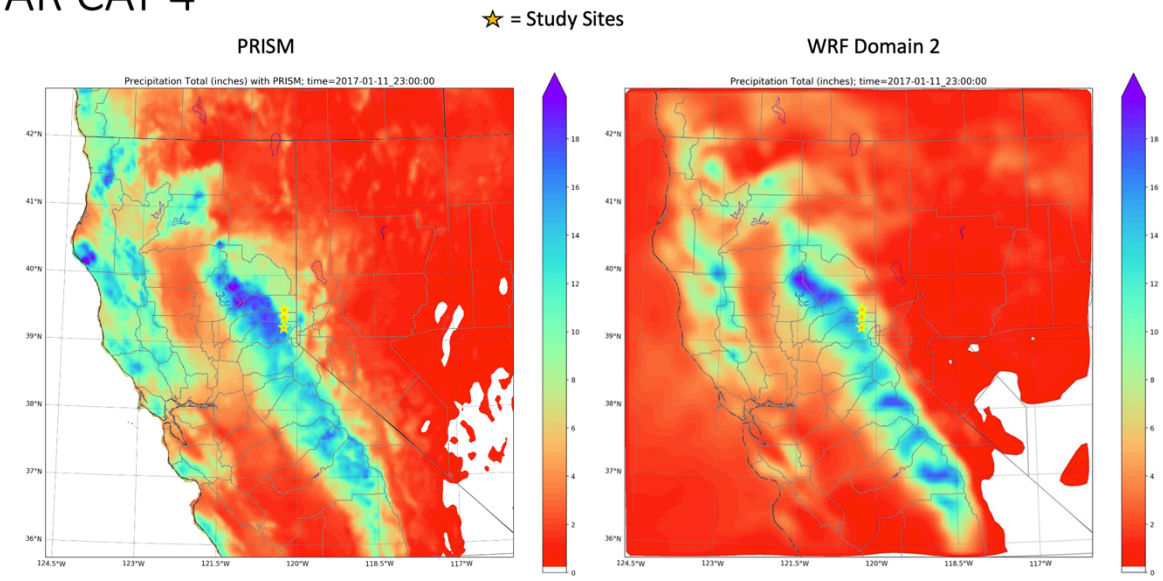

Appendix 4 Figure 2. Comparison between WRF-Control Domain-2 precipitation and PRISM precipitation for AR Cat 4.

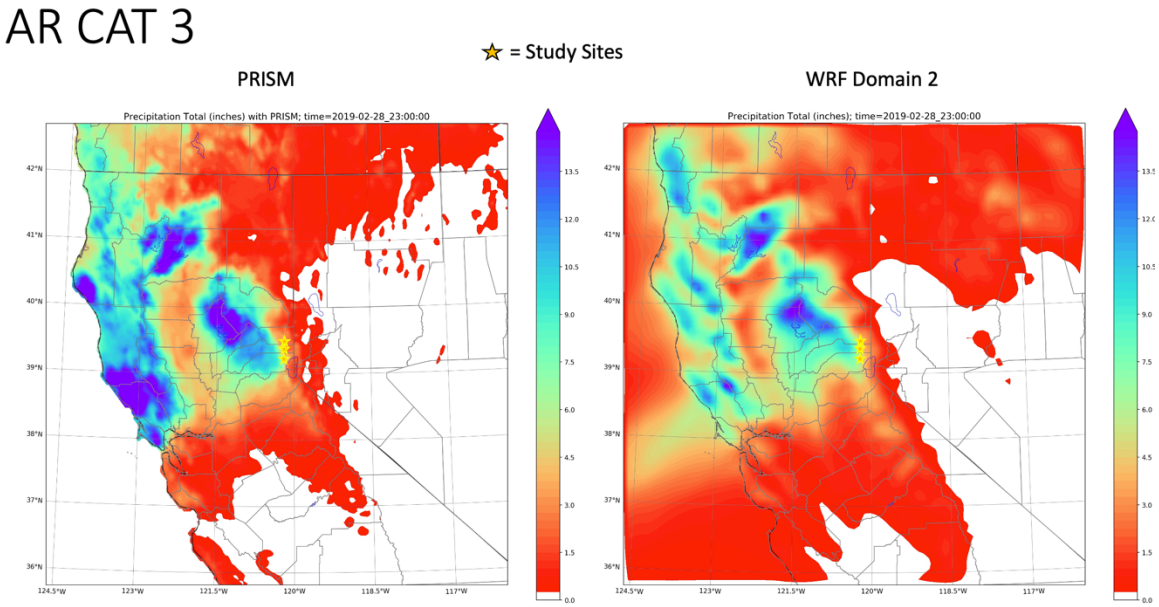

Appendix 4 Figure 3. Comparison between WRF-Control Domain-2 precipitation and PRISM precipitation for AR Cat 3.

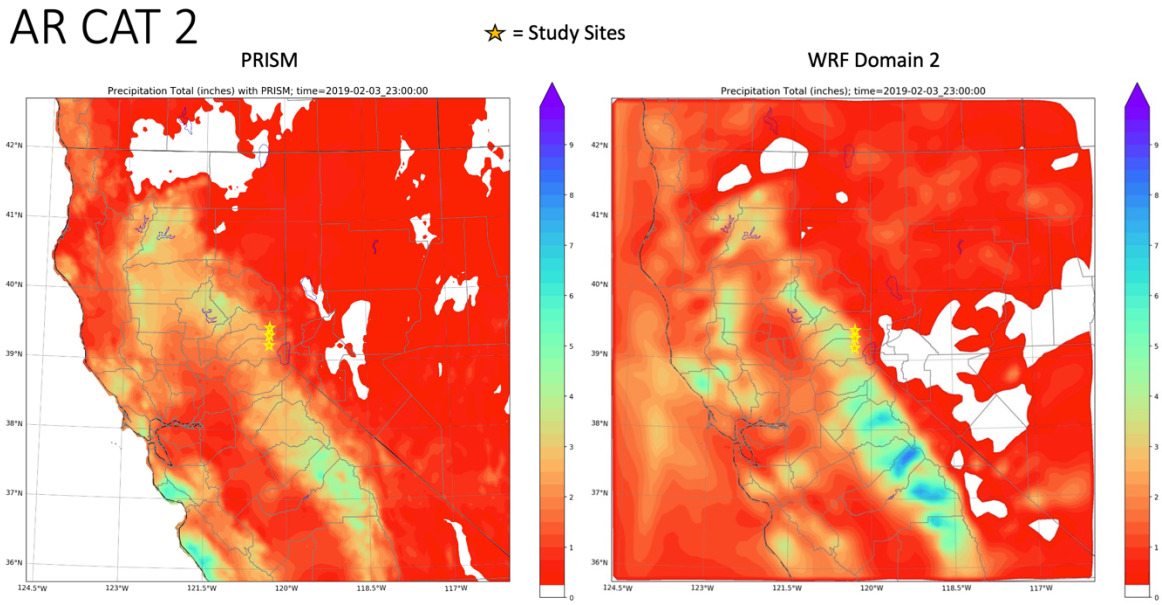

Appendix 4 Figure 4. Comparison between WRF-Control Domain-2 precipitation and PRISM precipitation for AR Cat 2.

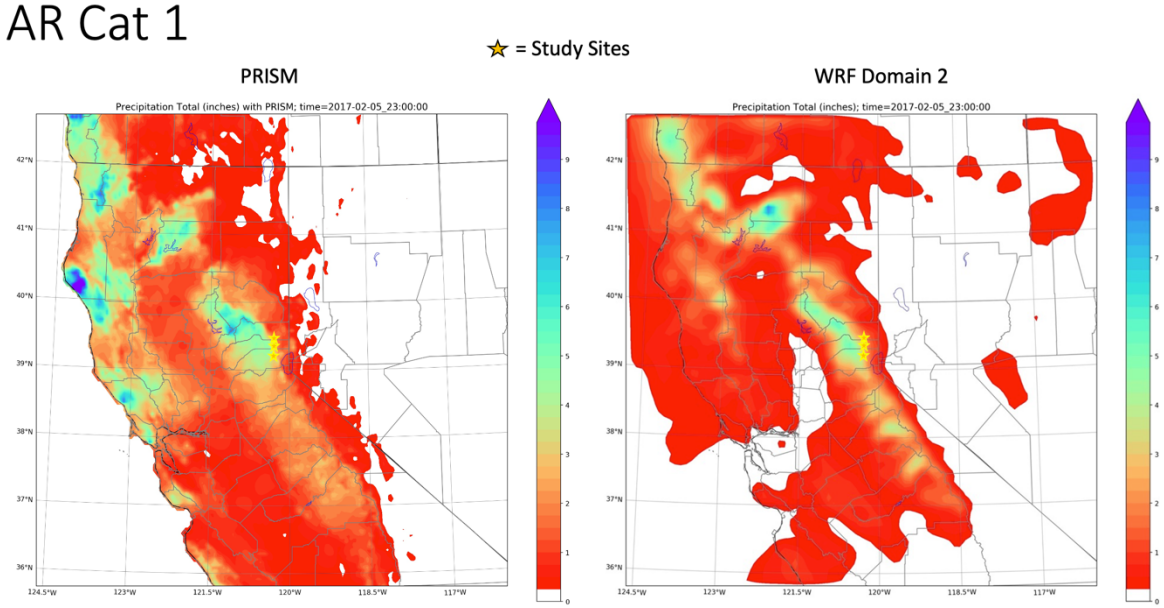

Appendix 4 Figure 5. Comparison between WRF-Control Domain-2 precipitation and PRISM precipitation for AR Cat 1.

Appendix 5 – Oakland Sounding Comparisons: Mixing Ratio, Temperature, Wind

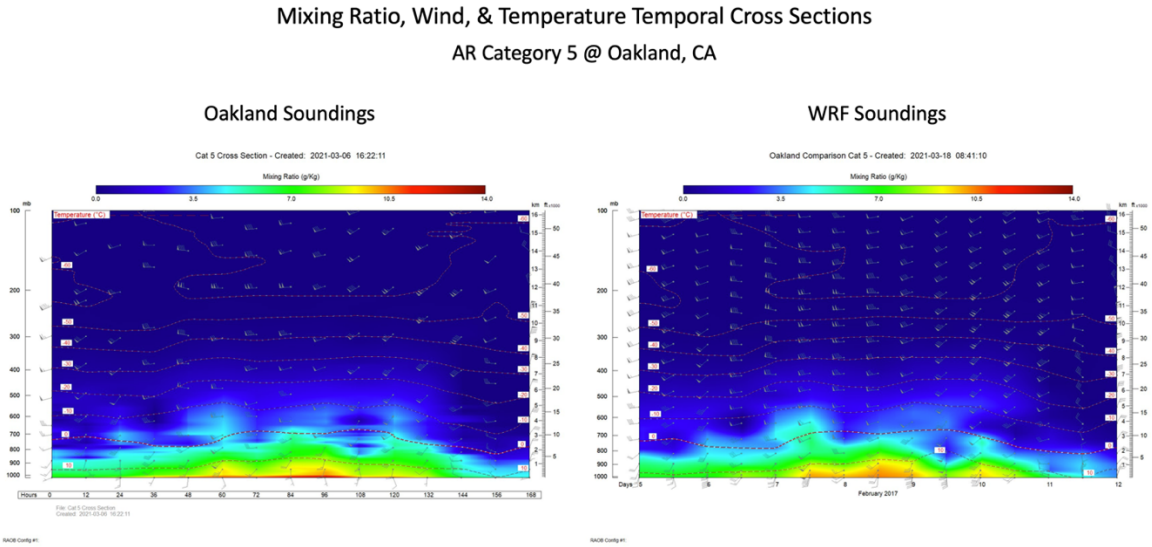

Appendix 5 Figure 1. Temporal cross section of vertical profiles of temperature (isotherms) in °C, wind (wind barbs) in knots, and color-filled contours depicting Mixing Ratio in g/Kg for AR Cat 5. Oakland Soundings were launched by the National Weather Service in Oakland, CA, and WRF Soundings are model-derived soundings (Domain-2) for the same times and locations as the Oakland Soundings. Plotted using RAOB software.

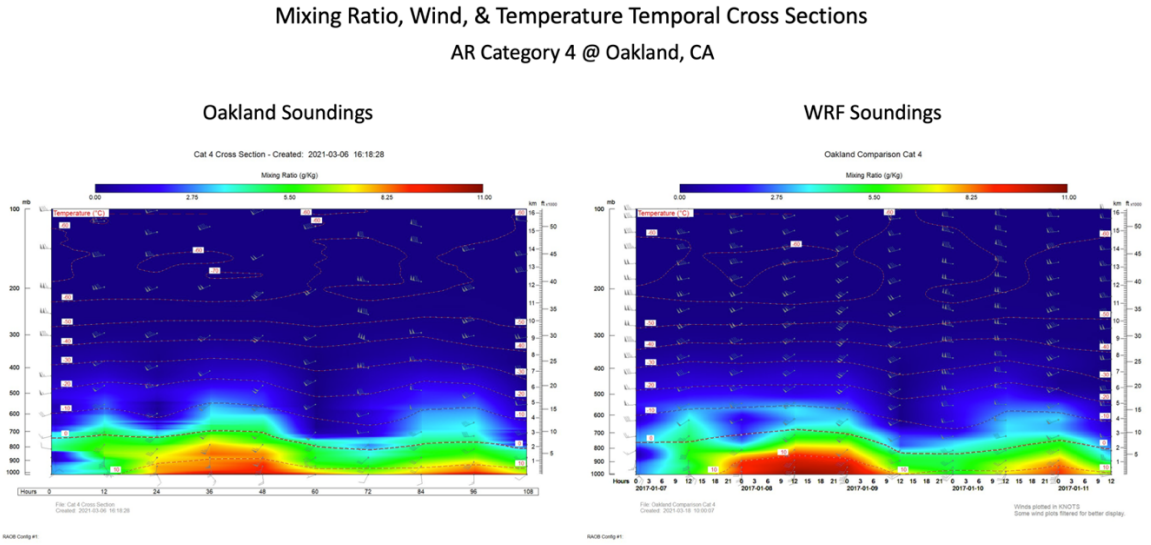

Appendix 5 Figure 2. Temporal cross section of vertical profiles of temperature (isotherms) in °C, wind (wind barbs) in knots, and color-filled contours depicting Mixing Ratio in g/Kg for AR Cat 4. Oakland Soundings were launched by the National Weather Service in Oakland, CA, and WRF Soundings are model-derived soundings (Domain-2) for the same times and locations as the Oakland Soundings. Plotted using RAOB software.

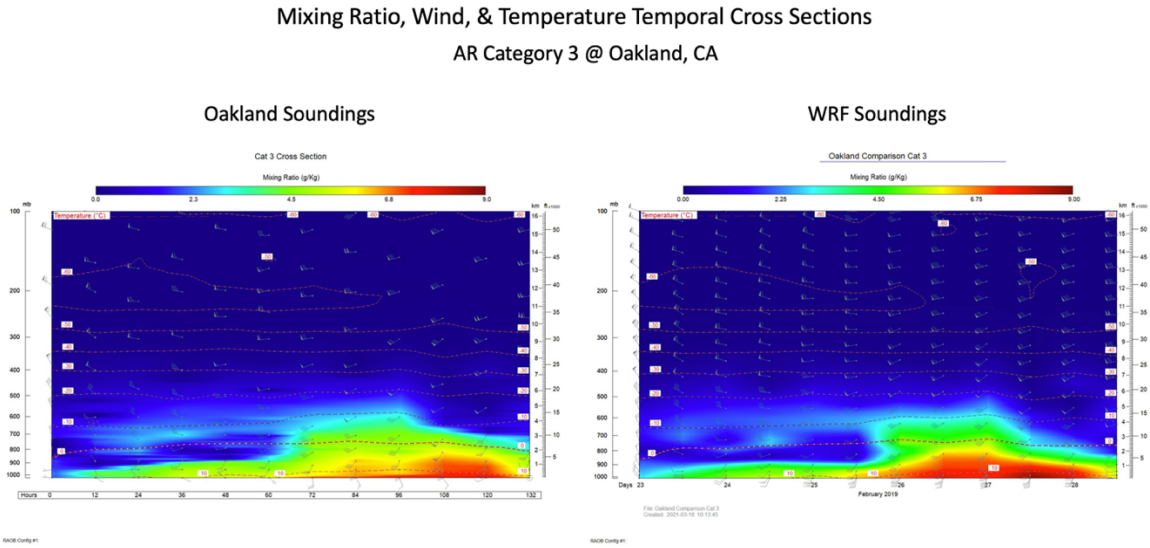

Appendix 5 Figure 3. Temporal cross section of vertical profiles of temperature (isotherms) in °C, wind (wind barbs) in knots, and color-filled contours depicting Mixing Ratio in g/Kg for AR Cat 3. Oakland Soundings were launched by the National Weather Service in Oakland, CA, and WRF Soundings are model-derived soundings (Domain-2) for the same times and locations as the Oakland Soundings. Plotted using RAOB software.

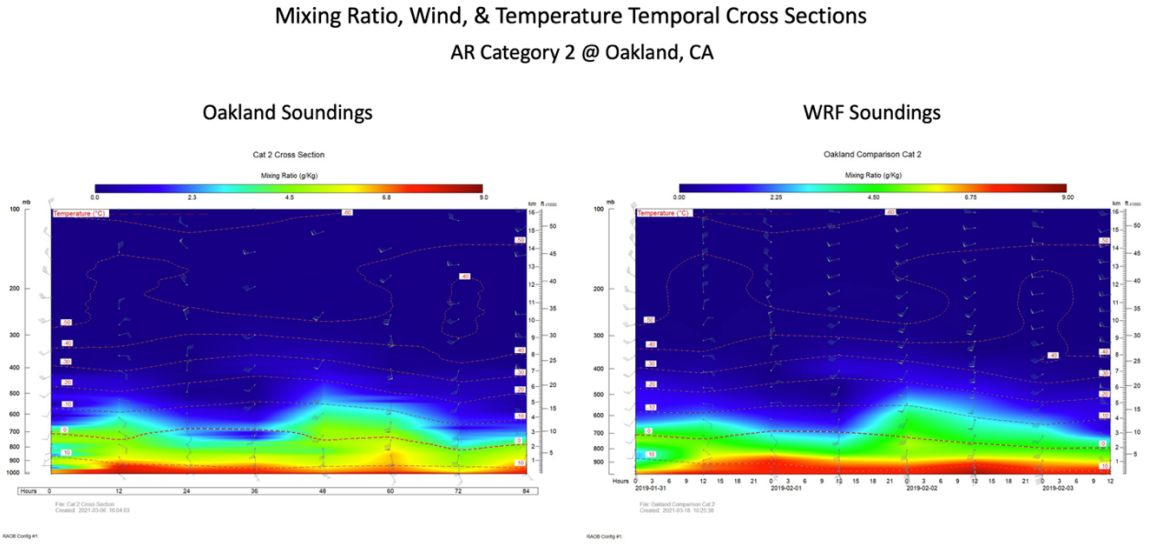

Appendix 5 Figure 4. Temporal cross section of vertical profiles of temperature (isotherms) in °C, wind (wind barbs) in knots, and color-filled contours depicting Mixing Ratio in g/Kg for AR Cat 2. Oakland Soundings were launched by the National Weather Service in Oakland, CA, and WRF Soundings are model-derived soundings (Domain-2) for the same times and locations as the Oakland Soundings. Plotted using RAOB software.

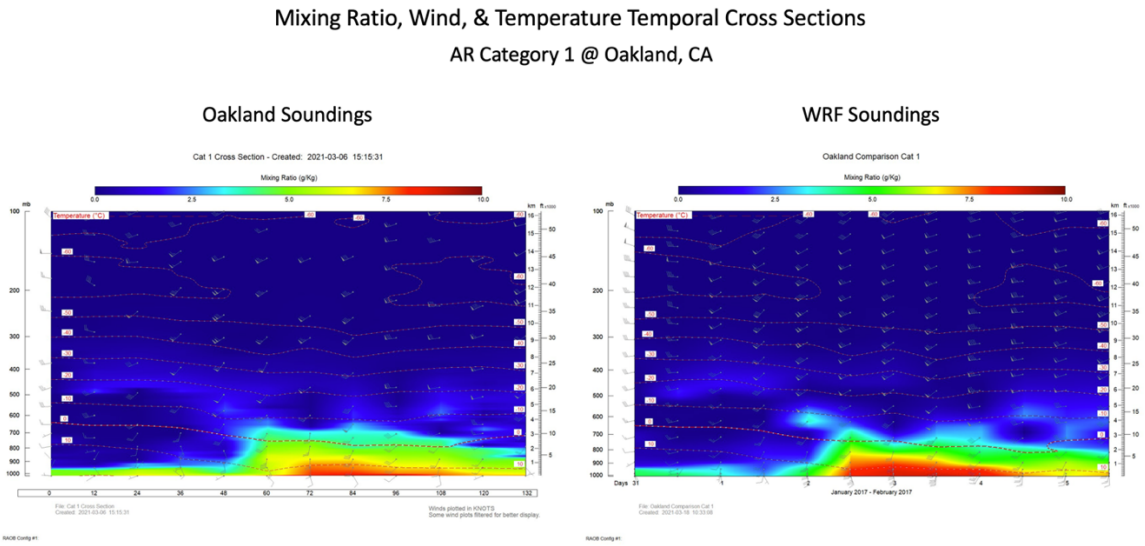

Appendix 5 Figure 5. Temporal cross section of vertical profiles of temperature (isotherms) in °C, wind (wind barbs) in knots, and color-filled contours depicting Mixing Ratio in g/Kg for AR Cat 1. Oakland Soundings were launched by the National Weather Service in Oakland, CA, and WRF Soundings are model-derived soundings (Domain-2) for the same times and locations as the Oakland Soundings. Plotted using RAOB software.

Appendix 6 – IVT Comparison: Control vs PGW

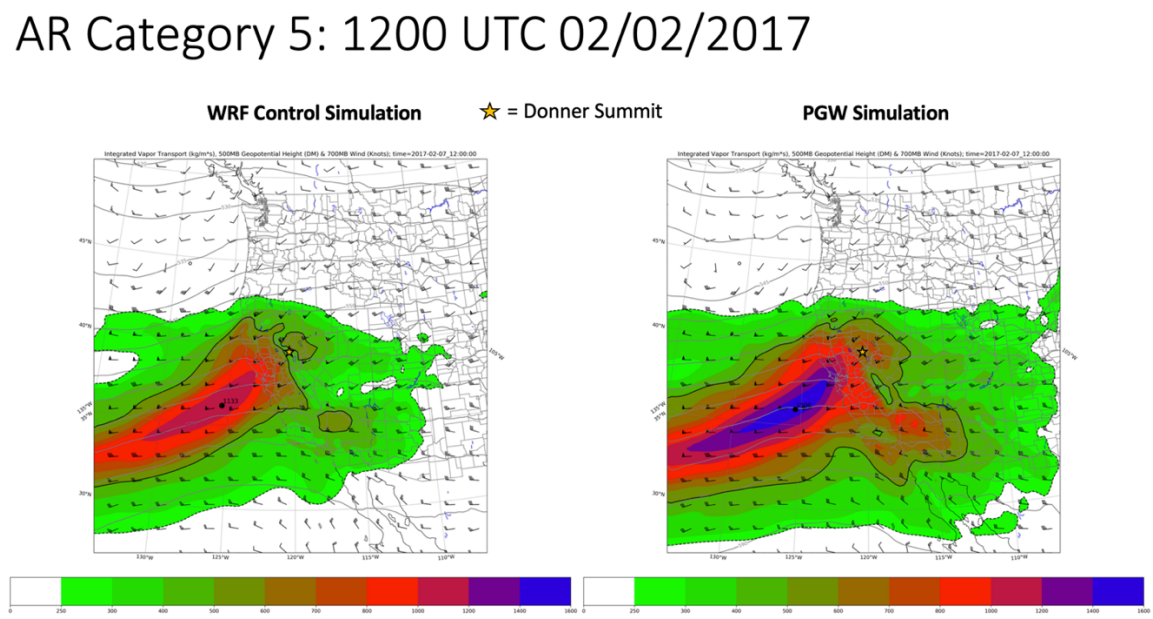

Appendix 6 Figure 1. Comparison of WRF Control and PGW simulations of IVT for AR Cat 5 near the time of landfall.

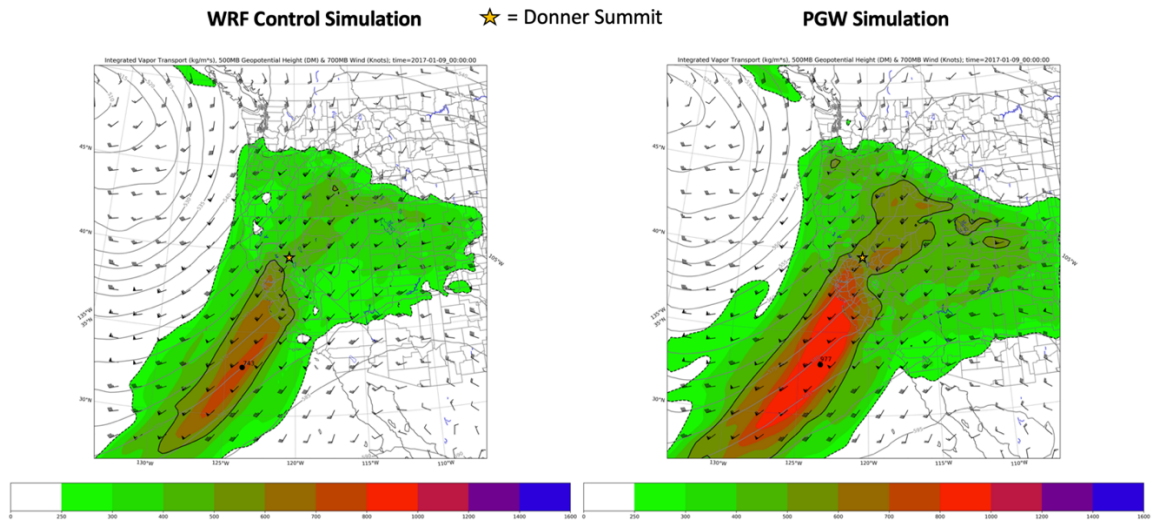

Appendix 6 Figure 2. Comparison of WRF Control and PGW simulations of IVT for AR Cat 4 near the time of landfall.

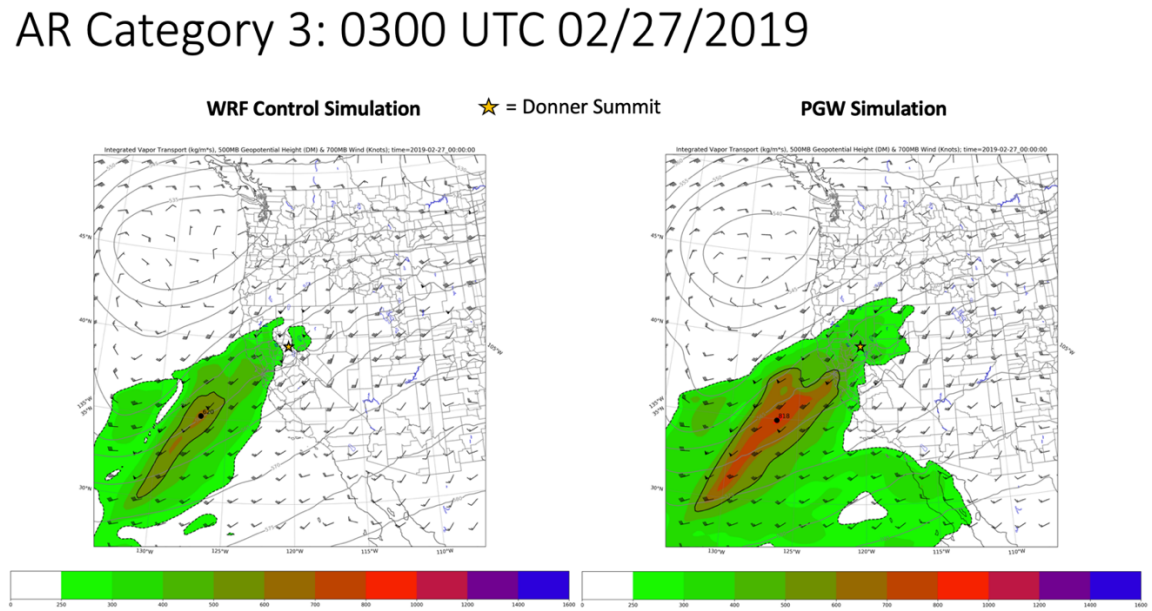

Appendix 6 Figure 3. Comparison of WRF Control and PGW simulations of IVT for AR Cat 3 near the time of landfall.

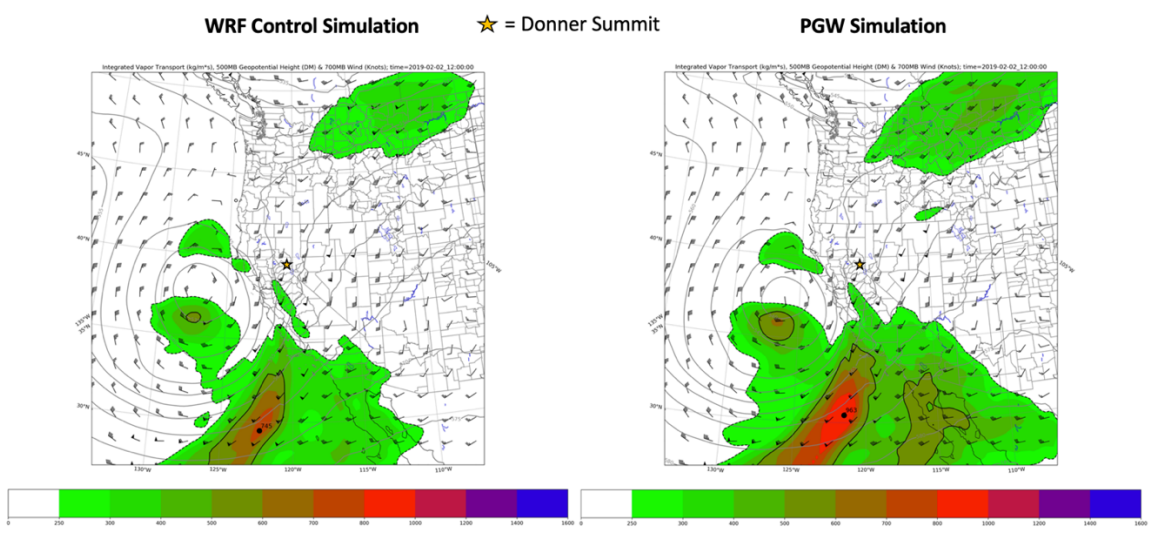

Appendix 6 Figure 4. Comparison of WRF Control and PGW simulations of IVT for AR Cat 2 near the time of landfall.

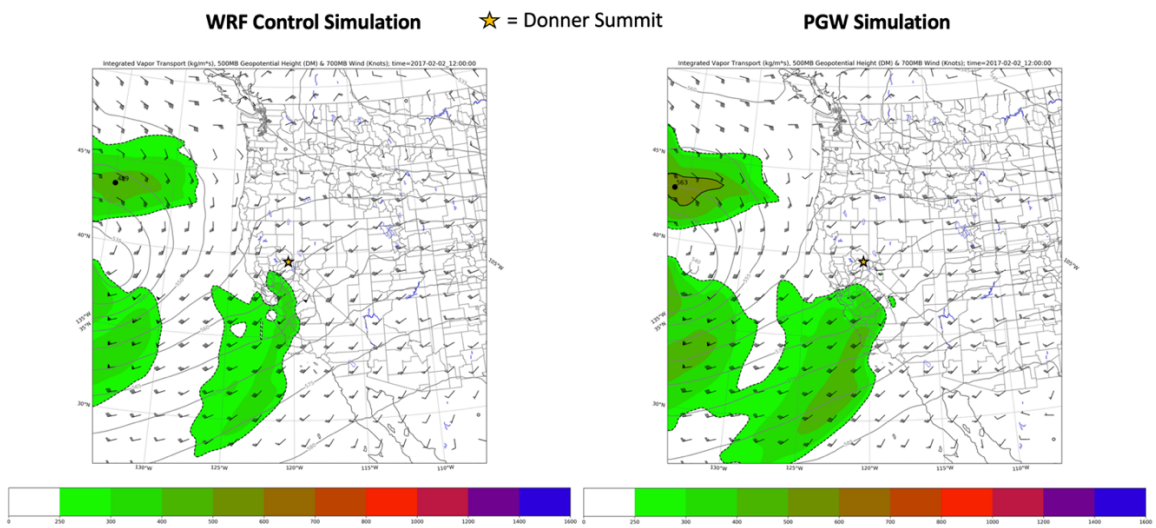

Appendix 6 Figure 5. Comparison of WRF Control and PGW simulations of IVT for AR Cat 1 near the time of landfall.

Appendix 7 – Control vs PGW Model Soundings Comparison: Mixing Ratio, Temperature, Wind

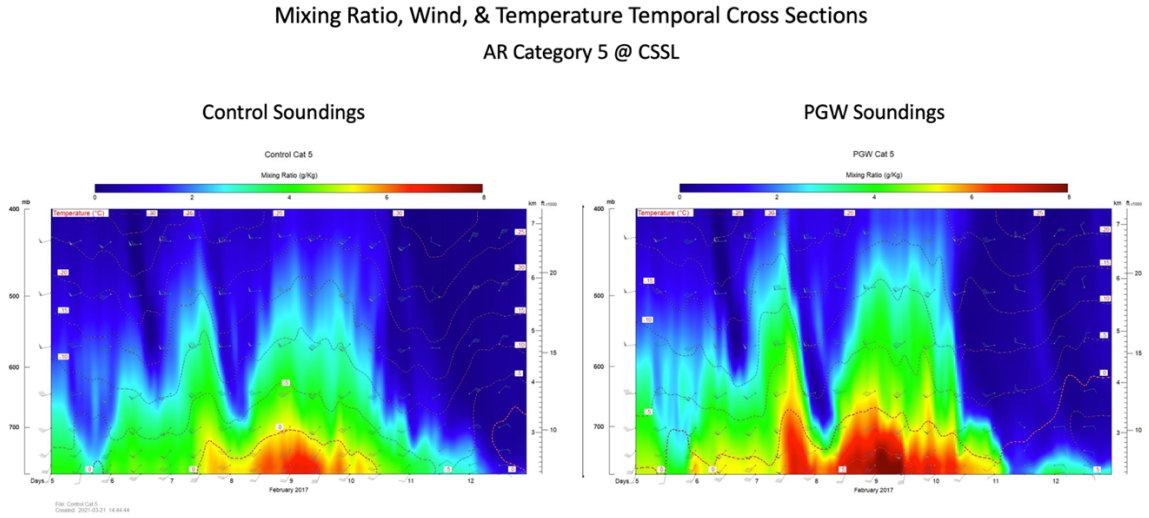

Appendix 7 Figure 1. Comparison of Control and PGW temporal cross sections of vertical profiles of atmospheric variables for AR Cat 5. Plotted with RAOB software. Temperature is represented by isotherms in °C; winds are in knots (wind barbs); mixing ratio is depicted by color-filled contours.

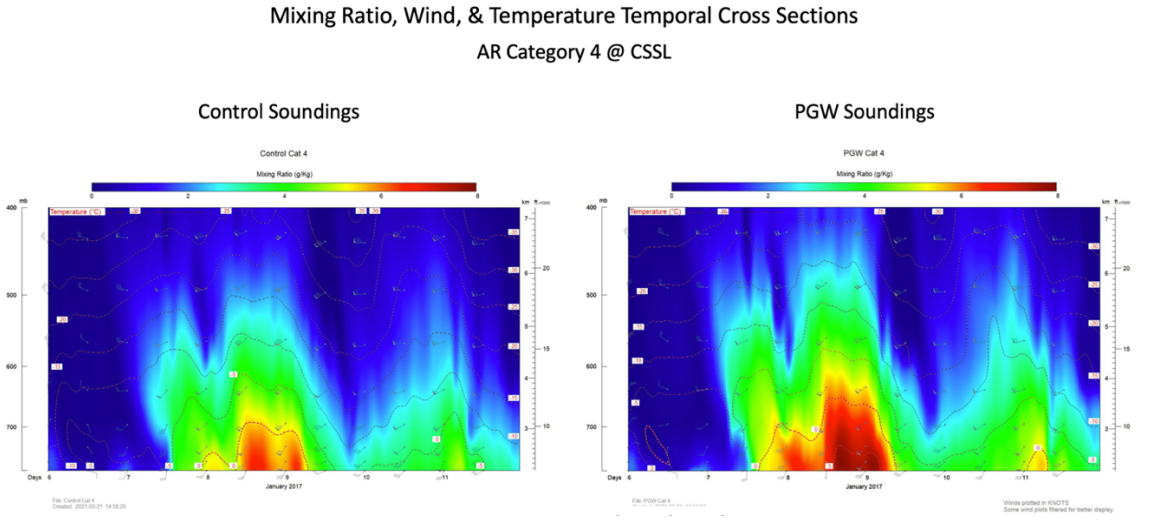

Appendix 7 Figure 2. Comparison of Control and PGW temporal cross sections of vertical profiles of atmospheric variables for AR Cat 4. Plotted with RAOB software. Temperature is represented by isotherms in °C; winds are in knots (wind barbs); mixing ratio is depicted by color-filled contours.

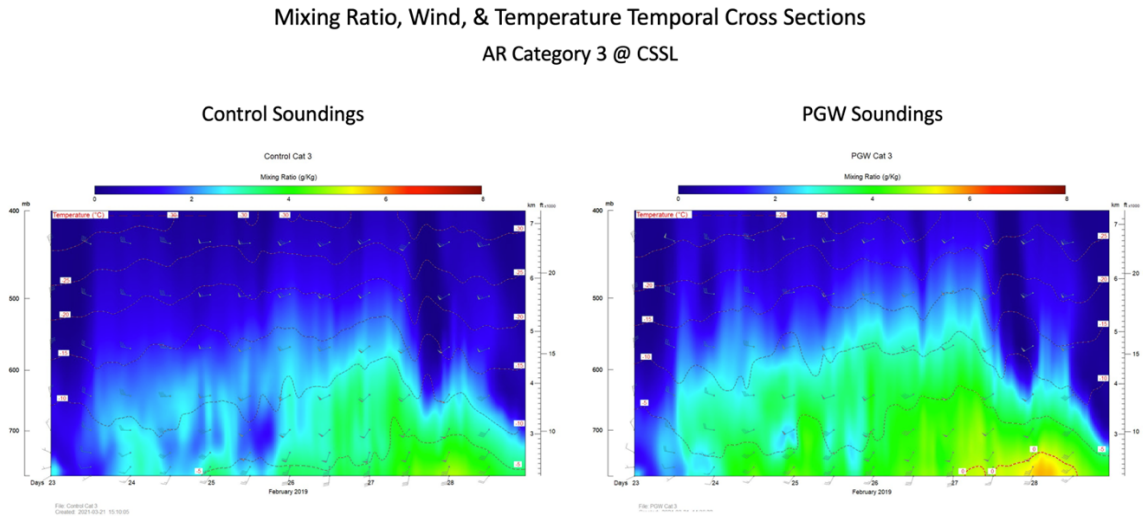

Appendix 7 Figure 3. Comparison of Control and PGW temporal cross sections of vertical profiles of atmospheric variables for AR Cat 3. Plotted with RAOB software. Temperature is represented by isotherms in °C; winds are in knots (wind barbs); mixing ratio is depicted by color-filled contours.

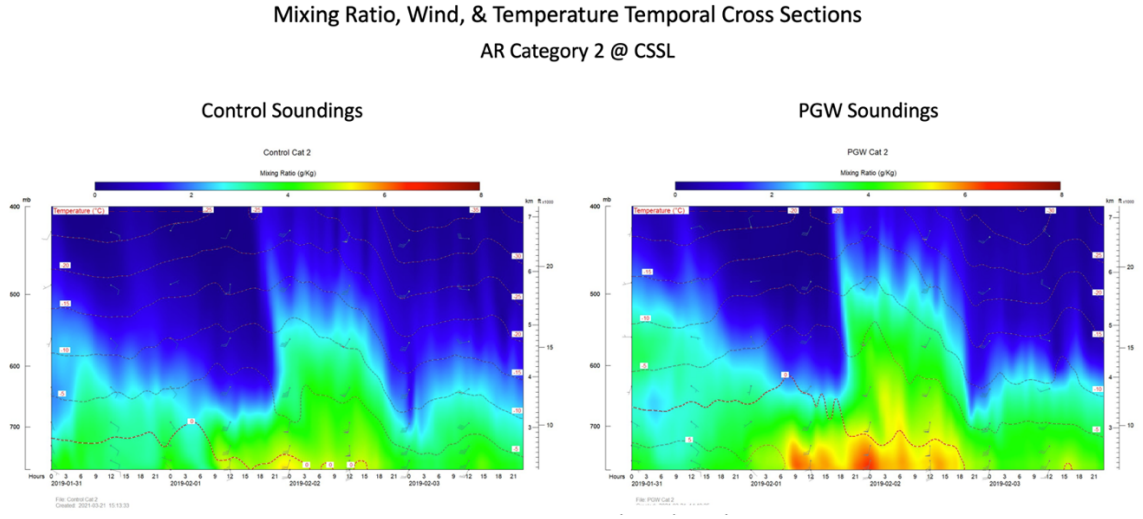

Appendix 7 Figure 4. Comparison of Control and PGW temporal cross sections of vertical profiles of atmospheric variables for AR Cat 2. Plotted with RAOB software. Temperature is represented by isotherms in °C; winds are in knots (wind barbs); mixing ratio is depicted by color-filled contours.

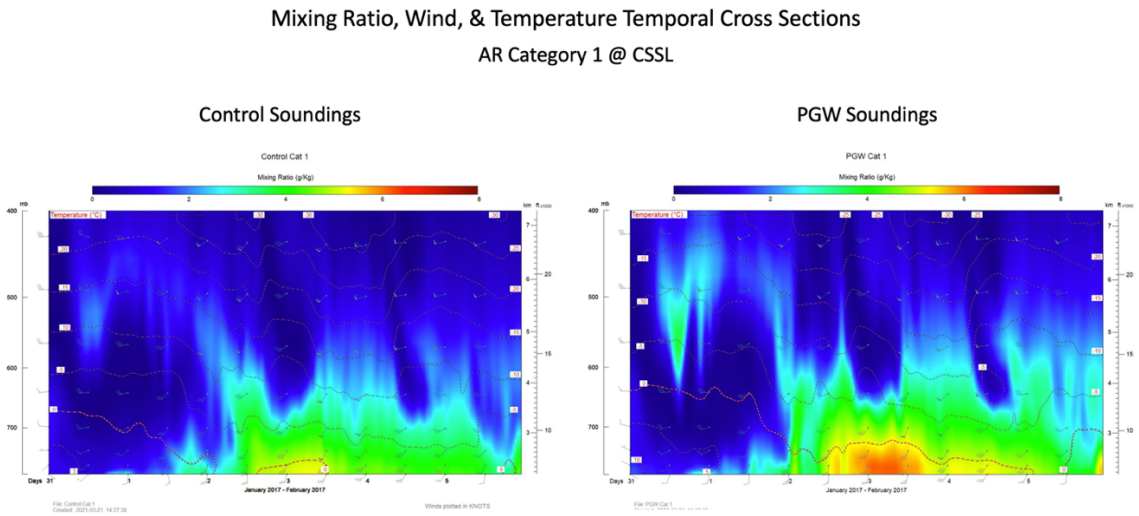

Appendix 7 Figure 5. Comparison of Control and PGW temporal cross sections of vertical profiles of atmospheric variables for AR Cat 1. Plotted with RAOB software. Temperature is represented by isotherms in °C; winds are in knots (wind barbs); mixing ratio is depicted by color-filled contours.

Appendix 8 – Precipitation Comparison: PGW vs Control

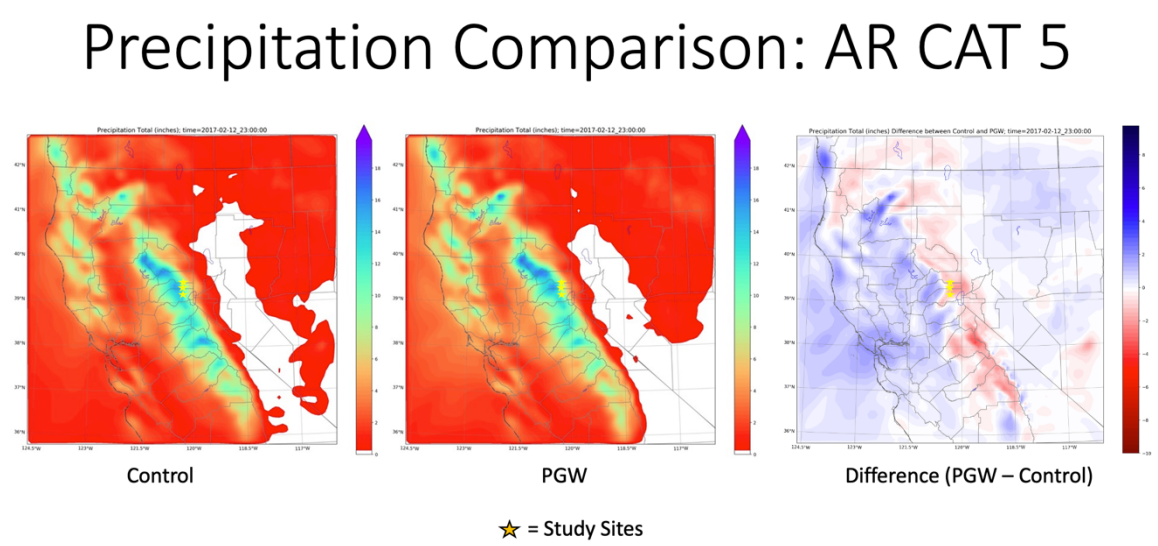

Appendix 8 Figure 1. AR Cat 5 Total Precipitation Comparison (PGW – Control) for Domain 3. Precipitation is reported in inches.

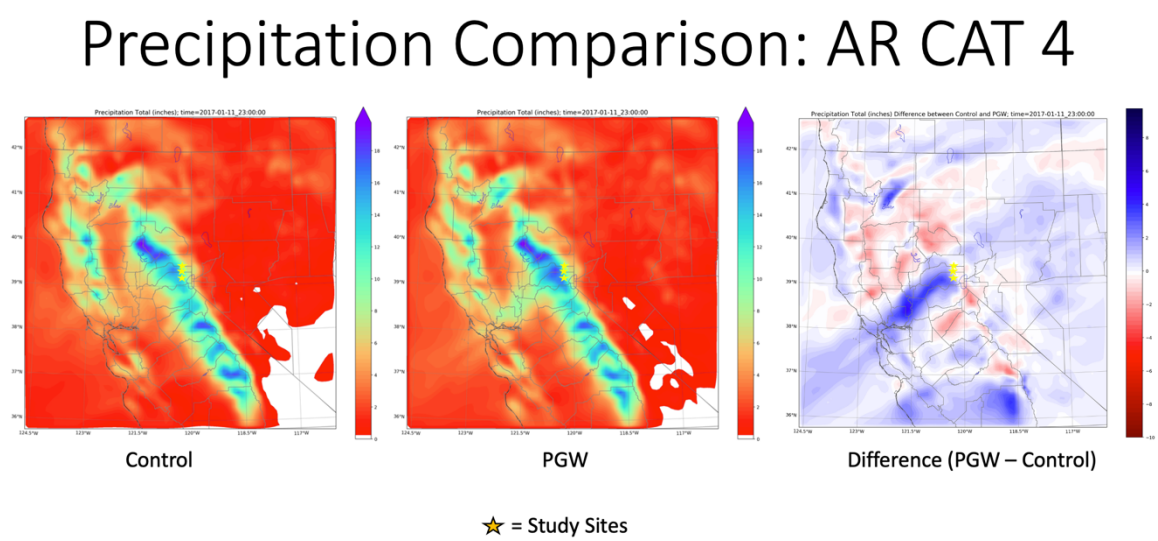

Appendix 8 Figure 2. AR Cat 4 Total Precipitation Comparison (PGW – Control) for Domain 3. Precipitation is reported in inches.

Precipitation Comparison: AR CAT 3

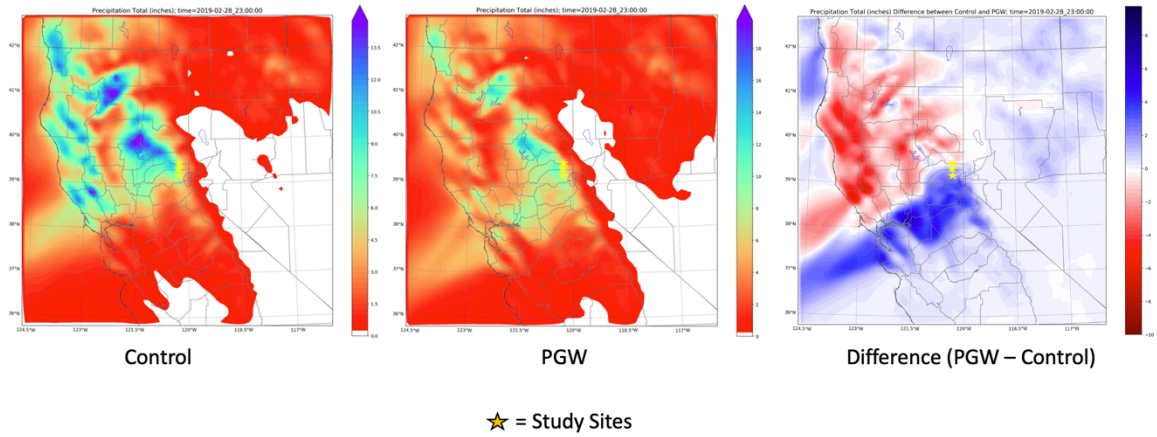

Appendix 8 Figure 3. AR Cat 3 Total Precipitation Comparison (PGW – Control) for Domain 3. Precipitation is reported in inches.

Precipitation Comparison: AR CAT 2

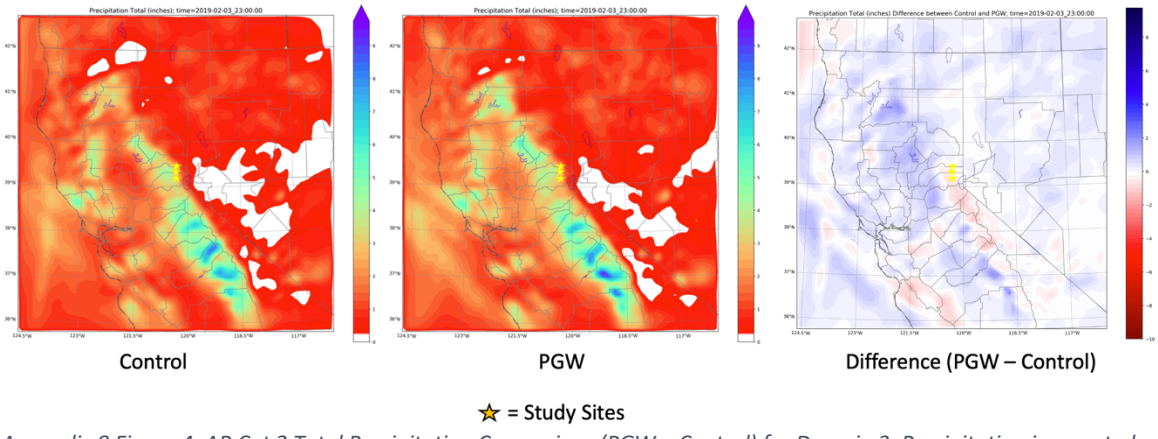

Appendix 8 Figure 4. AR Cat 2 Total Precipitation Comparison (PGW – Control) for Domain 3. Precipitation is reported in inches.

Precipitation Comparison: AR CAT 1

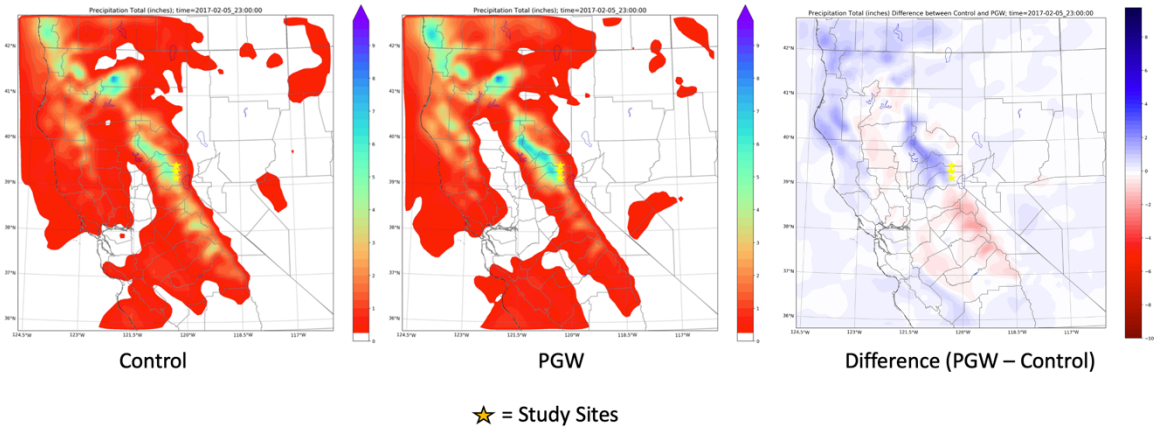

Appendix 8 Figure 5. AR Cat 1 Total Precipitation Comparison (PGW – Control) for Domain 3. Precipitation is reported in inches.

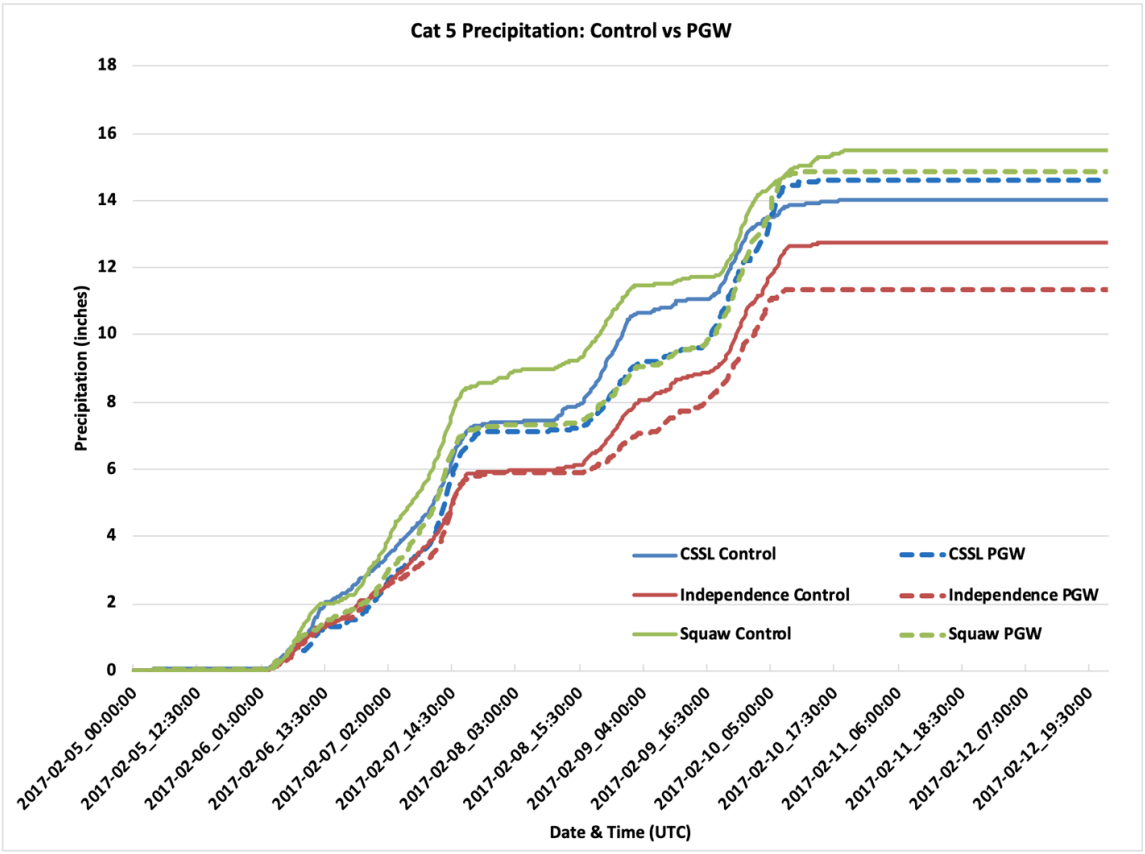

Appendix 8 Figure 6. Timeseries plots depicting a comparison of precipitation accumulation over time for WRF Domain-4 Control and PGW simulations. Solid lines represent Control simulations; dashed lines represent PGW simulations. Colors are as-defined by the legend.

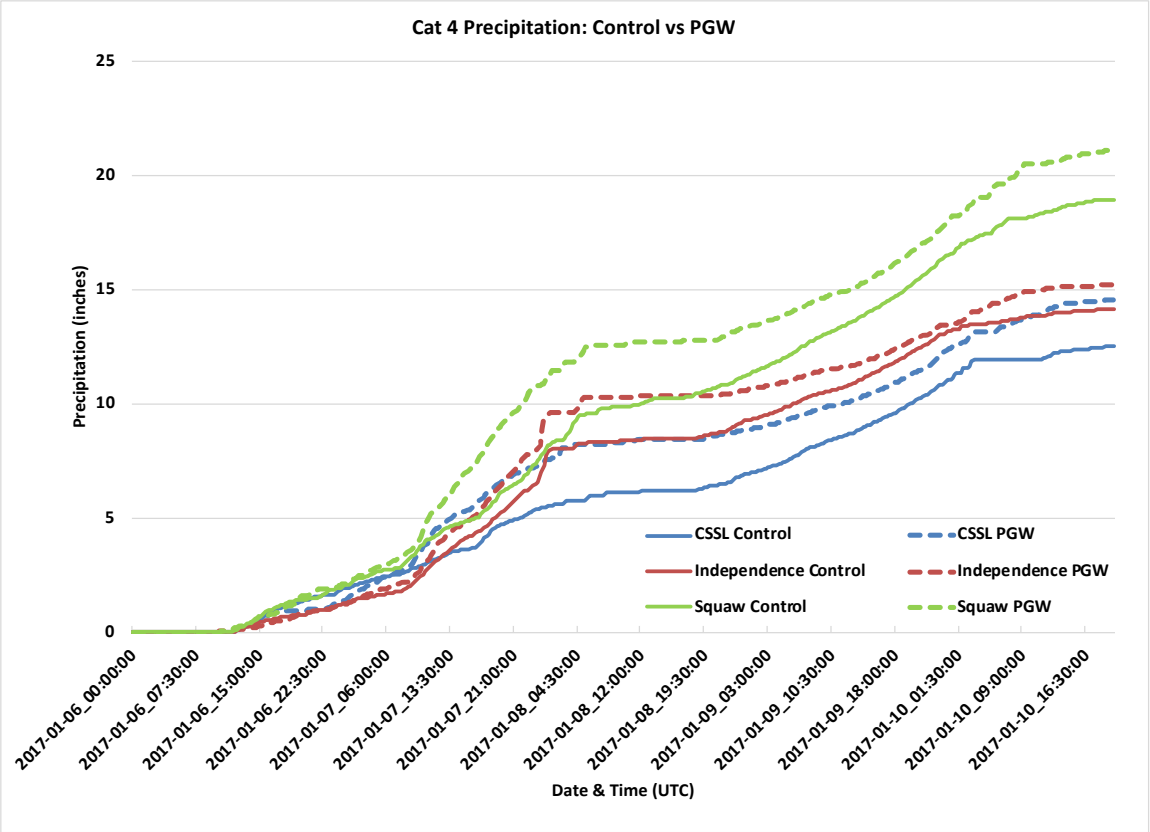

Appendix 8 Figure 7. Timeseries plots depicting a comparison of precipitation accumulation over time for WRF Domain-4 Control and PGW simulations. Solid lines represent Control simulations; dashed lines represent PGW simulations. Colors are as-defined by the legend.

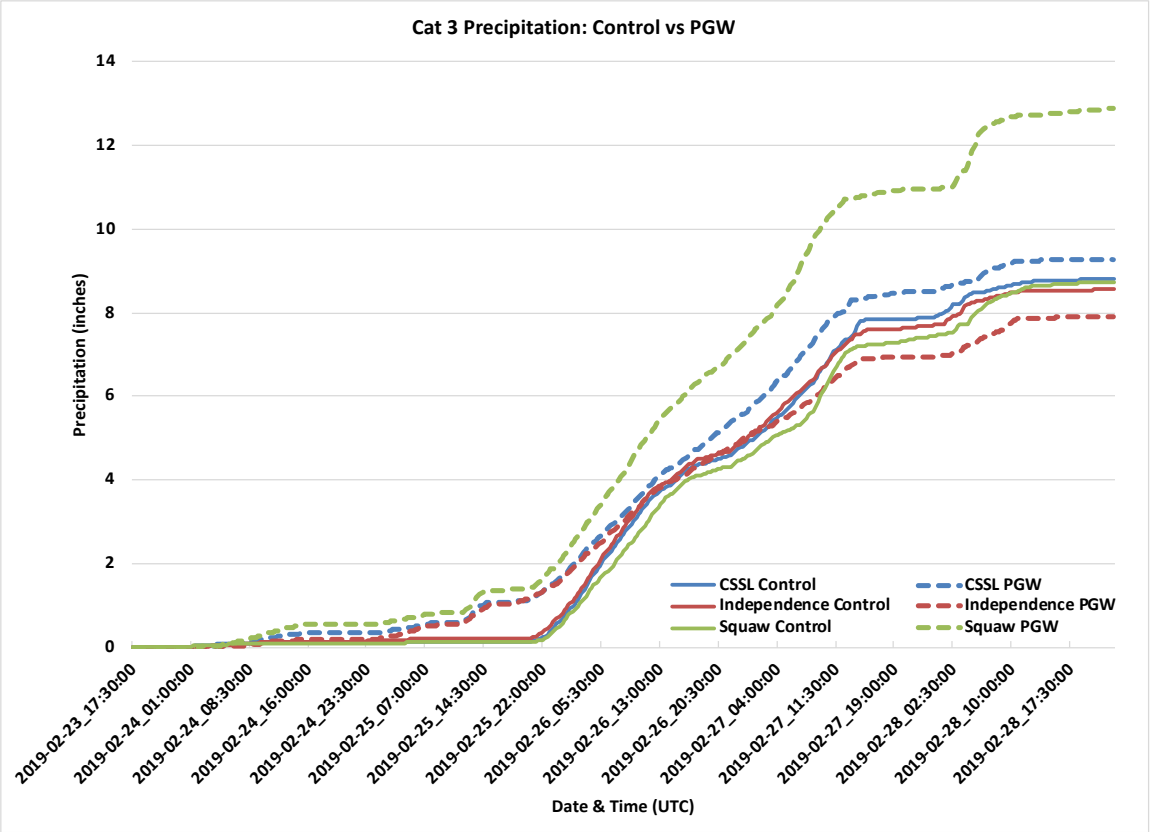

Appendix 8 Figure 8. Timeseries plots depicting a comparison of precipitation accumulation over time for WRF Domain-4 Control and PGW simulations. Solid lines represent Control simulations; dashed lines represent PGW simulations. Colors are as-defined by the legend.

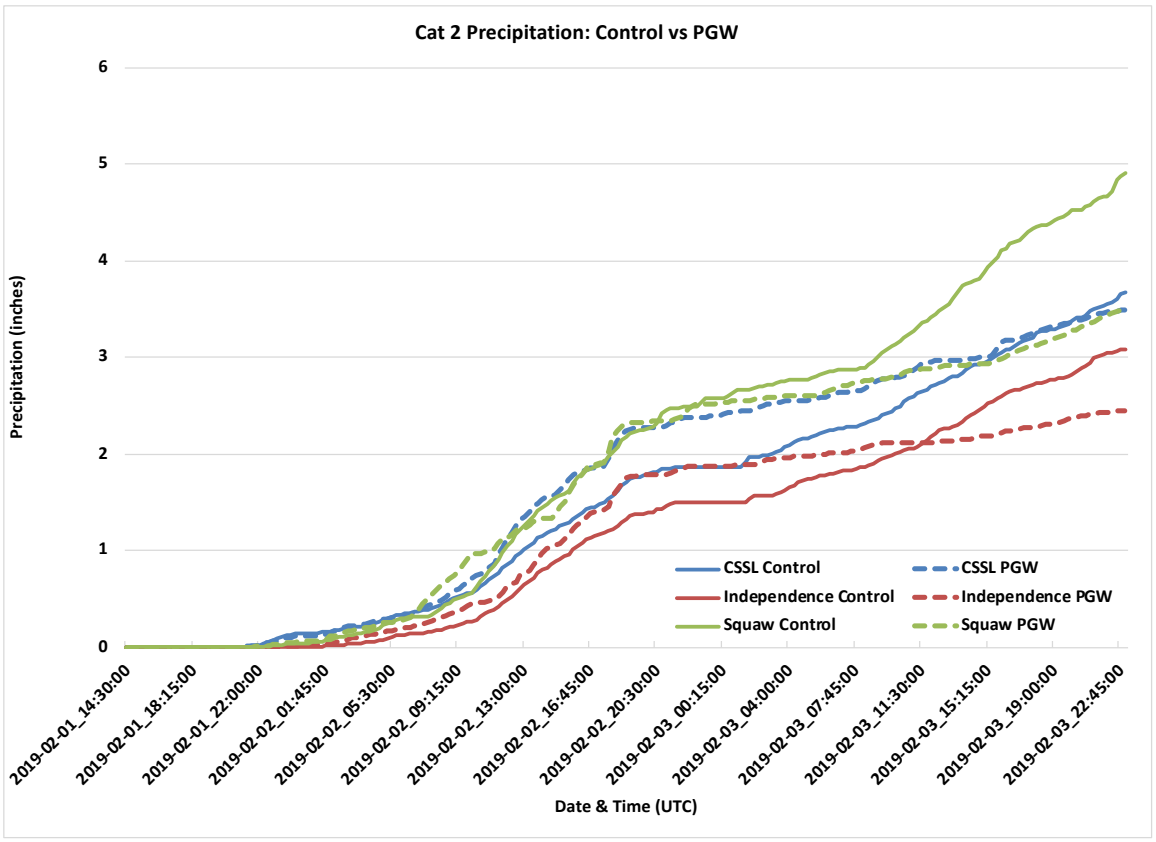

Appendix 8 Figure 9. Timeseries plots depicting a comparison of precipitation accumulation over time for WRF Domain-4 Control and PGW simulations. Solid lines represent Control simulations; dashed lines represent PGW simulations. Colors are as-defined by the legend.

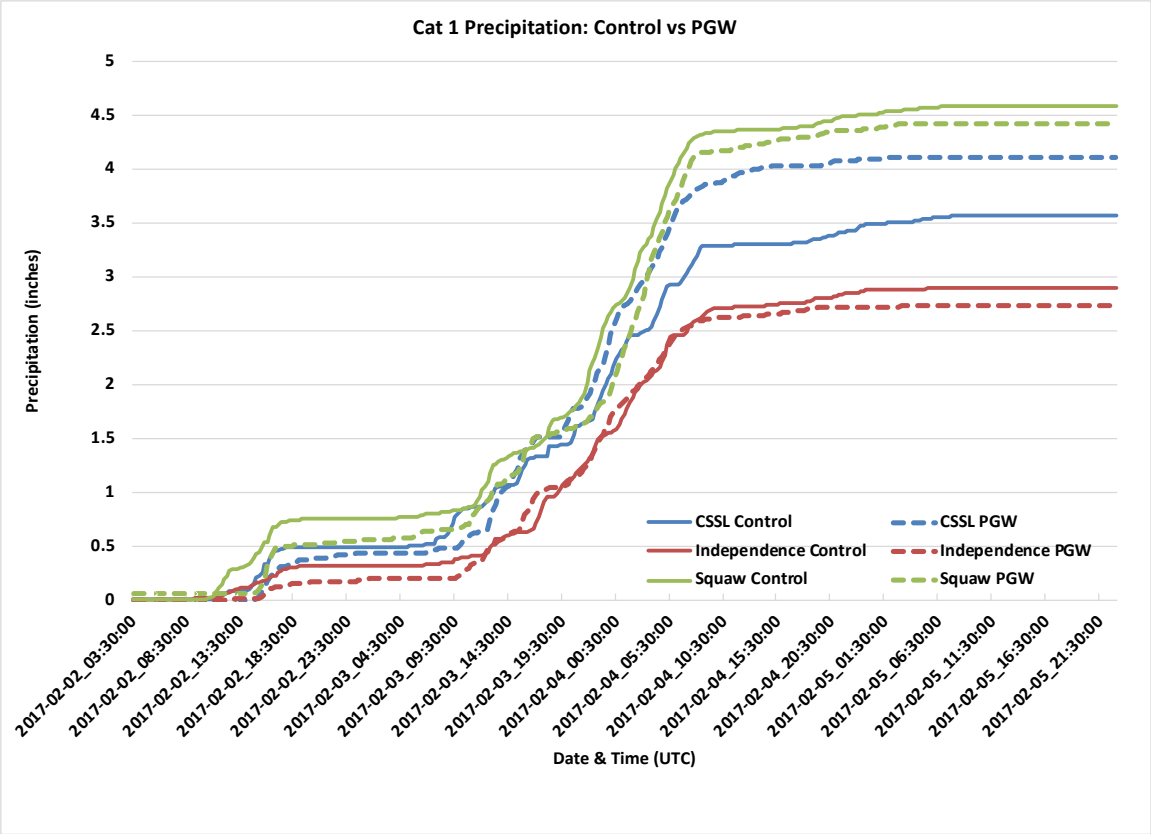

Appendix 8 Figure 10. Timeseries plots depicting a comparison of precipitation accumulation over time for WRF Domain-4 Control and PGW simulations. Solid lines represent Control simulations; dashed lines represent PGW simulations. Colors are as-defined by the legend.

Atmospheric River	SNOTEL Precip	% Change (PGW-Control)	RCP8.5 New AR Precip
AR Cat 5	11.97”	-3.45	**11.56”**
AR Cat 4	12.86”	11.67	**14.36”**
AR Cat 3	7.53”	15.30	**8.68”**
AR Cat 2	2.9”	-18.87	**2.35”**
AR Cat 1	3.93”	1.90	**4.00”**

Appendix 8 Figure 11. Table reporting RCP8.5 PGW-adjusted precipitation totals. SNOTEL observations were adjusted by the % change in the PGW vs Control observations. % Change is calculated with respect to Control simulations.

Appendix 9 – Temperature Comparison: Control vs PGW

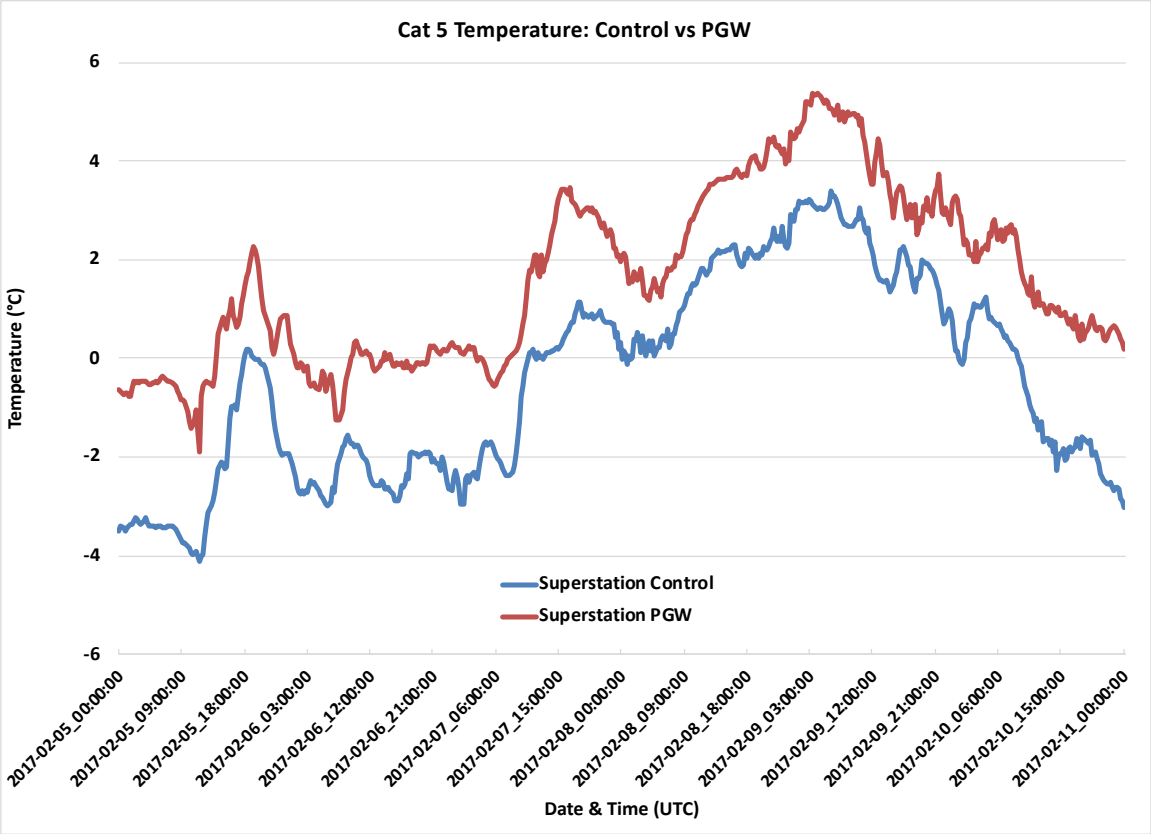

Appendix 9 Figure 1. Comparison of WRF Domain-4 Control and PGW AR Cat 5 Temperature.

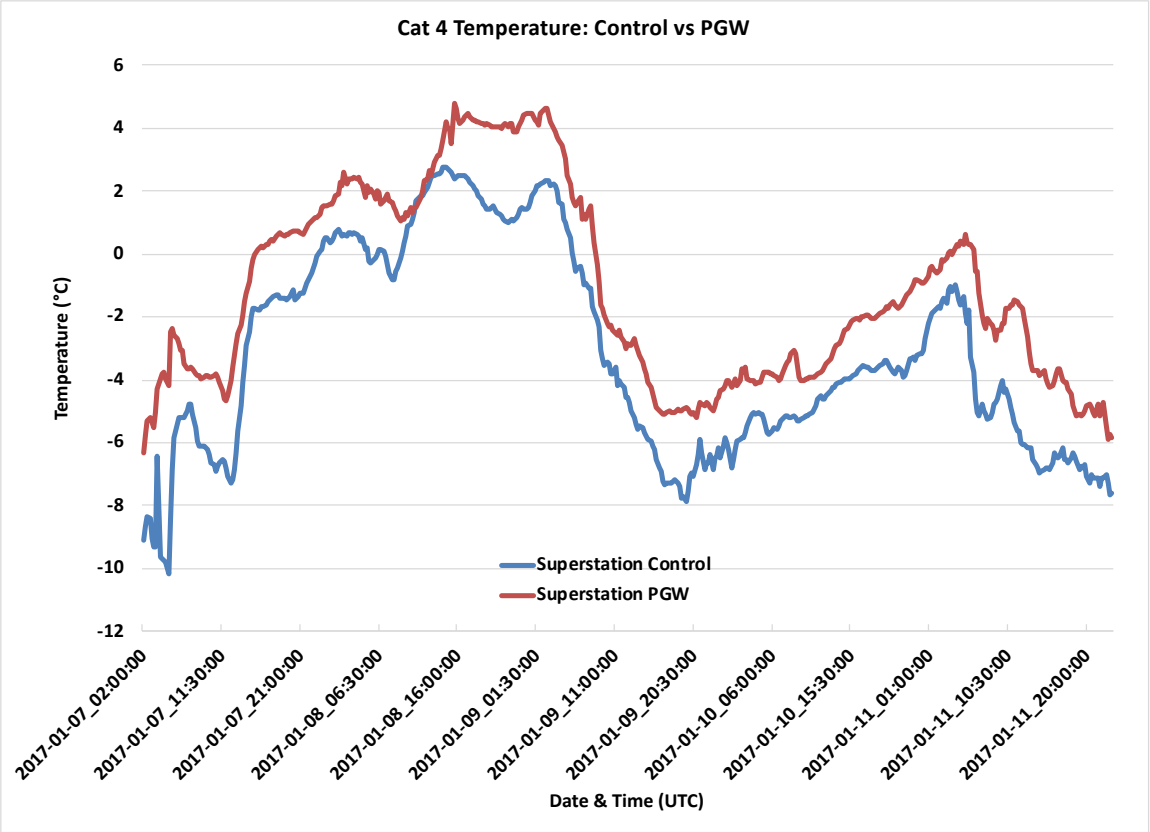

Appendix 9 Figure 2. Comparison of WRF Domain-4 Control and PGW AR Cat 4 Temperature.

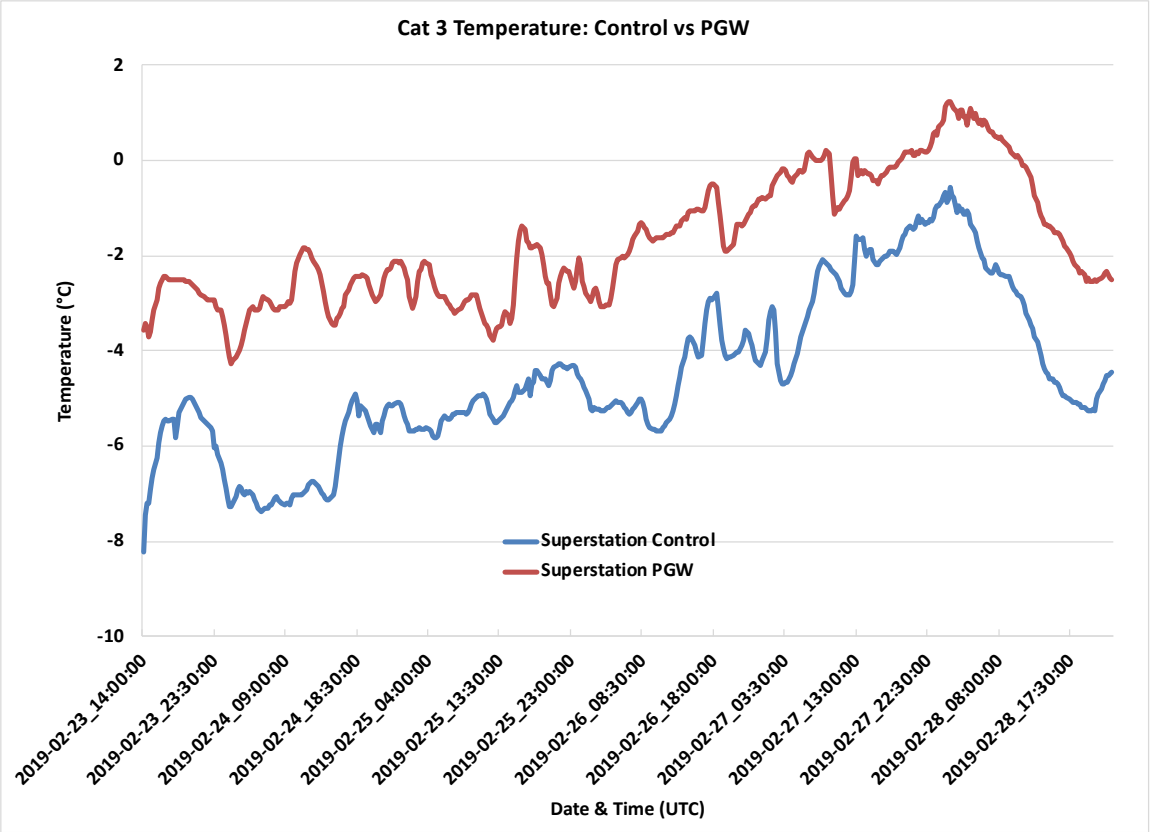

Appendix 9 Figure 3. Comparison of WRF Domain-4 Control and PGW AR Cat 3 Temperature.

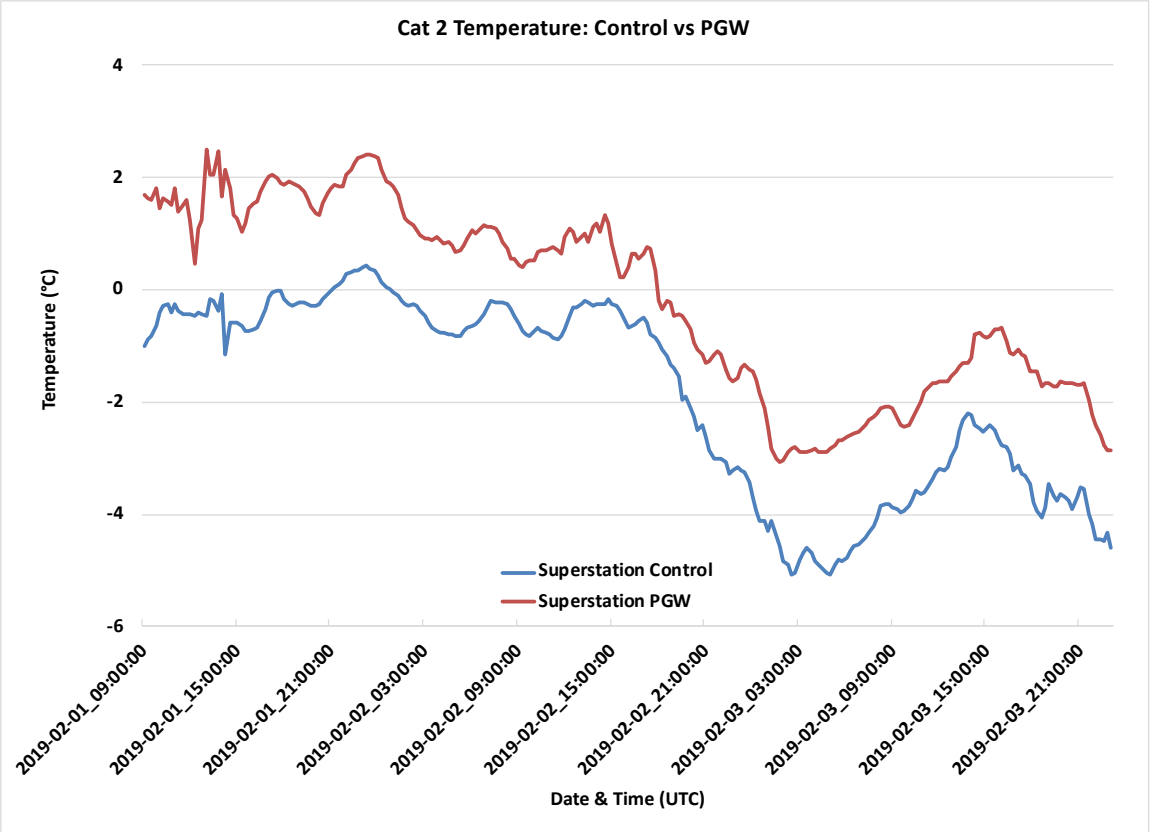

Appendix 9 Figure 4. Comparison of WRF Domain-4 Control and PGW AR Cat 2 Temperature.

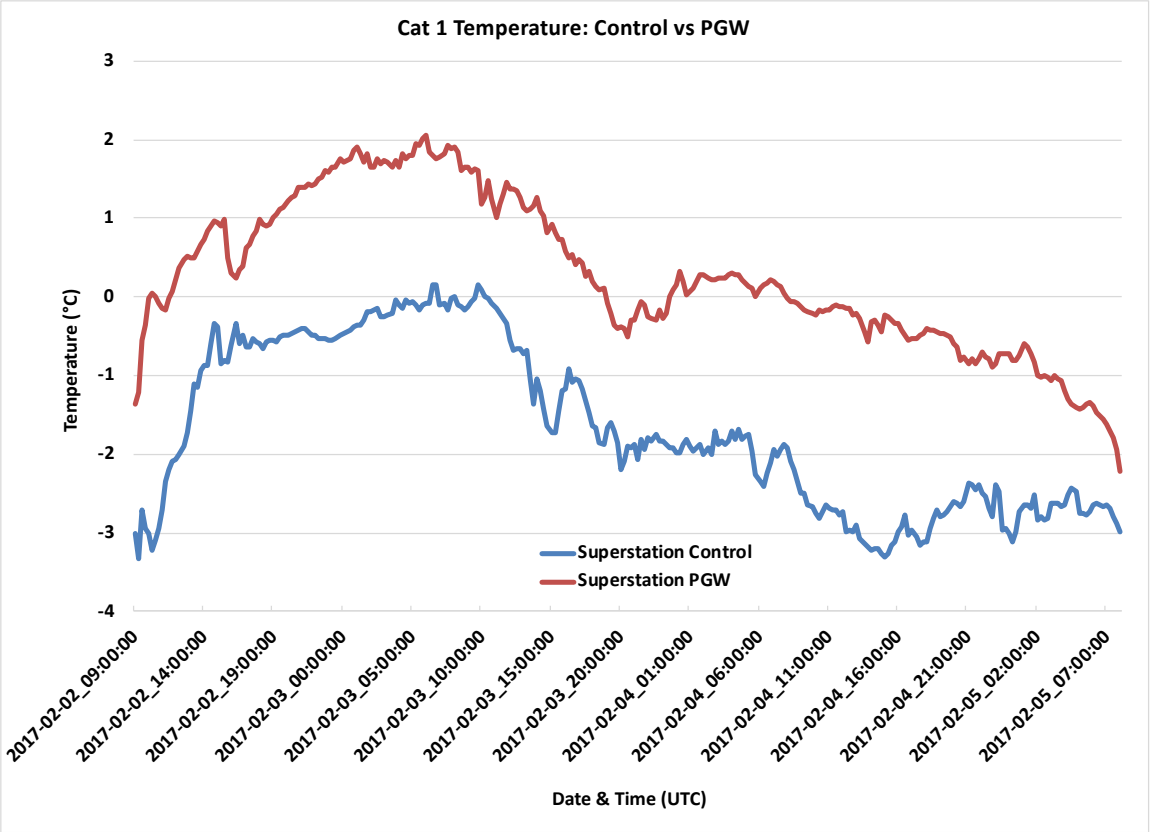

Appendix 9 Figure 5. Comparison of WRF Domain-4 Control and PGW AR Cat 1 Temperature.

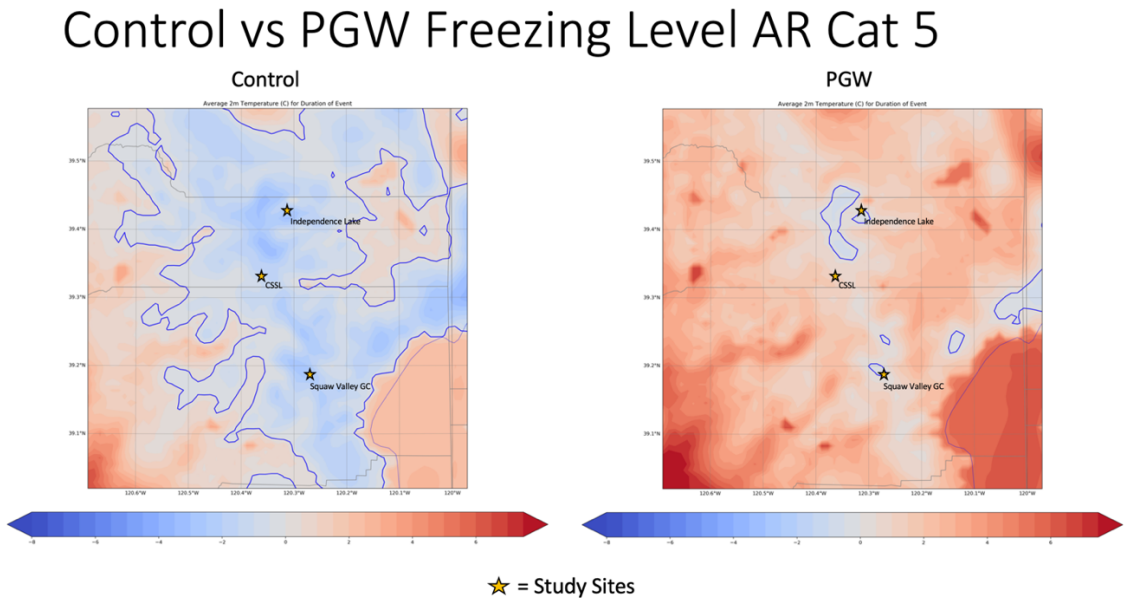

Appendix 9 Figure 6. Comparison of WRF Domain-4 Control and PGW AR Cat 5 Surface Temperature and 0°C Isotherm.

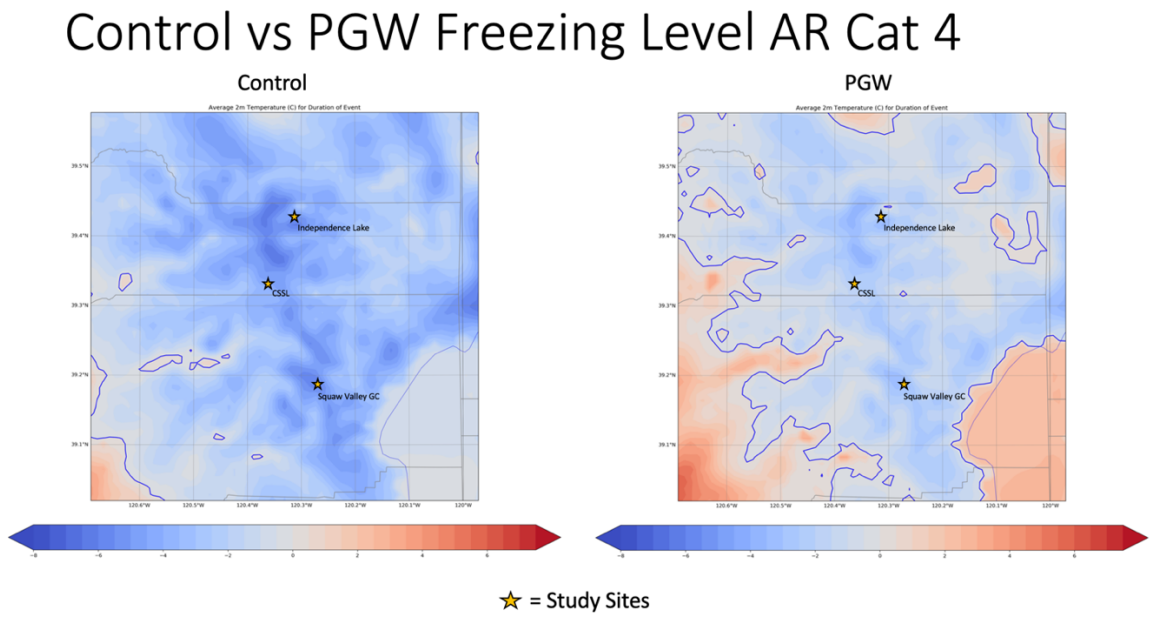

Appendix 9 Figure 7. Comparison of WRF Domain-4 Control and PGW AR Cat 4 Surface Temperature and 0°C Isotherm.

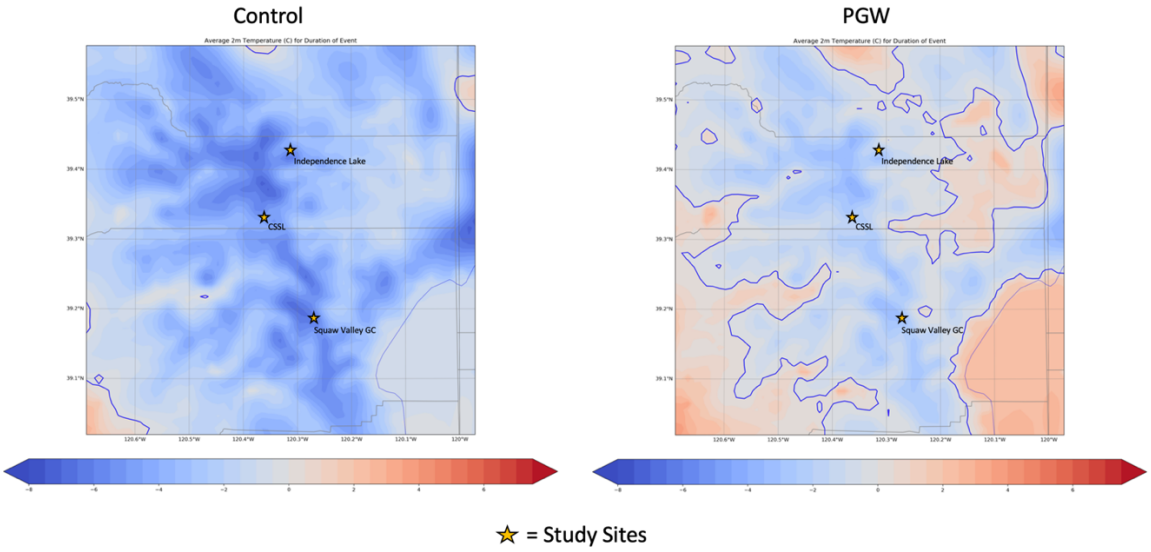

Appendix 9 Figure 8. Comparison of WRF Domain-4 Control and PGW AR Cat 3 Surface Temperature and 0°C Isotherm.

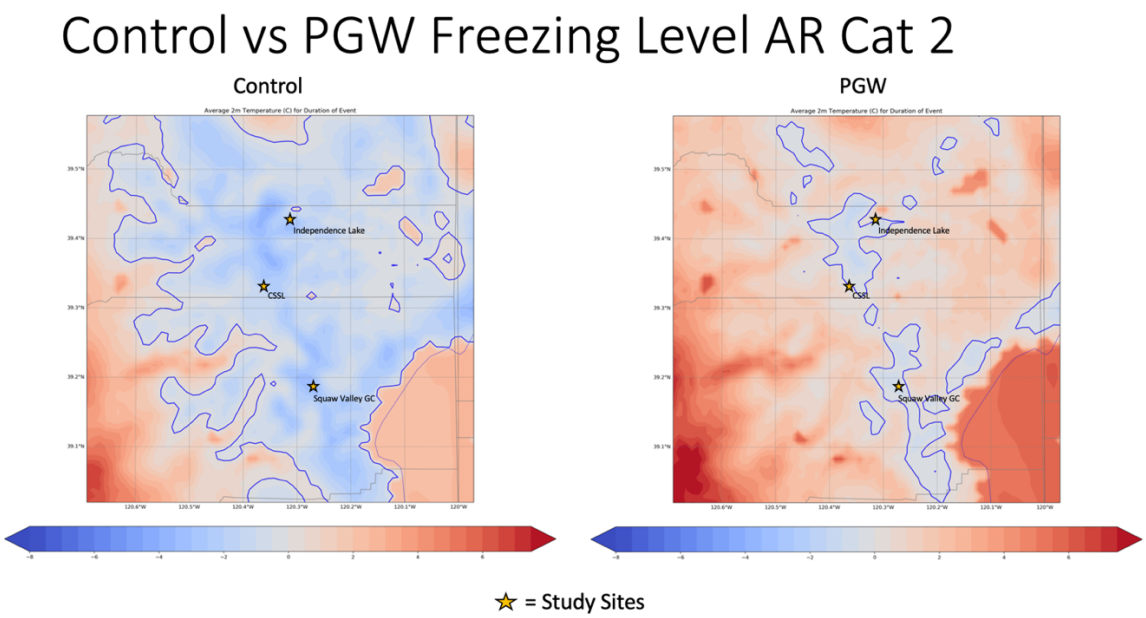

Appendix 9 Figure 9. Comparison of WRF Domain-4 Control and PGW AR Cat 2 Surface Temperature and 0°C Isotherm.

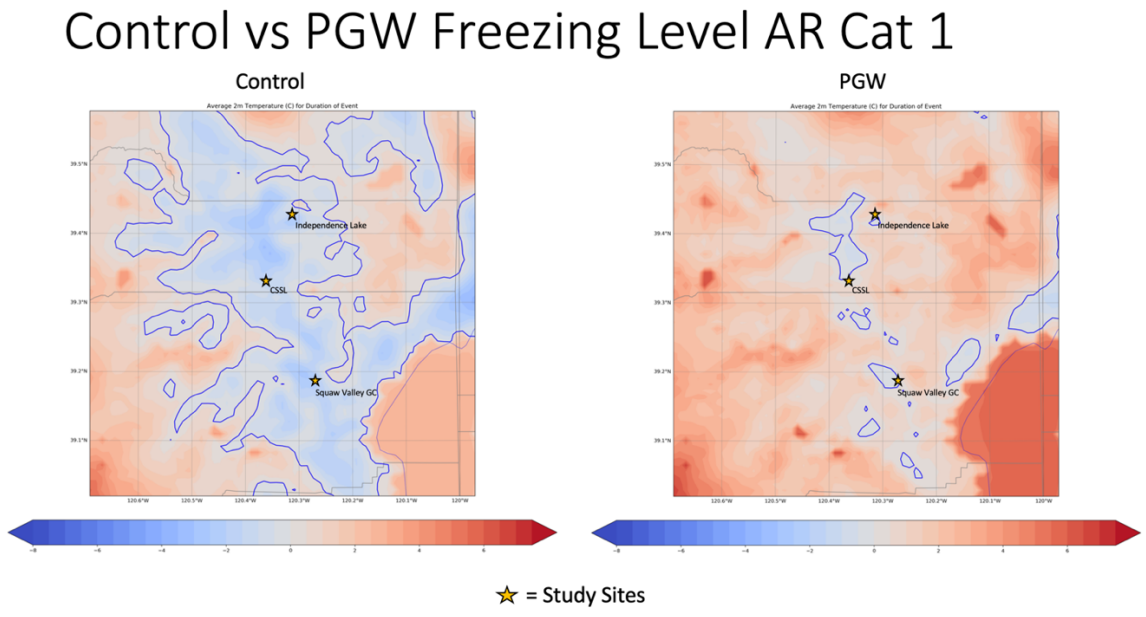

Appendix 9 Figure 10. Comparison of WRF Domain-4 Control and PGW AR Cat 1 Surface Temperature and 0°C Isotherm.